How Adhesives Should Flow during Manufacturing

From the Department of Production Engineering
of the
University of Bremen

for the degree of
Doktor der Ingenieurwissenschaften (Dr.-Ing.)
approved

Dissertation
by
M. Sc. Marvin Kaufmann

Supervisors: Prof. Dr. Bernd Mayer
Prof. Dr. Lucas F. M. da Silva, University of Porto

Date of oral examination: 22.05.2024

'Felix, qui potuit rerum cognoscere causas'

— Virgil, 29 BC

Declaration of Oath

Hereby, I — Marvin Kaufmann — declare on oath that I have prepared this thesis independently and without unauthorised external help, have not used any sources or aids other than those indicated by me, and have marked all passages taken verbatim or in terms of content from the used works as such.

Furthermore, I certify that the electronic version of the dissertation enclosed for examination purposes is identical to the printed version submitted, and I agree that this electronic version may be examined for plagiarism using qualified software to check the work.

Place, Date	Signature

Acknowledgement

I would like to begin by expressing my deepest gratitude to Prof. Bernd Mayer, my supervisor and first examiner of this thesis, for his unwavering support, confidence, trust, and the freedom he has granted me throughout this research journey. Moreover, I am truly fortunate to have had the opportunity to work under his leadership at the Fraunhofer IFAM in Bremen. The pleasant and productive working environment that Prof. Mayer has fostered — especially in such difficult times for the Fraunhofer Society — has been a source of encouragement and growth.

I would like to extend my sincere gratitude to Prof. Lucas F. M. da Silva from the University of Porto for graciously accepting the role of the second examiner for this thesis. I had the pleasure to first meet Prof. da Silva at the 'AB2023' conference in Porto, which he organized. I am truly grateful, that a man of such recognition and expertise, will take the time to evaluate and provide feedback on this thesis. Furthermore, I would like to express my deepest gratitude to Prof. Lucio Colombi Ciacchi and Claudio Balzani for their invaluable contributions as members of the examination committee.

Great thanks also goes to the German Research Foundation (DFG), which funded my research in context of the following research project: 'Efficient models for simulating the flow of highly viscous adhesives and sealants in manufacturing processes', Project ID: 445254897.

I would like to express my heartfelt appreciation to my colleagues, Prof. Michael Müller and Florian Flaig, from the Technical University of Braunschweig. Over the past three years, we have collaborated intensively on the DFG research project, and their support and teamwork have been invaluable. Through fruitful discussions and their exceptional contributions, we have achieved remarkable results that would not have been possible without their dedication and expertise. I am grateful for the privilege of working alongside such talented individuals.

I would like to extend my appreciation to all of my colleagues, past and present, at Fraunhofer IFAM in Bremen, particularly those in my department, *Adhesive bonding technology*. I begin to express my gratitude to the department head, Holger Fricke, who provided me with sufficient time and space to conduct my research, for his feedback, as well as the opportunity to contribute to several conferences and research projects.

I would like to give a special acknowledgement to Till Vallée, the head of my working group, *Structural bonding*, who has been a constant source of belief and support since I have started at Fraunhofer IFAM as a student assistant. He recognized and promoted my potential, both personally and professionally, over the past years. Without his invaluable assistance and unique discussions, many of the concepts and ideas that form the basis of this work would not have been possible. I am sincerely grateful for his invaluable special ideas and that he created an atmosphere that nurtures creativity and collaboration.

Furthermore, I would like to thank Morten Voss, Ivo Neumann, Simon Fecht, Cordula Grunwald, Jonas Wirries, Michael Adam, Mathis Eppmann, Sascha Voss, Andrea Paul, Sebastian Mysliki as well as all of the other colleagues who have supported me throughout my time at Fraunhofer IFAM.

A profound thanks goes also to the technical staff of my department: Andreas Kruse, Sascha Korfe, Jürgen Loschen, Ralf Gentzsch, Iris Gottschalk and Katja Marnitz who supported me with their experience and expertise.

A bottomless thanks also to all my student assistants who contributed to this dissertation, especially to Jona Haupt, Thorben Steinberg, Marc Viehöfer and Tobias Evers — aka sharpest photographer Ever(s).

Special thanks goes to Prof. Andreas Hartwig for supporting and nominating me for the 'Adhesion Innovation Award 2023'. Without his belief in me, I would not have been honoured with this esteemed award.

Last but certainly not least, I want to wholeheartedly express my deepest gratitude to my incredible family, friends, and loved ones for their unwavering support! Without their encouragement and belief in me, this journey would not have been possible. Their presence in my life has been a constant source of inspiration and motivation. Thank you from the bottom of my heart for being there for me!

Abstract

This thesis proposes a methodology to optimize the application pattern of adhesively bonded joints, so that the liquid adhesive automatically flows into the desired bond shape during manufacturing — leaving no spots over- or underfilled, thus the adhesive is used in the most efficient way. Besides preventing adhesive excess and waste that eliminates the need for cleaning and reworking steps after joining, this optimization approach ultimately leads to a more ecological and economic adhesive manufacturing processes.

To achieve this goal, an optimization algorithm is developed that iteratively modifies the shape of adhesive application pattern until it flows into the desired bond shape. Established methods from topology optimisation for solids are used, re-interpreted, and applied in the context of fluid mechanics in a new way. At each iteration, the resulting distribution obtained after squeezing an initial adhesive application pattern is calculated. The *resulting* distribution is then compared to the *desired* adhesive distribution, and overflown adhesive is traced back to its origin in the initial pattern (using the calculated velocity and direction). These overflown areas are then removed from the initial pattern and the iteration loop continues until the resulting distribution matches the desired bond geometry within an acceptable tolerance.

This optimization strategy relies on the accurate simulation of squeeze flow processes for which a special numerical model was chosen. This model was extensively validated in a comprehensive experimental study in advance, to prove its suitability. By combining the Hele-Shaw approach, a method to investigate squeeze flow processes, with Particle Image Velocimetry, a method to measure fluid flows, it is demonstrated that the simulation model is sufficiently accurate and can be implemented to calculate the quantities that are required by the optimization algorithm. Further, the surface structure has proven to be of secondary importance and doesn't need to be considered in the optimization.

The algorithm was applied to optimize a variety of different application patterns. It was found that the optimized shapes have recurring shapes such as pointy *fingers* which flow into corners and *bays* that flow into straight edges. Furthermore, quantities like the degree of compression, number of cells and considered flow-laws were varied to investigate their influence on the algorithms results. However, it was found that the algorithm is mesh and

flow-law independent, which highly improves its applicability and simplicity for practical use. It is capable to identify optimal patterns for frequently used adhesive layer thicknesses and degrees of compression.

Finally, the optimized patterns obtained by theoretical analysis were validated through real world experiments, that confirmed their ability to flow into the desired shapes. Overall, this thesis presents an innovative approach to optimize adhesive application patterns. Due to the performed optimization, the environmentally questionable adhesive waste and costly post-cleaning work can be eliminated — thus, a more ecological and economical manufacturing process is achieved.

Kurzfassung

In dieser Arbeit wird eine Methode zur Optimierung von Applikationsmustern für geklebte Verbindungen entwickelt. Durch die Optimierung soll der flüssige Klebstoff beim Fügen automatisch in die gewünschte Fugengeometrie fließen — ohne danach über- oder unterfüllte Stellen zu hinterlassen. Durch das Vermeiden von Klebstoffaustritt werden Reinigungs- und Nachbearbeitungsschritte obsolet, was wiederrum zu einem sehr ökologischen und wirtschaftlichen Herstellungsprozess führt.

Hierfür wurde ein Optimierungsalgorithmus entwickelt, der iterativ die Form des Auftragsmusters modifiziert, bis es in die gewünschte Klebfugengeometrie fließt. Dabei wurden etablierte Methoden aus der Topologieoptimierung verwendet, neu interpretiert und im Kontext der Fluidmechanik angewandt. In jeder Iteration wird die resultierende Klebstoffverteilung, die sich nach dem Verpressen (Squeeze-Flow Prozess) eines Initialmusters ergibt, berechnet. Die resultierende Verteilung wird dann mit der gewünschten Klebfugengeometrie verglichen und übergeflossener Klebstoff zu seinem Ursprung im Initialmuster zurückverfolgt (mit Hilfe der berechneten Geschwindigkeit und Richtung). Diese überlaufenden Bereiche werden dann aus dem Initialmuster entfernt. Die Iterationsschleife wird so lange fortgesetzt, bis die resultierende Klebstoffverteilung innerhalb einer akzeptablen Toleranz mit der gewünschten Klebefugengeometrie übereinstimmt.

Diese Optimierungsstrategie beruht auf der genauen Simulation von Squeeze-Flow Prozessen, für die ein spezielles numerisches Modell verwendet wurde. Dieses Modell wurde im Vorfeld in einer umfassenden experimentellen Studie validiert, um seine Eignung nachzuweisen. Durch die Kombination des Hele-Shaw Ansatzes, einer Methode zur Untersuchung von Squeeze-Flow Prozessen, mit Particle Image Velocimetry, einer Methode zur Strömungsmessung, wird gezeigt, dass das Simulationsmodell ausreichend genau ist und in den Optimierungsalgorithmus implementiert werden kann. Darüber hinaus hat sich gezeigt, dass die Oberflächenstruktur der Fügeteile bei der Optimierung nicht mit berücksichtigt werden muss.

Der Optimierungsalgorithmus wurde an verschiedenen Klebfugengeometrien validiert. Dabei hat sich herausgestellt, dass die optimierten Initialmuster wiederkehrende Merkmale aufweisen, z.B. spitze *Finger* welche beim Verpressen in Ecken fließen oder *Buchten* welche

in gerade Kanten strömen. Darüber hinaus wurde der Grad der Kompression, die Anzahl der Zellen sowie die verwendeten Fließgesetze variiert. Dabei wurde festgestellt, dass der Algorithmus unabhängig von der Zell-Diskretisierung und dem verwendeten Fließgesetz ist, was seine Anwendbarkeit in der Praxis erleichtert. Es wurden optimale Muster für gängige Klebschichtdicken erzielt.

Schließlich wurden die optimierten Applikationsmuster experimentell validiert, wobei sich bestätigt hat das diese in die gewünschten Klebfugengeometrie fließen. Somit präsentiert diese Arbeit einen erfolgreichen und innovativen Ansatz zur Verbesserung von Herstellungsprozessen im Kontext der Klebtechnik. Umweltbedenkliche Klebstoffabfälle und kostspielige Nachbearbeitungsschritte werden hiermit obsolet, wodurch ein ökologischer und wirtschaftlicher Herstellungsprozess garantiert wird.

Contents

List of Abbreviations

Acronyms

AESO	Additive Evolutionary Structural Optimization
ANOVA	Analysis of variance
BESO	Bi-directional Evolutionary Structural Optimization
CFD	Computational Fluid Dynamics
ESO	Evolutionary Structural Optimization
FDM	Finite Difference Method
FEM	Finite Element Method
FVM	Finite Volume Method
HSC	Hele-Shaw cell
IDS	Institute of Dynamics and Vibrations
MoE	Modulus of elasticity
PDE	Partial Differential Equation
PFGM	Partially Filled Gap Model
PIV	Particle Image Velocimetry
SPH	Smoothed Particle Hydrodynamics
UTM	Universal Testing Machine
2D	Two dimensional
3D	Three dimensional

Symbols

b	Width
d	Distance of overflow
h	Gap height
k	Spring stiffness
l	Length
m	Mass, cells filling degree
n	Quantity, flow index
p	Pressure
t	Time
$\mathbf{u}$	Displacement vector
$\mathbf{v}$	Velocity vector
u, v, w	Velocity components in x-, y- and z-direction
x, y, z	Coordinates in space
D	Diameter
$\mathbf{D}$	Matrix with distances of overflow
F	Force
K	Body force, flow consistency index
$\mathbf{K}$	Stiffness Matrix
$\mathbf{M}$	Matrix with degree of filling
R	Radius
R_a	Arithmetic mean roughness
R_q	Root mean square roughness
R_z	Mean peak-to-valley height
RR	Rejection ratio, reduction ratio
ER	Evolution rate, elimination rate
V	Volume
α	Angle, compliance
$\dot{\gamma}$	Shear rate
η	Dynamic viscosity
θ	Contact angle
ρ	Density
σ_{vM}	von Mises stress criteria
τ	Shear stress
Δ	Change or difference of a quantity
Ω	Design domain, fluid domain

Indices

0	Initial state, position at $t = 0$
1	Next state, position at $t = t + \Delta t$
BC	Boundary condition
e	Element
exp	Experimental
fin	Final
i	Iteration step
$i + 1$	Next iteration step
ini	Initial
j	Matrix row variable
k	Matrix column variable
max	Maximum
min	Minimum
res	Result(ing)
t	Time step
$t + 1$	Next time step
th	Threshold
tar	Target
x, y, z	Directions in space

Part I

Opening Chapters: Problem, Practice and Proposed Solution

1 Introduction

Humans probably always strived to improve things. We've optimized our environment and found the tools needed. To make life simpler, easier. To fulfil our needs, whether basic or ambitious. Throughout history we hunted with bow and arrow to get food and built rockets to fly to the moon and fulfil our desire for exploration. The invention of bicycles, cars and aeroplanes have revolutionized the way we get from A to B faster and faster. Further, smartphones have fundamentally changed the way we interact and communicate socially. Despite being often overlooked, these inventions (and lots of others) have been significantly improved due to the application of adhesive bonding technology. Consequently, they have become more durable, reliable, secure, and last but not least cost-effective, which is why they are accessible to so many people today.

1.1 Scientific Problem

Although the technology of adhesive bonding highly improved our everyday products because of its many advantages, it does come with some challenges regarding manufacturing. These difficulties are mainly caused by the liquid state of the uncured adhesive. The achievement of a solid bond that precisely matches the desired geometry, transitioning from a liquid adhesive, is a highly challenging task. Adhesives do flow, even though there are some adhesives which are rheologically designed to remain in their applied shape during manufacturing. However, once the substrates are pressed together, the adhesive is forced to flow in-between the parts to be joined due to the squeezing process.

This is desired, as the adhesive begins to wet both surfaces and fills the bond. However, many things can go wrong here. It is commonly accepted that a huge amount of adhesive will spill out of the bond area, and no real thought is given to the design of the initial shape of the adhesive application pattern. Since there is no general understanding about how a good application pattern should look like, overfilling is even intended by design to prevent an underfilled bond domain at the cost of waste and additional cleaning steps. Furthermore, underfilling can occur, e.g. in the form of air bubbles, which can be caused by the trapping of air during the squeezing process. Both shortcomings — over- and underfilling — are ex-

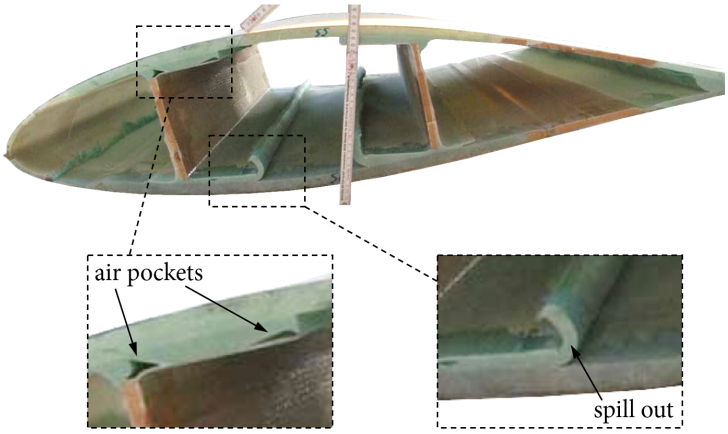

Figure 1.1: Cross section of a wind turbine rotor blade with air pockets (underfilling) and much adhesive spill out (overfilling), taken & edited from [106].

emplary illustrated in Figure 1.1. In a nutshell, adhesive bonding requires special attention with regard to the manufacturing process!

To make matters worse, the highly automated world of today's manufacturing industry offer many possibilities for the application of adhesives which are not fully utilized yet. In addition to the conventional stress and strength related topics, a more global view on adhesive bonding is needed. This includes the consideration of adhesive flow during joining with all the information about initial application pattern and the resulting adhesive distribution contained after the squeezing process. In this way, the advantages of modern manufacturing possibilities can be utilized to close the gap between common practice and what is technical possible. This thesis aims to narrow this gap by optimizing adhesive application.

1.2 Motivation

Optimizing adhesive application has significant implications for achieving more sustainable bonds. By reducing the amount of adhesive used and preventing over- and underfilling, several benefits can be realized. Firstly, it leads to economic advantages through waste reduction and material savings. Secondly, it contributes to environmentally friendly production practices by minimizing resource consumption. Additionally, the optimization of adhesive application streamlines manufacturing by reducing the number of required working steps and eliminating cleaning tasks. Moreover, it can enhance the aesthetics of bonded products, which is particularly crucial in the glass or automotive industry, where aesthetics play a pivotal role in product design. The research questions will be further refined and outlined in the Objectives, right after an overview of the State of the Art has been given.

2 State of the Art

2.1 Adhesive Manufacturing Processes

Manufacturing of adhesively bonded joints involves several steps, which must be coordinated according to the technical application. First, an adhesive needs to be selected so to fulfil the requirements of the specific application, cf. Figure 2.1 (a). The choice of adhesive is highly influenced by the desired strength and the materials that need to be bonded — however environmental conditions, curing time, cost, health, and safety as well as the adhesive application method are further factors to be considered for the selection.

The next step is the preparation of the surfaces of the substrates on which the adhesive will be applied to. Again, the preparation method that is used for the surfaces is depending upon the materials to be bonded. There are many surface pre-treatment methods, ranging in complexity from cleaning with solvents, sandblasting or grinding, to flame- or plasma-treatments, cf. Figure 2.1 (b) — to name only a few. All of them aim to modify the surface in a way that adhesion will benefit, and joint strength and durability are maximised.

Subsequently, the liquid adhesive is applied onto the substrate(s). The final shape of the adhesive bead, and method used to apply the adhesive onto the surface(s) influences the resulting bond geometry as well as the amount of adhesive spill out and underfilling — a topic this thesis will investigate in much detail. Adhesive application can be either done manually, cf. Figure 2.1 (c), using a cartridge press (which is fast and simple for single components), or by using robots/xyz-Tables in combination with dispensers and dosing systems (which is automatable and repeatable for a high number of pieces).

After applying the adhesive onto the substrate(s) they can be joined, cf. Figure 2.1 (d). Pushing the substrates against each other, the relative motion of the closing gap between the substrates forces the adhesive to flow in-between them whereby it wets both surfaces, cf. Figure 2.1 (e). This process is called *squeeze flow* — another topic that will be comprehensively investigated in this thesis.

It is worth noting that there are other exciting joining methods for bonding that deserve mention, such as the injection of adhesive in-between already final positioned substrates. Additionally, the last step of every manufacturing process, i.e. the curing process, depicted

in Figure 2.1 (f), should also be mentioned here for the sake of completeness. It has been dealt with in a recent dissertation [93], in which a method to accelerate the curing process using inductive heating was developed.

(a) Adhesive selection

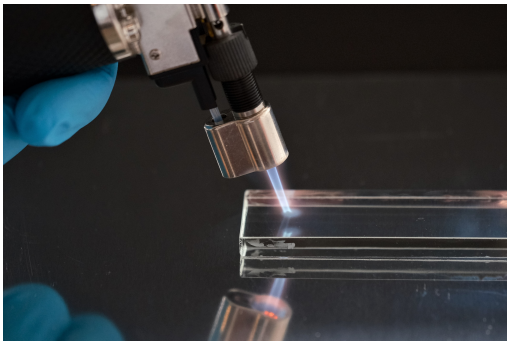

(b) Surface pre-treatment

(c) Adhesive application

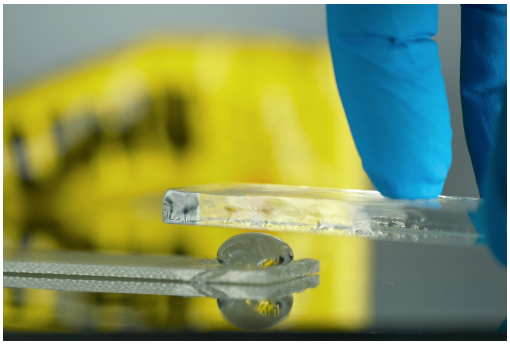

(d) Before joining

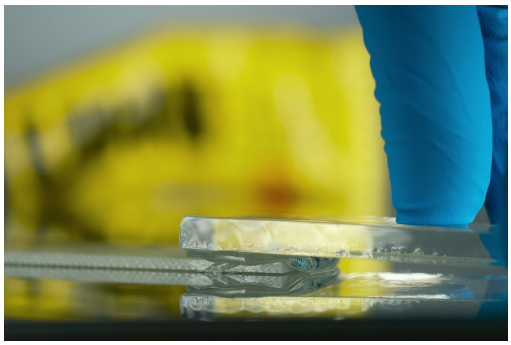

(e) After joining

(f) Curing process

Figure 2.1: Manufacturing process of adhesively bonded joints.

2.2 Experimental Investigations on Adhesive Squeeze Flow

Squeeze flows are defined as *flows in which a material is deformed due to a squeezing motion of some boundaries that approach each other*. Unlike pipe or channel flow, squeeze flow does not rely on gravity to generate motion, but it is primarily driven by the kinematics of the squeezing process. Materials that can experience squeeze flow are usually non-solid and highly viscous liquids — properties that apply to a wide range of adhesives in their liquid state. The boundaries — or, in the context of adhesive bonding, the substrates — in-between which the fluid is squeezed, can either be rigid or non-rigid and can have a certain surface structure. The squeeze process is described by the relative motion of the substrates from an initial to a final state, following defined kinematics (e.g. translation, rotation or a combination thereof). Hereby, the topology of the substrates can be flat or arbitrarily shaped and the position can be parallel or inclined to each other, cf. [30].

A widely used device to investigate adhesive squeeze flows consists of two parallel plates with an initial gap height of h_0 that approach each other with a constant velocity w, until they reach a final gap height of h_{fin}, as illustrated in Figure 2.2. In this setting, the fluid's thickness is always considered much smaller than it's spread. Furthermore, the volume of the fluid can be kept constant, by allowing it to spread in-between some *infinitely large* surfaces; or the squeezing area can be kept constant, by allowing the fluid to squeeze out of *finite sized* surfaces right from the beginning [20]. In the first case, the fluid will spread into a circular shape if the gap becomes small enough ($h_{\text{fin}} \ll h_0$ or $h \to 0$), independent of the initial shape.

A visually easy to grasp illustration of experimental squeeze flow was carried out by J. M. Adams et al. [1]. The researchers conducted an investigation into the behaviour of squeeze flow with a material called *plasticine*. Their objective was to validate a finite element

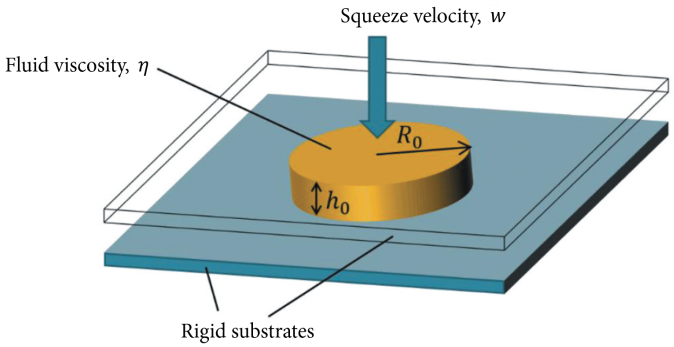

Figure 2.2: Squeeze flow scenario of a circular fluid pattern under compression, taken & edited from [67].

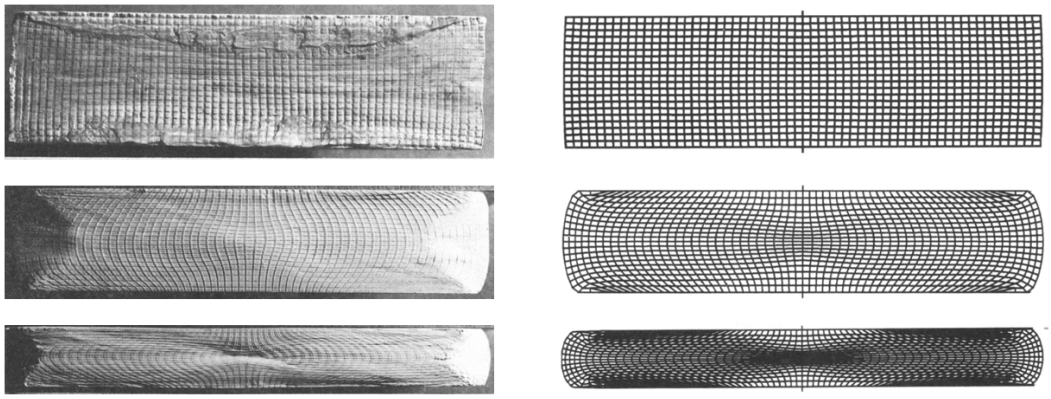

Figure 2.3: Displacement field of an elasto-viscoplastic paste material during squeeze flow (2D): experiment (left), simulation (right) for 13%, 29% and 52% compressive deformation, taken from [1].

simulation that utilized an elasto-viscoplastic material model. To carry out the experiment, they prepared specimens with a grid pattern on the cross section and subjected them to squeezing in-between two parallel stiff stainless steel plates, that were attached to a testing machine. With this procedure, they were able to measure and accurately predicted the 2D displacement field through numerical simulation, as depicted in Figure 2.3. Similar studies, such as [60] and [61, 62] have further explored the compaction process of soft pastes and solids. However, more details regarding the numerical simulation of squeeze flow scenarios will be presented in section 2.4.

2.2.1 The Hele-Shaw Approach

The modern investigations on flows within narrow gaps can be traced back to the pioneering work of Henry Selby Hele-Shaw. He served as an early source of inspiration for subsequent research with his studies on *The flow of water*, which he published in the late 19th century [27–29]. Hele-Shaw developed a specialized device known as the Hele-Shaw cell (HSC), named after him, that consists of two closely and parallel spaced, stationary glass panes in-between which a flow can be generated and observed at the same time. Using this apparatus, he explored various flow scenarios, including the flow of water around a semi-cylinder. He concluded that, in this case, the experimentally observed flow patterns aligned with those theoretically predicted based on hydrodynamic principles [29, p. 35]. However, in this classical or original forms of the HSC, the gap between the plates was constant and the flow is generated by injection or a pump circuit.

Further developments led to cells that have moving surfaces which can squeeze the fluid to

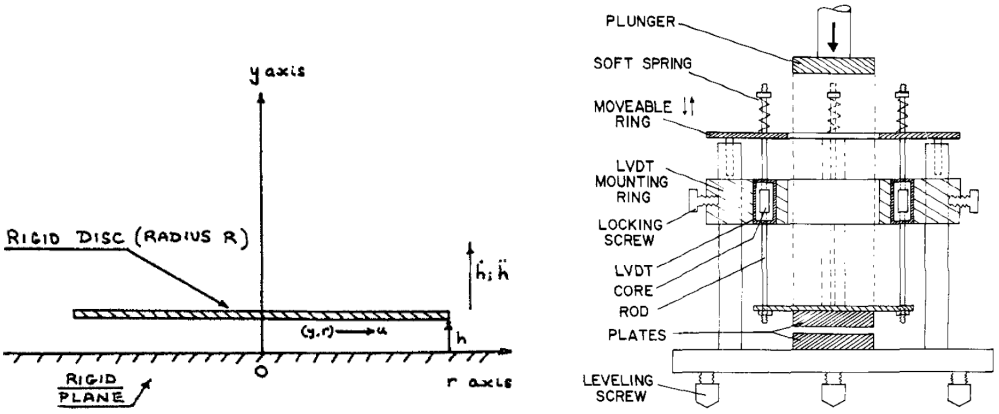

(a) Model sketch of the general squeeze flow problem, taken from [40].

(b) Experimental setup for the investigation of squeeze flows, taken from [52].

Figure 2.4: Description and investigation of squeeze flow problems.

obtain and observe its flow, as illustrated exemplary in Figure 2.4. Some of these adaptations, like the lifting HSC (as referenced in [2]), facilitate an expansion of the gap size, while others, such as the closing HSC (discussed in [46]), enable its reduction. These specialized cells usually have circular plate geometries and serve dual roles: *pulling* fluids, a process that also gives rise to viscous fingering (more on that in subsection 2.2.5) and compressing fluids to investigate fluid rheology and squeeze flow behaviour. The lifting HSC, in particular, finds application in investigating potential setbacks and relaxation effects that may occur in the context of adhesive bonding after pressing the substrates together and subsequently releasing the clamping force.

2.2.2 Surface Condition and Pre-treatments

There are different methods to characterize the quality and condition of surfaces to evaluate the effect of the pre-treatment applied. One popular and simple way is to estimate the surface energy by measuring the contact angle θ between the liquid-vapour interface (e.g. water-air) meeting the solid substrate surface [26]. Depending on the resulting contact angle, the state of the surface can be quantified as hydrophilic ($\theta < 90°$), hydrophobic ($\theta \approx 90°$) and superhydrophobic ($\theta > 90°$). The smaller the contact angle the better is the surface condition for bonding.

Another method to characterize the quality and condition of a surface is to measure its roughness. This can be done in different ways, but the most practical oriented methods aim to determine the arithmetic mean deviation, also known as arithmetic mean roughness R_a,

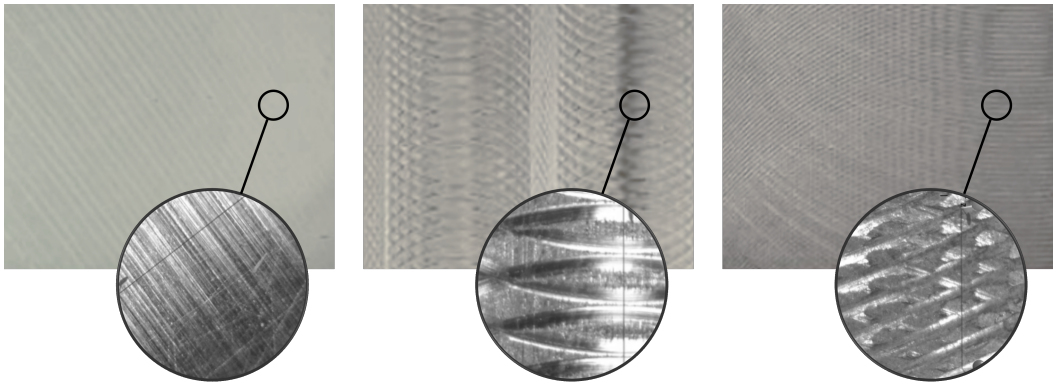

Figure 2.5: Surface structure of milled aluminium plates with maximum mean surface roughness of $R_a = 0.26\,\mu m$ (left), $R_a = 4.91\,\mu m$ (middle) and $R_a = 7.82\,\mu m$ (right), taken & edited from [7].

along a profile (line) – even thought this is also possible on a surface (area). Based on the characteristics of the surface, more parameters such as the root mean square roughness R_q or the mean peak-to-valley height R_z are needed for characterization, since the same R_a can be measured on totally different surfaces.

It is common practice to prepare surfaces before bonding [26], for which a plethora of different methods, ranging from simple cleaning with organic solvents, roughening, flame- or plasma-treatments, exist [6]. The goal thereof is to improve wettability, and thus increase adhesion to the substrate, in order to maximize joint strength and durability [26]. Mechanical surface pre-treatments aim to increase the surface roughness; these methods include e.g. sanding, brushing and blasting [79], and increase mechanical interlocking; they are the preferred methods for (uncoated) metals. Physical pre-treatment methods aim to introduce oxygen atoms into the surface and include flame treatment and different plasma treatments [85]; they are often used with polymers [49]. Chemical surface pre-treatments are used to remove contaminants, oxide layers, and enhance surface compatibility, ultimately ensuring strong and durable bonds [4]. However, all these pre-treatment methods may modify the surface in terms of roughness or surface energy, thus raising the question if they influence the fluid dynamics of the squeeze flow itself.

Biszczanik et al. [7] used a setup similar to the closing HSC to investigate the adhesive spread and the compressive force applied, generated on different substrate surface structures. In their investigation a polyurethane adhesive was squeezed between milled aluminium plates, see Figure 2.5, with mean surface roughness ranging from $R_a = 0.26\,\mu m$ to $7.82\,\mu m$. The authors concluded that the roughness of substrate's surfaces does not sig-

nificantly affect the resulting thickness under otherwise identical test conditions.

Further studies considered rough surfaces to squeeze fluids to manipulate the fluid-solid boundary conditions, e.g. slip ($v_{BC} > 0$) vs. no-slip ($v_{BC} = 0$). Therefore Rabideau et al. used P180 grit sandpaper, with avg. particle diameter of 82 µm, as surfaces to squeeze samples of Carbopol at low forces of 1 N, 2 N, and 3 N. They reported that this roughness "*was deemed sufficient for preventing wall slip*" [77]. Subsequently they measured the height as function of time and observed differences between the smooth and rough surfaces. However, although they considered the stiffness of the experimental setup and corrected the height measurement by subtracting the deformation of the experimental setup, it is not finally clear if the observed differences in height may also just result from deviations of the recalibration (zeroing) done after attaching the sandpaper, cf. [46]. So, it remains unclear if pre-treated surfaces for adhesives influence the dynamics of squeeze flows or not.

2.2.3 Adhesive Application Methods

There are different ways to apply adhesives or sealants onto the substrates. The first and probably most simple and common way is to apply adhesive in form of a *bead*, i.e. dispensing and extruding it onto a surface with a certain bead cross section. Furthermore, the adhesive can be applied in form of *swirls* or (*flat*) *streams*, as shown in Figure 2.6. It is also possible to *spray* the adhesive onto the substrates [16]. Since this thesis focuses on adhesive bead application, further details are given subsequently.

Depending on the specific technical application, the applied beads have different cross sections, e.g. D-shaped, rectangular or triangular, created by the design of the application nozzle. The latter have the advantage to reduce the risk of air entrapment during the joining process because the tip of the triangle is less likely to already enclose some air. One disadvantage of bead application is that they often have a surge at the beginning, leading to squeeze out, and the material may lead to filament formation at shut-off [59].

To apply adhesives in more complex shapes, the *dam* & *fill* method can be applied. With this method, a dam is first applied which defines the outer contour and is subsequently filled. In contrast to application methods that are similar to 3D printing or those which work with negative forms, the *dam* & *fill* method can be implemented using simple dispensers linked to a robot or xyz-Table. The dam is usually formed with a highly thixotropic (stable) fluid and is subsequently filled with a low viscous (flowable) fluid.

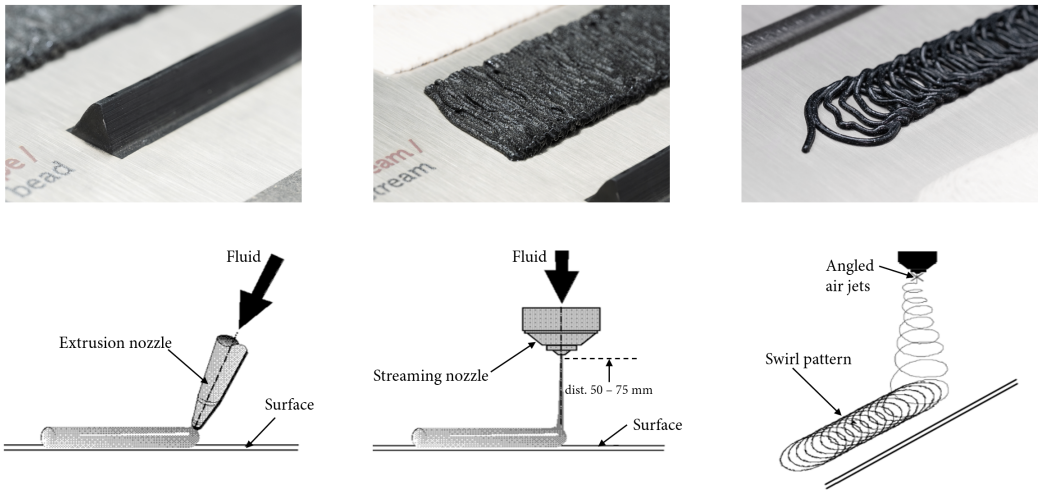

Figure 2.6: Adhesive application methods: extruding a bead (left), flat stream (middle), swirling technique (right), taken & edited from [59].

2.2.4 Formation and Influence of Air Pockets

Air enclosures in adhesive bonds are imperfections that can arise during various stages, including squeeze flow, application, or substrate relaxation after joining. These enclosures encompass both air bubbles, typically small and pre-existing in the adhesive container, and larger air pockets formed during the squeezing process by trapped air. Air enclosures can also form during the adhesive application process or by setback (relaxation) of the substrates after joining. The presence of such voids can significantly compromise the load-bearing capacity of the bonded joint, especially under dynamic loads (fatigue stress), as they amplify stress concentrations and cumulative damage.

Researchers, such as Sengab and Talreja [83], have explored the impact of void shapes on load capacity, noting that spherical air enclosures are less critical than flat voids in terms of initiating and propagating cracks. Additionally, voids can expedite moisture migration, a concern in sealing bonds. In the pursuit of optimal bonding, the goal is to achieve a fully filled gap with minimal material excess and a complete absence of air enclosures. Researchers like Müller et al. [69] have experimentally and numerically investigated artificially induced air pockets during squeeze flow, observing that these air pockets tend to migrate towards the adhesive layer's edge, where they may discharge and vanish.

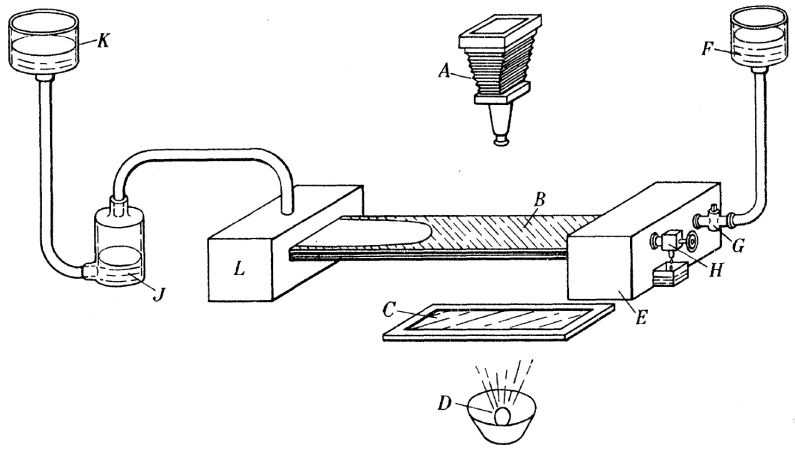

Figure 2.7: Arrangement of long Hele-Shaw cell for observing flows with a photo camera. "*The camera A points vertically downwards at the channel B which is illuminated by a flash-bulb D placed under a tracing-paper screen C. The driving pressure was produced by raising a water vessel K so as to increase the air pressure in the bottle J. This raised the pressure above the fluid contained in the upstream reservoir L. The more viscous fluid was supplied from a vessel F, so as to fill the upstream reservoir E. If the pressure in E were maintained constant, as it would be if the pipe connecting E and F were left open, the velocity of the finger would increase as the length of the column of more viscous fluid decreased. To maintain a more constant velocity the cock G between E and F was closed during an experiment and the fluid in E escaped to the atmosphere through a needle valve H*", taken from [80].

2.2.5 Phenomena of Viscous Fingers

Viscous fingering, a phenomenon of considerable interest, is investigated within modifications of HSCs, developed by Saffman and Taylor. They aimed to investigate and mathematically describe the penetration of fluids into more viscous liquids. For example, they injected water into oil, using a long channel HSC shown and described in Figure 2.7 and observed that morphologically unstable interfaces, which are shaped like fingers, emerge in this process, shown in Figure 2.8. This phenomenon is referred to as Saffman–Taylor instabilities or simply *viscous fingering* and can occur with other fluids including adhesives.

Engaging flow patterns manifest when two adjacent surfaces, already containing a fluid, are separated. This separation triggers pronounced instability at the initial fluid-gas interface [80], leading to the advancement of so-called viscous fingers (corridors of air) into the fluid, while other regions of the interface experience minimal displacement [31]. These fingers exhibit a propensity to bifurcate at their tips, engendering the formation of new fingers, ultimately yielding a densely branched interfacial structure, as shown in Figure 2.9. Viscous

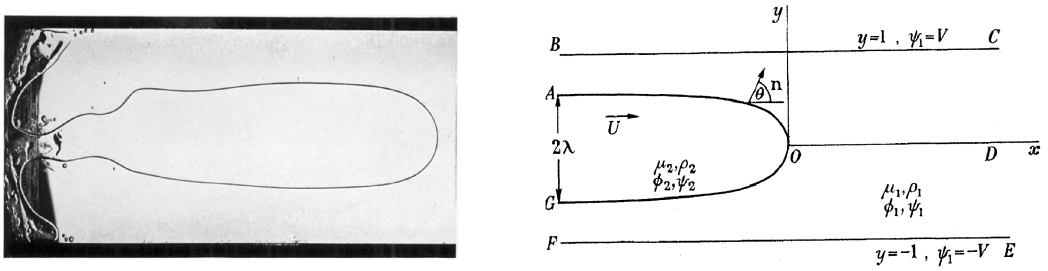

Figure 2.8: Air finger advancing into a more viscous liquid. "*A bubble of fluid of viscosity μ_2 and density ρ_2 is supposed to be moving steadily through a vertical channel in the Hele-Shaw cell filled with fluid of viscosity μ_1 and density ρ_1*", taken from [80].

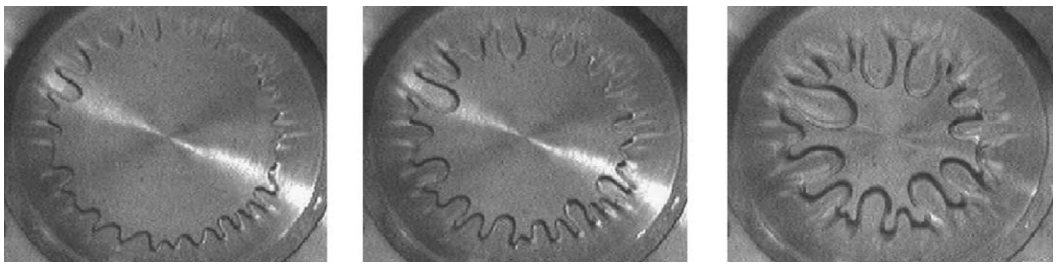

Figure 2.9: Evolution of viscous fingers in a lifting HSC at three different times; the initial gap height is 0.5 mm with a diameter of 40 mm, taken from [2].

fingers are also investigated with circular stationary HSCs, whereby the less viscous fluid is injected centrally through an inlet [13].

2.3 Particle Image Velocimetry

So far, flows in narrow gaps have been visualized by its moving interfaces or sometimes artificial streamlines and grids. However, there are more advanced methods to measure flows, one of which is Particle Image Velocimetry (PIV). It is an optical method to measure the characteristics, i.e. velocity, direction, shear rate and other related properties of fluid flows in two dimensions (2D).

2.3.1 Methodology

To visualize fluid flows, light, small and easily visible particles are introduced into the fluid, and their movement is employed for tracking purposes. A camera captures images at brief, sequential intervals, as depicted in Figure 2.10. Later, specialized PIV software, such as OpenPIV or PIVLab [86, 87], among others, can be utilized for analysis. This software

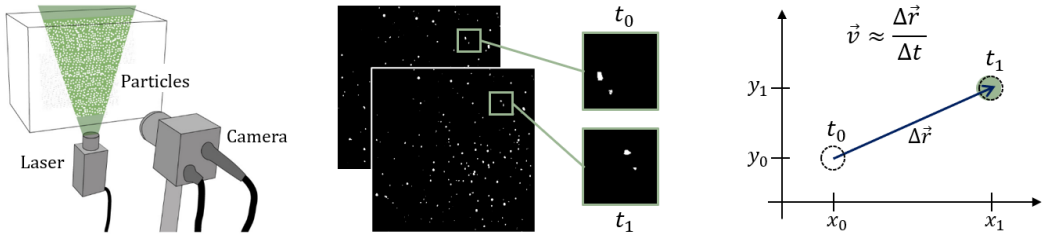

Figure 2.10: Methodology of Particle Image Velocimetry: schematic experimental setup (left, taken from [87]), exemplary successive frames of a flow field (middle) and principle of the velocity calculation (right).

computes a velocity field by comparing pairs of successive frames in the recorded data.

Using digital cross correlation, any finite location (group of pixels) of one frame can be assigned to the next frame with the information of its displacement in x and y direction: $\Delta\vec{r} = (x_1 - x_0 \mid y_1 - y_0)$. With the additional information of time difference between both frames, $\Delta t = t_1 - t_0$, and a scale that links a number of pixels to a real length, the velocity vector, $\vec{v} = (u \mid v)$, at a certain location can be quantified according to Eq. 2.1:

$$\vec{v} \approx \frac{\Delta\vec{r}}{\Delta t}. \tag{2.1}$$

Incorporating a laser, along with a synchronizer that acts as a simultaneous trigger for the camera and laser, offers distinct advantages. This arrangement allows for illuminating the flow precisely when a frame is captured. Consequently, it enhances image quality, which, in turn, significantly improves the quality of the PIV results during post-processing.

The methodology can be extended to three dimensional (3D) measurements by using two or more cameras with different viewing angles, which collect the needed information of flow in the third dimension (z-direction). The discretization of 3D PIV can be increased by adding more cameras and laser planes. For more information on established 3D PIV setups, e.g. dual-plane stereoscopic PIV, the author refers the interested reader to [32].

2.3.2 Particles

The particles used for PIV need to be selected depending on the fluid and application to be investigated. Most important, the density of the particles should match to the fluid, to avoid floating (occurring if $\rho_{\text{Particle}} < \rho_{\text{Fluid}}$) or sinking (occurring if $\rho_{\text{Particle}} > \rho_{\text{Fluid}}$) – fine-tuning is possible by exploiting the temperature dependence of the fluid density. However, the need for equal density diminishes with increasing fluid viscosity, especially for highly viscous fluids which most adhesives are.

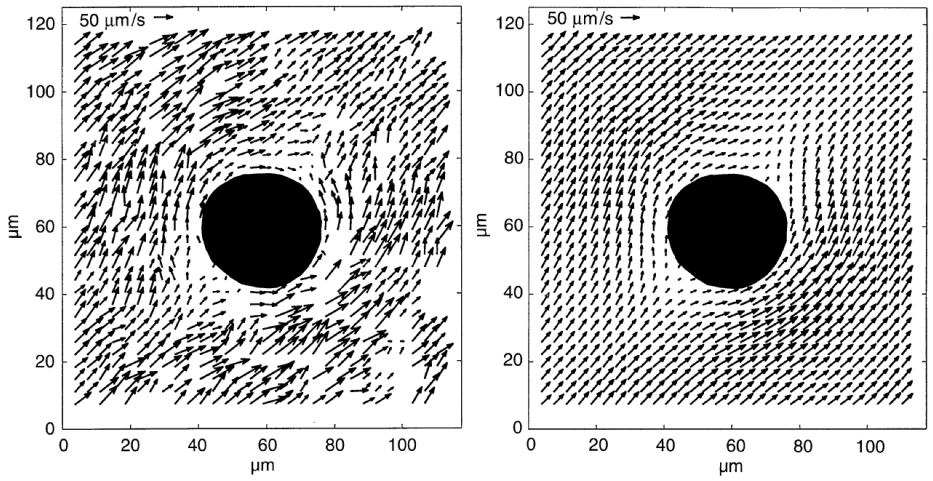

Figure 2.11: Flow around a cylinder measured with PIV: Instantaneous velocity field (left) and eight-image ensemble-averaged velocity field (right), taken from [81].

Typical particles can be glass, polystyrene or polyethylene beads or aluminium flakes. Ideal particles are spherical and small (approx. $10-100\,\mu m$) so that, in combination with the camera setup, the diameter results in around three pixels in the recorded image, as recommended by [87]. If chosen properly, the effect of the particles on the fluid flow is negligible [63].

2.3.3 Examples

A few examples are mentioned to illustrate the possibilities of PIV. The methodology can be applied to a variety of flow cases, including Hele-Shaw flows as done by Santiago et al. back in 1998 at small scale [81]. They were able to measure the flow around a cylindrical obstacle with a diameter of approximately only $30\,\mu m$ in size. By further combining multiple measurements they could ensemble the average flow profile around that cylinder, as shown in Figure 2.11.

PIV can also be applied for engine flow measurements [19], to track granular flows [57] or the movement of soil [105] where the medium itself corresponds as the particles. Phenomena such as hydraulic ground failure [48] were measured using PIV, as shown in Figure 2.12. The ground failure can be caused by a granular flow that is driven by a hight difference of the water level in the soil, as is the case for construction pits or dams. Further, Yuan et al. [105] applied the method of PIV to measure the deformation of piles under horizontal loads.

PIV can be applied at different scales, starting with micro-PIV [21] where the particle size

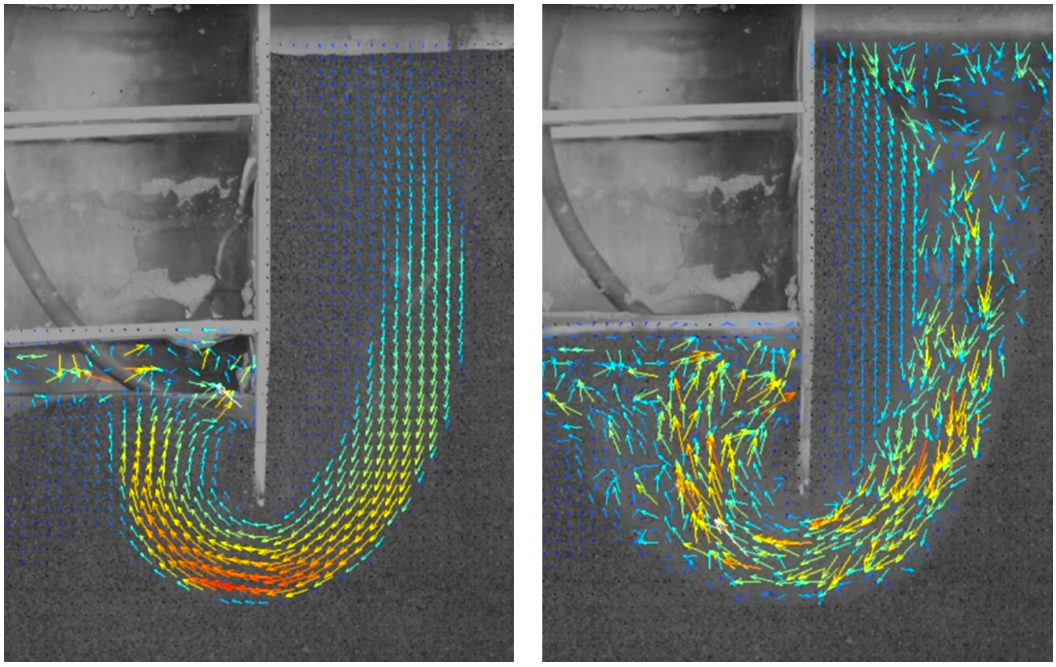

Figure 2.12: Soil just before (left) and immediately after (right) hydraulic ground failure analysed with Particle Image Velocimetry (PIV), source: IBU Institut für Bau und Umwelt YouTube channel, see the video, accessed on 25. July 2023.

is given in nanometres, ranging between 200 nm and 2000 nm [95]. On the other side, PIV can be applied at large scales as done in [90] where the authors used snow as the particles to measure the atmospheric boundary layer with a measurement area of approximately 22 m × 52 m and up to 56 m above the ground. Furthermore, recent advancements enabled the application of PIV to more complex and turbulent flows [96].

2.4 Numerical Simulation of Flows in Narrow Gaps

2.4.1 Computational Fluid Dynamics

Computational Fluid Dynamics (CFD) is a widely used numerical method to solve and analyse fluid mechanic problems. Such fluid flow problems usually can no longer be solved with analytical methods because of their non-linear nature and complex geometry. CFD numerically solves the Navier–Stokes equations, a set of partial differential equations, which describe fluid flows. For an incompressible Newtonian fluid in three dimensions (3D), they can be written in the form of Equation 2.2:

$$
\begin{aligned}
\rho \cdot \left(\frac{\partial u}{\partial t} + \frac{\partial u}{\partial x} u + \frac{\partial u}{\partial y} v + \frac{\partial u}{\partial z} w \right) &= K_x - \frac{\partial p}{\partial x} + \eta \cdot \left(\frac{\partial^2 u}{\partial x^2} + \frac{\partial^2 u}{\partial y^2} + \frac{\partial^2 u}{\partial z^2} \right) \\
\rho \cdot \left(\frac{\partial v}{\partial t} + \frac{\partial v}{\partial x} u + \frac{\partial v}{\partial y} v + \frac{\partial u}{\partial z} w \right) &= K_y - \frac{\partial p}{\partial y} + \eta \cdot \left(\frac{\partial^2 v}{\partial x^2} + \frac{\partial^2 v}{\partial y^2} + \frac{\partial^2 v}{\partial z^2} \right) \\
\rho \cdot \left(\frac{\partial w}{\partial t} + \frac{\partial w}{\partial x} u + \frac{\partial w}{\partial y} v + \frac{\partial u}{\partial z} w \right) &= K_z - \frac{\partial p}{\partial z} + \eta \cdot \left(\frac{\partial^2 w}{\partial x^2} + \frac{\partial^2 w}{\partial y^2} + \frac{\partial^2 w}{\partial z^2} \right)
\end{aligned}
\tag{2.2}
$$

were x, y and z are the cartesian coordinates; u, v and w are the corresponding fluid velocities; ρ is the fluid's density; η is the fluid's dynamic viscosity; p the pressure; and K_i the body forces, i.e. gravity, cf. [66]. They mathematically express the conservation of mass, momentum and energy within a fluid continuum and can be further connected by an equation of state to relate pressure, temperature, and density. With sufficient initial- and boundary-conditions, this system of equations can be solved numerically by a variety of methods, which either utilize finite magnitudes, such as the Finite Element Method (FEM), Finite Volume Method (FVM) and Finite Difference Method (FDM), or mesh-free Lagrangian approaches such as Smoothed Particle Hydrodynamics (SPH). The solution of the Navier-Stokes equations is the fluid flow velocity and direction at any given point in space (and time, if the flow is non-stationary, i.e. transient). Based on the velocity vector field, further quantities of the flow, including pressure or temperature, can be post-calculated. CFD simulations need a high amount of computing power and time, and depending on the problems complexity, they are solved on server clusters or are not possible to solve at all.

Simon Ingelsten et al. [39] proposed a method, that combines the FVM with backward tracking Lagrangian-Eulerian approach to simulate planar viscoelastic squeeze flows. Their study aims to validate the numerical method for such flows and assess the grid resolution dependence of important flow quantities. Results show that the load on the solids can be accurately predicted with a relatively coarse grid. The study also demonstrates good agreement with theoretical predictions and previous numerical results. The influence of different viscoelastic properties, particularly shear-thinning, is investigated using the model. Additionally, a reverse squeeze flow simulation highlights important aspects in adhesive joining applications. However, they only presented results for 2D cases, like similar studies, about transient squeeze flow of viscoplastic materials like [43].

There are a variety of commercial (e.g. *Ansys Fluent*) and non-commercial (e.g. *OpenFOAM*) CFD software solutions available, most of which utilize the FVM to solve the Navier-Stokes equations. There is also other simulation software that makes certain assumptions and simplifications to cut computation time to be able to address more specific flow prob-

lems. Many of these software tools are developed by universities and research institutes to investigate specific flow cases. The Institute of Dynamics and Vibrations (IDS) at the Technical University of Braunschweig has developed a simulation tool called Partially Filled Gap Model (PFGM), which is especially suitable for the simulation of flows in narrow gaps, including squeeze flows [66]. It is kindly provided by the IDS and used in this thesis after prior validation. The functionality of the PFGM is described below.

2.4.2 Partially Filled Gap Model

The fundamental concept behind the Partially Filled Gap Model (PFGM) is to achieve a balance between high numerical precision and efficient computation when simulating flows in narrow gaps. This is accomplished by strategically simplifying the complete Navier–Stokes equations through various assumptions tailored to the context of adhesive squeeze flows. This approach draws inspiration from the work of Reynolds [78], who, over a century ago, devised a highly effective description for lubricated flows based on the Navier–Stokes equations.

The first and most important assumption is that flow in the gap height direction, i.e. the z-direction, can be neglected as there are no significant pressure gradients in this direction, consequently the third part of Equation 2.2 is dropped, cf. [66]. Further simplifications result from the fact that, the gap height, h, is usually much smaller than the length, l, and width, b, dimensions of the squeezed fluid ($h \ll l$ and $h \ll b$), thus the dominating terms in the Navier–Stokes equations are those that consider the pressure gradients and the shear stress derivatives in the thickness, i.e. the z-direction, cf. [66]. That said, the other terms of the equation do not significantly contribute to the equilibrium and thus might be neglected. Furthermore, the flow can be considered to be laminar, and gravity is of secondary importance because of the high viscosity of the adhesive. According to all these model assumptions, the Navier–Stokes Equation 2.2 simplify to Equation 2.3:

$$\begin{aligned} \frac{\partial p}{\partial x} &= \eta \cdot \frac{\partial^2 u}{\partial z^2} \\ \frac{\partial p}{\partial y} &= \eta \cdot \frac{\partial^2 v}{\partial z^2} \end{aligned} \tag{2.3}$$

In this simplified form of Equation 2.3, all shear stresses due to the derivatives in x- and y-direction as well as the inertia-related (convective) terms vanished, which is well justified and proven according to literature of lubricated contacts, cf. [66].

Similar to CFD the PFGM uses cuboid shaped cells (instead of nodes of finite elements) to discretise the fluid domain into an equidistant cartesian mesh (spatial discretization: Δx

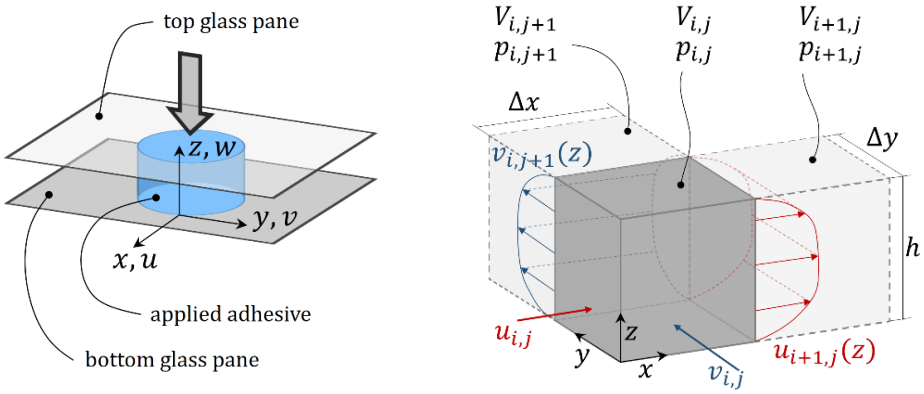

Figure 2.13: Schematic PFGM squeeze flow problem with circular fluid domain including coordinate definitions (left) and one representative fluid cell with neighbourhood conventions and state variables (right), taken from [46].

and Δy), as shown in Figure 2.13. However, due to the first assumption, only one cell is used for the discretisation in z-direction, meaning that the height of each fluid cell directly corresponds to the gap height h. In addition, the flow velocity between two neighbouring cells, i and $i+1$ (for the x-direction) or j and $j+1$ (for the y-direction), is modelled with a quadratic and symmetric function, i.e. the flow profiles $u(z)$ and $v(z)$, for which the no-slip condition are implied. The no-slip condition states, that the velocity at the fluid-surface interface is zero, i.e. $u(z=0)=0$, $u(z=h)=0$ and $v(z=0)=0$, $v(z=h)=0$. In addition to the velocities u and v, each cell is assigned with a pressure p and a fluid volume V (which can also be expressed as a degree of filling: $\Theta = {}^{V}/_{V_{\text{gap}}}$, with $V_{\text{gap}} = h \cdot \Delta x \cdot \Delta y$). The volume of a cell is a known quantity, which has been calculated in a previous time step or it is initially known by condition. The time, labelled by the index t, is discretised into finite time steps, Δt, whereby the index $t+1$ refers to the next time step at $t + \Delta t$.

Subsequently, the strategy of the PFGM to solve this system of equations is explained in short form. More details about the strategy can be found in [46, 66–68]. At first the pressure is calculated according to the method of artificial compressibility, cf. [50], as stated by Equation 2.4.

$$p_{ij}^{t+1} = \begin{cases} 0, & \text{if } V_{ij}^{t+1} \leq V_{ij,\text{gap}}^{t+1} \\ \overline{E} \cdot \left(V_{ij}^{t+1} - V_{ij,\text{gap}}^{t+1} \right) / V_{ij,\text{gap}}^{t+1}, & \text{if } V_{ij}^{t+1} > V_{ij,\text{gap}}^{t+1} \end{cases} \tag{2.4}$$

Once the pressure is known, the velocities can be calculated according to the simplified 2D Navier–Stokes Equation 2.3. Therefore, the partial derivative terms are approximated

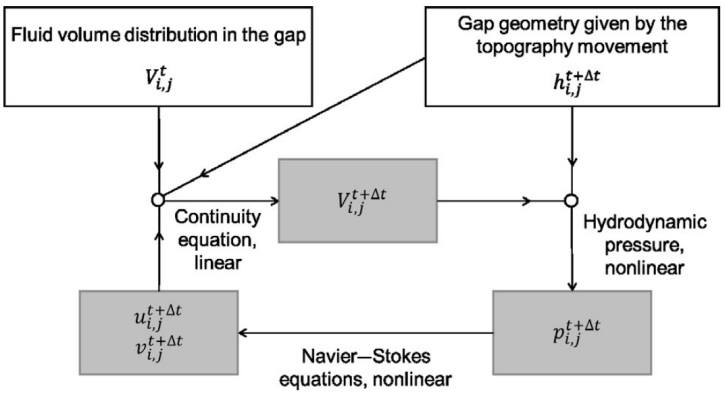

Figure 2.14: Constitutive laws and their interaction within the PFGM, taken from [69].

with a finite difference scheme, using the central difference quotients, resulting in Equation 2.5 for the first derivative:

$$\begin{aligned} \left.\frac{\partial p}{\partial x}\right|_{i,j} &\approx \frac{p_{i,j} - p_{i-1,j}}{\Delta x} \\ \left.\frac{\partial p}{\partial y}\right|_{i,j} &\approx \frac{p_{i,j} - p_{i,j-1}}{\Delta y} \end{aligned} \tag{2.5}$$

and Equation 2.6 for the second derivatives:

$$\begin{aligned} \left.\frac{\partial^2 u}{\partial z^2}\right|_{i,j} &\approx -\frac{12 \cdot u_{ij}}{h_{i,j}^2} \\ \left.\frac{\partial^2 v}{\partial z^2}\right|_{i,j} &\approx -\frac{12 \cdot v_{ij}}{h_{i,j}^2} \end{aligned} \tag{2.6}$$

The last step is the calculation of the volume distribution for the next iteration step, given by Equation 2.7:

$$\begin{aligned} V_{i,j}^{t+1} = V_{i,j}^{t} + \Bigg(& u_{i,j}^{t+1} \cdot \frac{V_{i-1,j}^{t+1} + V_{i,j}^{t+1}}{2\Delta x} - u_{i+1,j}^{t+1} \cdot \frac{V_{i,j}^{t+1} + V_{i+1,j}^{t+1}}{2\Delta x} \\ & + v_{i,j}^{t+1} \cdot \frac{V_{i,j-1}^{t+1} + V_{i,j}^{t+1}}{2\Delta y} - v_{i,j+1}^{t+1} \cdot \frac{V_{i,j}^{t+1} + V_{i,j+1}^{t+1}}{2\Delta y} \Bigg) \cdot \Delta t \end{aligned} \tag{2.7}$$

This set of implicit non-linear equations is iteratively solved with a Newton-Method based algorithm. Their relationship is further illustrated in Figure 2.14

Subsequently, a short simulation example is presented to show some general results to

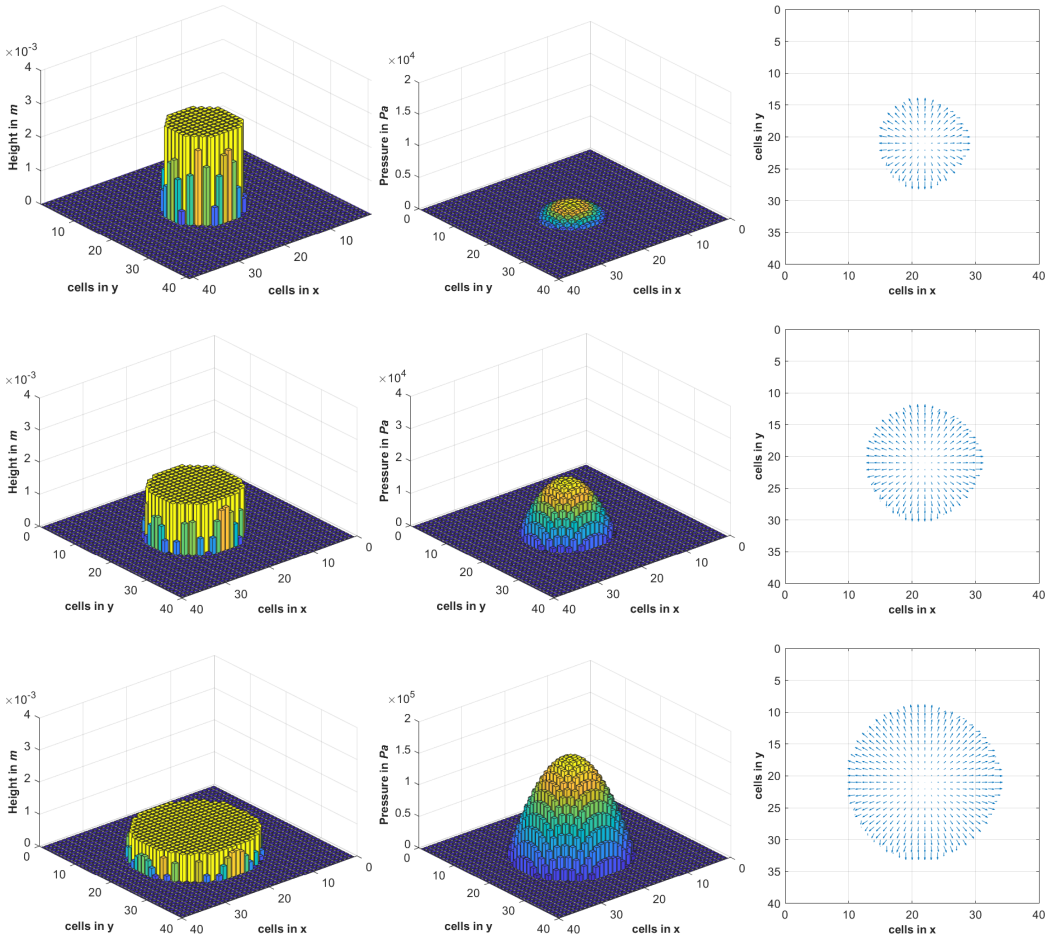

Figure 2.15: PFGM simulation results of a circular adhesive pattern that is being squeezed: fluid and gap height (left), pressure distribution (middle) and fluid velocity field (right), for three different time steps (top to bottom).

illustrate the functionality and capabilities of the PFGM. The example considers a circular fluid shape, that is squeezed. Despite the fact that the PFGM is able to calculate quantitative results, at this stage the results are presented in a qualitative way. It can be seen that the fluid height decreases as its diameter increases, i.e. it continues to spread in a circular shape throughout the entire squeezing process, which is shown for three different steps in time in Figure 2.15 (left). The pressure distribution looks like a parabolic dome and increases during the squeezing process, see Figure 2.15 (middle). Furthermore, according to the velocity vector fields which are shown in Figure 2.15 (right), it can be seen that the fluid spreads always outwards.

Since the PFGM includes several simplifications and assumptions it will be experimen-

tally validated in Part II to prove its usability to solve the objective of this thesis — the optimization of adhesive application pattern — which is addressed in Part III. However, in order to complete the simulation of squeeze flows, a suitable fluid model is needed.

2.4.3 Material Models of Fluids

As any modelling process, the simulation of squeeze flow using the PFGM also requires a material law, or in this case, a flow law. The simplest way to describe a fluid is to use the Newtonian flow law. It assumes that the fluids shear stress, τ, is proportional to the shear rate, $\dot{\gamma}$, as stated by Equation 2.8:

$$\tau = \eta \cdot \dot{\gamma} \tag{2.8}$$

whereby the constant of proportionality, η, is referred to the dynamic viscosity of the fluid. In a more general description of fluid behaviour the viscosity can be a function of the shear rate itself, however for the Newtonian-law it is a constant, as stated in Equation 2.9:

$$\eta\left(\dot{\gamma}\right) = \eta_0 \tag{2.9}$$

In addition, there are various non-Newtonian flow laws, which might be suitable to describe the behaviour of shear-thinning liquid adhesives, one of which is the Power-law also known as the Ostwald–de Waele relationship. Therein the shear stress of the fluid is given by Equation 2.10:

$$\tau = K \cdot \dot{\gamma}^n \tag{2.10}$$

where K is a flow consistency index in the unit of Pa $\cdot$ s$^{\mathrm{n}}$ and n is the dimensionless flow behaviour index. By equating Equation 2.8 and Equation 2.10 one obtains that the viscosity according to the Power-law can be described as Equation 2.11:

$$\eta\left(\dot{\gamma}\right) = K \cdot \dot{\gamma}^{n-1} \tag{2.11}$$

and it can be seen that it is a generalized form of the Newtonian-law, which is obtained for $n = 1$. However, for $n < 1$ the fluid behaves pseudoplastic (shear-thinning, meaning the viscosity decreases with increasing shear rates) and for $n > 1$ the fluid is dilatant (shear-thickening, meaning the viscosity increases with increasing shear rates).

Another flow law that is considered to describe shear-thinning behaviour of adhesives is the Yasuda-law [103], given by Equation 2.12:

$$\eta\left(\dot{\gamma}\right) = \eta_{\infty} + \left(\eta_0 - \eta_{\infty}\right) \cdot \left(1 + \left(\lambda\dot{\gamma}\right)^{\alpha}\right)^{\frac{n_{\text{Yas}}-1}{\alpha}} \tag{2.12}$$

which is a generalization of the *Carreau-law* [12], in which the exponent $\alpha = 2$. Furthermore, n describes the dimensionless power index, λ is a characteristic time in s, η_0 is the viscosity at zero shear rate in Pa · s and η_{∞} is the viscosity at infinite shear rate in Pa · s.

All of these considered flow laws were already implemented in the PFGM as described in much detail in [67]. The determination of the model parameters of the fluids used in this thesis will follow in subsection 4.2.1.

2.5 Topology Optimization

2.5.1 Solid Mechanics

Topology optimization is a design methodology that seeks to maximize the structural efficiency of a component or system by strategically allocating material only where it is structurally most essential. This approach aims to conserve material resources in areas with lower structural demands. Various criteria, including stress, strain, or a combination of them, i.e. energy, can be employed to identify regions where material can be minimized. The finite element method enables the rapid computation of these criteria, even for complex three-dimensional (3D) structures.

Topology optimization methods have undergone rapid development and improvement over the past three decades. The origin of today's established methods for topology optimization goes back to Xie and Steven who published *a simple Evolutionary procedure for Structural Optimization* (ESO) back in 1992 [100]. Their proposed methodology utilized the finite element method to gradually reduce a structure by rejecting a ratio (RR) of low stressed elements based on the von Mises stress criteria σ_{vM}. Elements e, which von Mises stress is less than the RR multiplied by the maximum von Mises stress of the structure ($\sigma_{\text{vM},e} < \text{RR} \cdot \sigma_{\text{vM,max}}$) are iteratively deleted until a steady state is reached. Every time a steady state is reached the RR is increased by an evolution rate (ER) and the iterative optimization procedure takes place until a global convergence criteria is satisfied, e.g. until all stresses are within 25 %.

This fairly simple approach resulted in structures which are surprisingly similar to solutions obtained by analytical optimization methods — such as the Michell type frame structures named after Michell [64] as illustrated by Figure 2.16. However, Xie and Steven didn't claim that their developed ESO method results in mathematically optimal solutions, but in the eyes of a structural engineer it was clear that the gained structures do perfectly

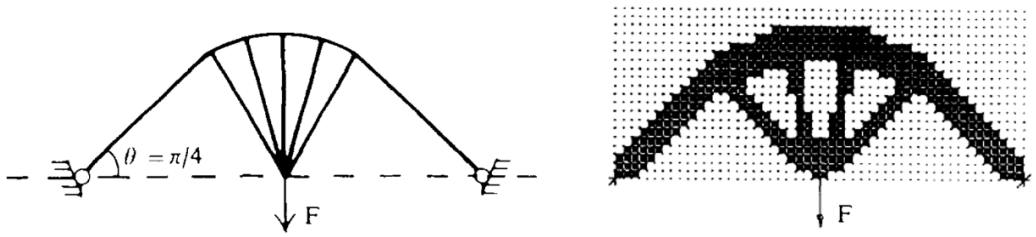

Figure 2.16: Optimization of a Michell type structure (high beam on two fixed bearings): Optimal solution obtained with analytical methods (left, [64]) and according to Evolutionary Structural Optimization with RR = 12.5 (right, [100]).

counteract the given loads and boundary conditions.

Further development by Querin et al. [75] let to the Additive Evolutionary Structural Optimization (AESO) method, which can be considered as a contrary or reverse method to the original ESO approach. As the name already indicates, this method starts with the smallest possible design domain, which connects all loads to the boundary conditions, and iteratively adds elements to the existing ones where the material utilization, e.g. a stress criterion, is very high. One main advantage of this method is the saving in computation time as the number of elements is much smaller during the first iterations of the evolutionary process compared to the original ESO method.

However, both ESO and AESO have one major shortcoming, once an element was either added to, or removed from the structure it couldn't be changed in the later optimization process, which according to Xia et al. [98] raised the question of whether optimal structures can be created at all with these methods or not.

Finally, the decisive development of the methodology was done by Querin et al. [74] in 1998 by combining ESO and AESO to a Bi-directional Evolutionary Structural Optimization (BESO) method — which can both, add elements in high-stressed areas and delete elements in low-stressed ones. The new BESO methodology dispelled the question of whether optimal structures can be created or not — in fact the topology can evolve arbitrarily throughout the entire optimization process. With the BESO method, any initial topology can be chosen (in between the maximum and minimum possible design configuration), whereby the number of iterations needed for convergence, and consequently the computation time, is reduced even further. The new method has also been successfully applied to 3D structures with multiple load cases by Young et al. [104], cf. Figure 2.17.

These early optimization methods usually considered the von Mises stress criteria as the driving optimization parameter. A performance indicator (PI) was introduced in [54, 76] to benchmark the efficiency of an optimized structure compared to an initial fully stressed de-

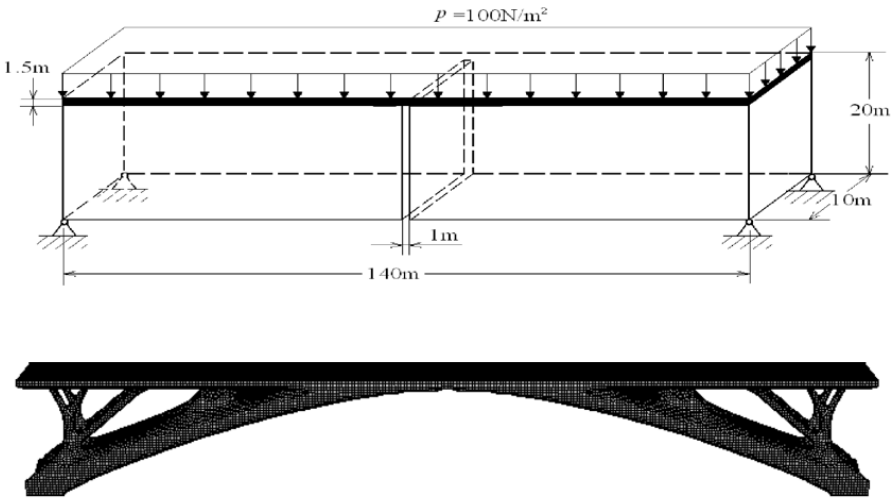

Figure 2.17: Structural optimization example for a bridge in 3D using the BESO methodology: design domain (top) and optimized geometry (bottom), taken from [38]. Note that the design domain does not allow material to be placed under the centre section to get a high level of clearance under the bridge.

sign and to check for convergence [74]. Later, the governing optimization parameter shifted to strain energy formulations and the optimization procedure was driven by minimizing the mean compliance of a structure to maximize its stiffness [15, 71]. For this purpose, *elemental sensitivity numbers* were introduced, which are defined by the change of compliance due to the removal or addition of elements: $\alpha_e = \frac{1}{2}\mathbf{u}_e^T \mathbf{K}_e \mathbf{u}_e$ [15].

Until this point, one major shortcoming of BESO methods was their mesh dependency — with finer meshing more voids (empty domains enclosed with material/elements) would be introduced during optimization. Consequently, so called *checkerboard* pattern could occur (with low-order bilinear, 2D, or trilinear, 3D, finite elements) because the sensitivity numbers could become C^0 discontinuous across element boundaries, according to Huang et al. [34]. To avoid the formation of smaller and smaller voids, a suppression algorithm was developed, which averages the sensitivity number of every element with those of the surrounding elements, within a certain radius, weighted anti-proportionally to their distances [53]. By additionally considering the iteration history, by averaging the weighted elemental sensitivity numbers with its value of the previous iteration step the BESO method became more stable and convergent during the optimization process.

Both of these techniques were implemented into a new *convergent and mesh-independent* BESO method [34, 38] by Huang and Xie. They were the first who formulated the topology optimization problem with mean compliance objective subject to a volume constraint

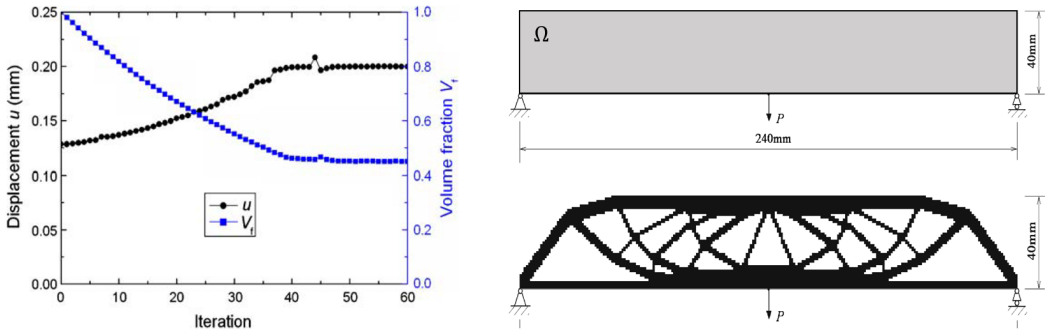

Figure 2.18: Structural topology optimization problem of a 2D single span beam: Evolution history of the volume fraction and maximum deflection (left), and design domain and optimized topology using BESO (right), taken from [37].

— the final step for a convergent topology optimization method; done by linking the evolution process, i.e. element removal and addition, to a volume ratio. The volume ratio leads to the target volume and consequently a target number of elements present in the next iteration, instead of simply removing an unlimited ratio of over- and underutilized elements. An example is given for a single span beam in Figure 2.18, the optimization goal was to minimize the volume and at a threshold of a maximum allowed deflection of $0.2\,\text{mm}$. This approach was implemented by sorting the elements according to their sensitivity numbers. By finding the threshold sensitivity number α_{th}, all elements which sensitivity numbers are equal or smaller than the threshold will be deleted: $\alpha_e \leq \alpha_{\text{th}}$; all elements which sensitivity numbers are larger than the threshold will be added: $\alpha_e > \alpha_{\text{th}}$. The threshold sensitivity number α_{th} corresponds to a design with the target volume of the next iteration – thus the optimization process is linked to a evolutionary volume ratio.

Further developments of optimization methods led to numerous solutions for specific problems such as algorithms for geometric non-linear structures [35], structures with non-linear material behaviour [97], fatigue loaded structures [42], multi-material structures [8, 23, 33], periodic structures [88], structures with buckling or dynamic problems [99, 101], or with constraints for additive manufacturing [41], etc., which are summarized in much detail in the following recent review articles: [36, 98, 108]. Such topology optimization techniques have been used to improve the design of several structures, for example: jacket support structures [89], transition piece [51] and rotor blades [11] for wind energy systems; steel reinforced aluminium casting [82]; reinforced concrete structures [3, 9, 58, 84], including bridges [5, 22, 56, 92] — to name a few examples.

Adhesive bonds can be optimized in different ways and with different objectives, e.g. considering BESO like topology optimization as done in [44]. However, most methods follow

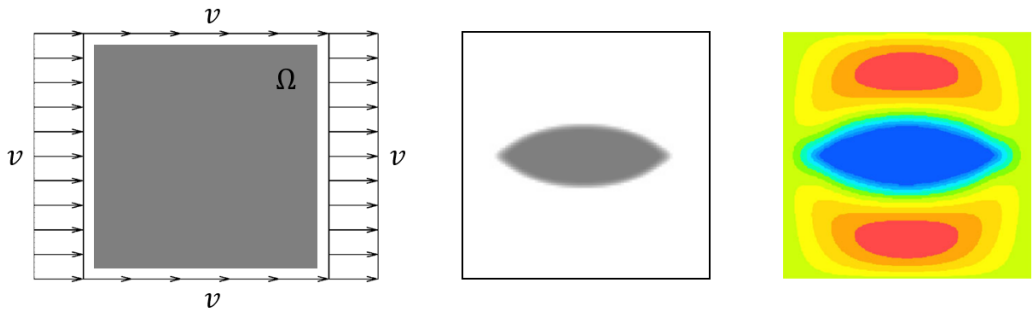

Figure 2.19: Optimised flow around an object with minimum drag: square design domain Ω and surrounding flow profile v (left), result of the optimized topology (middle), qualitative velocity magnitude (right). The problem is discretised with 120×120 elements, implies the no-slip condition, and the target volume of the object was 10% of Ω, taken & edited from [10, 25].

a similar approach, which attempts to reduce or redistribute the mechanical stresses in the adhesive layer in favour of the load capacity [91]. One possibility are the so called "mixed adhesive joints" [14, 17]. In these bonded joints, the adhesive layer consists of several adhesives that differ significantly in their stiffness, e.g. their Modulus of elasticity (MoE). A ductile (soft) adhesive is used at the locations where high stresses normally occur, thus locally reducing these stress peaks.

2.5.2 Fluid Mechanics

Topology optimization of fluids is a field of study that, similar to structural optimization problems, aims to optimize the shape and distribution of fluid (or its boundaries) within a given space to achieve a desired performance objective. This can be achieved by using numerical optimization algorithms to iteratively modify the geometry of the fluid domain or boundaries and solve the associated flow equations. One of the main challenges in topology optimization of fluids is the complexity of these governing equations, which typically involve Partial Differential Equations (PDEs) and require advanced numerical methods to solve. However, recent advancements in Computational Fluid Dynamics (CFD), such as the PFGM tool, have enabled researchers to address these increasingly complex problems.

A fundamental problem in flow optimisation is to find the shape of an object that has the least drag on the surrounding flow. This minimum drag optimization example was investigated e.g. in [10, 25] for Stokes flows (flows with low Reynolds number $\mathrm{Re} \ll 1$, i.e. were the inertial forces are small compared to the viscous forces). The optimization process started with a square design domain Ω that is surrounded by a flow profile v. They targeted

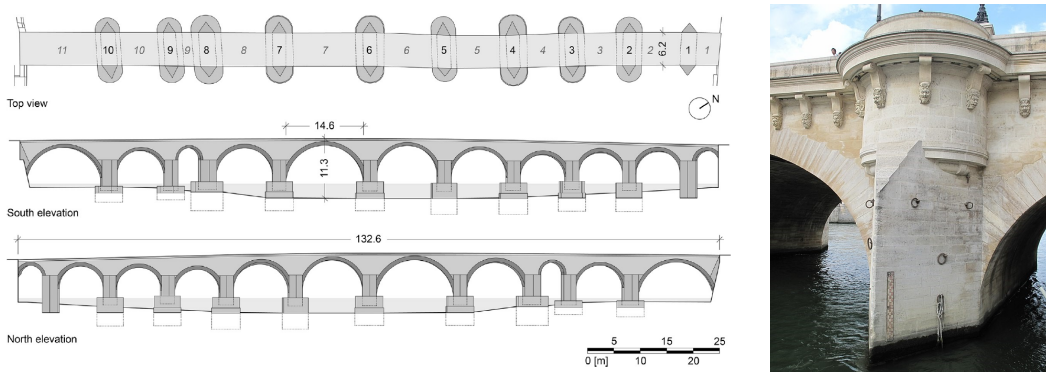

Figure 2.20: Bridge examples with pillar cross section for minimum drag: Azzone Visconti bridge (left, taken from [107]) and Pont Neuf bridge (right, from *Wikimedia Commons*).

different ratios between solid and fluid volume within Ω but found that the optimized shape always looked similar to a rugby ball, as shown in Figure 2.19. Another real world scenario where this optimized shape can be found quite often are the pillar cross sections of historic arch bridges that are made out of stone, e.g. the famous *Pont Neuf* bridge in Paris or the *Azzone Visconti* bridge in northern Italy, see Figure 2.20. These pillars were designed to *split* the water of the flowing river to minimize drag, and protect from ice floes, centuries before the development of flow optimization methods. Furthermore, cars are designed with air drag in mind to minimize fuel consumption [70].

Another branch of flow optimization deals with channel or pipe flows. Contrary to the previous example, in this case the fluid phase is surrounded by the solid phase which forms a boundary and thus directs the flow. Such flows can be optimized with several targets in mind, for example the minimization of pressure drop over the channel length [73]. The topology can also be optimized to dictate the flow velocity and direction at a certain point within the design domain. In the extreme case, Gersborg et al. and Olesen et al. [24, 72] have shown that the topology can be optimized to reverse the flow direction, as shown in Figure 2.21 at the cost of a pressure drop Δp.

Another area of interest related to flow problems is the optimization of heat flow. One example is the maximization of heat exchange or the design problem of a heat sink, which e.g. can enhance the performance of cooling devices. An ideal design involves an intricate channel that forms a delicate network with numerous branches, enabling efficient heat exchange between the fluid and solid domains, as depicted in Figure 2.22. The complexity of the channel indicates that a larger surface area between the fluid and solid domains is advantageous for heat exchange — just like known from theory.

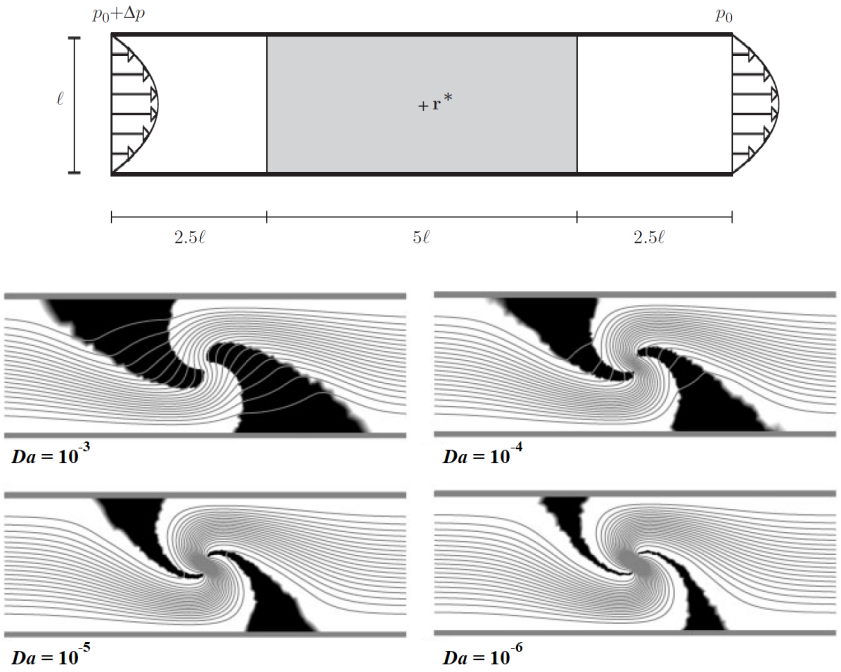

Figure 2.21: Optimization example that reverses the flow direction at point $r*$ for Stokes flow: Design domain and boundary conditions (top) and optimization structure with streamlines for different degrees of permeability (Darcy numbers, Da) of the porous boundary material (bottom), taken from [72].

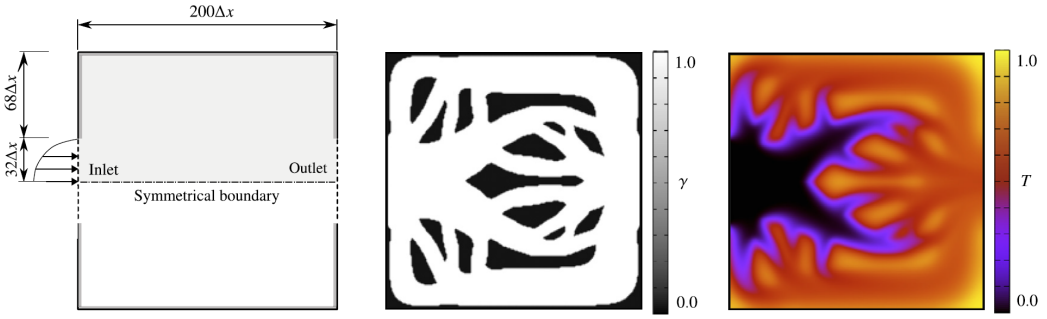

Figure 2.22: Heat exchange maximization problem: design domain and boundary conditions (left), optimized configuration (middle), normalized temperature distribution (right), taken from [102].

There are numerous fascinating domains that delve into the optimization of fluid flow, including the exciting realm of traffic optimization, cf. [94]. The field of topology optimization for fluids holds immense potential to revolutionize the design of fluid systems, paving the way for highly efficient and groundbreaking designs. Future research in this area is poised to unleash advanced optimization algorithms and embrace the integration of complex physics within the optimization framework.

It is worth noting that — to the best of the author's knowledge — the approach to apply optimization techniques to squeeze flow problems as proposed in this thesis is completely new and unique. This thesis aims to break new ground by combining innovative concept of topology optimization with the powerful and efficient PFGM tool. The goal is to optimize the application pattern that experience squeeze flow and thus modernize adhesive joining manufacturing processes.

3 Objectives

The main objective of this thesis is to develop and validate a simulation-based methodology which optimizes the adhesive application pattern's shape. The primary goal is to ensure that these optimized patterns seamlessly flow into the intended bond shape during the substrate joining process. In essence, when the target gap is reached, the adhesive should uniformly fill the entire bond geometry, minimizing any discrepancies between the target and achieved bonded surfaces. Additionally, these optimized patterns should effectively prevent any air entrapment during the squeezing phase. To achieve this overarching goal, several critical questions, which remain partially unresolved in the current state of the art, must be addressed in advance.

3.1 Open Questions and Preliminary Work

Of central importance is the validation of the selected simulation software, the Partially Filled Gap Model (PFGM). This software serves as the foundational tool for the development of a method to optimize the shape of adhesive application patterns. To validate the PFGM effectively, it is imperative to establish an adequate experimental setup and a rigorous analysis procedure. Both combined should have the capability to precisely measure all the relevant process parameters as a function of time to subsequently be compared with the PFGM simulation's calculations. Among the critical parameters are the force-displacement characteristics, the evolution of the fluid's shape, and the corresponding velocity fields. This validation process is essential to ensure the reliability and accuracy of the simulation model. Until now it is not clear, if:

> **Hypothesis #1:** Adhesive squeeze flow processes can be experimentally characterized by combining Particle Image Velocimetry and the Hele-Shaw approach.

as it has never been done before.

Despite the fact that the PFGM was particularly developed to simulate flows in narrow gaps, which is the reason why it is considered to be used in this thesis, it has never been

validated experimentally. However, this is very crucial and the statement that:

> **Hypothesis #2:** The Partially Filled Gap Model provides the accuracy that is needed for the optimization of adhesive application pattern.

is the second hypothesis that needs to be addressed.

Furthermore, it is common that the substrate surfaces are pre-treated in different ways before the adhesive is applied and squeezed in-between them. There are a variety of different methods, however all of them aim to improve the adhesion of the bonded joint by changing the surface roughness or energy. It is not clear which impact these modifications have on the squeeze flow processes, thus raising the question if:

> **Hypothesis #3:** The surface structures of the substrates which squeeze the adhesive can be neglected in the Partially Filled Gap Model simulation.

3.2 Scientific Goal and Main Objective

Once these questions are answered by the experimental validation in which the PFGM needs to prove sufficiently accurate, the main objective of the thesis — the optimization of adhesive application pattern — will be addressed:

> **Scientific goal:** The goal of this thesis is to develop an optimization methodology which finds adhesive application pattern that flow into the desired bond geometry during the joining process and thus *reduce adhesive spill-out and underfilling*.

To do so, an algorithm will be developed, which gradually modifies the shape of an application pattern, by penalizing overfilled domains of fluid in the initial pattern, as illustrated in Figure 3.1. The PFGM is implemented in the algorithm to gain the information about the squeeze flow process, that are needed to feed the criteria which modify the application pattern. After each modification a new squeeze flow calculation is performed by the PFGM and based on the new results the optimization cycle continues until a global convergence criterion is satisfied and the pattern is optimized.

Within one iteration cycle, the optimization algorithm needs to find the areas of fluid that, according to the transient vector fields calculated by the PFGM squeeze flow simulation,

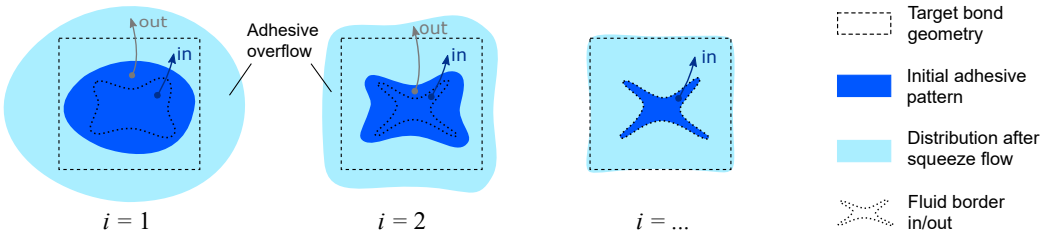

Figure 3.1: Schematic representation of the simplified methodology for optimizing adhesive application patterns.

have flown out of a pre-defined target bond shape, and then trace these areas back to their origin in the initial application pattern. Based on this information, the initial application pattern is modified, and a new iteration cycle begins, in which less overflow is expected, cf. Figure 3.1.

The iteration cycle will continue until the shape of the pattern has converged and flows into the desired bond shape within a certain tolerance. To reliably trace the fluid flow and locate overfilling, it is quite important that the PFGM simulation data feeding the algorithm is accurate in terms of velocity magnitude and direction — which is the reason why it will be experimentally validated in advance.

To ensure that the developed optimisation method can be applied in practice, the following three subgoals are pursued. First, it is important that the optimisation can be applied to a wide range of industrial problems, which is why:

> **Subgoal #1:** The algorithm is supposed to find an optimal application pattern that flows into *any desired adhesive layer* geometry and thickness.

Furthermore, numerical simulations often require a multitude of model and material parameters, which must be determined in advance with considerable effort. Therefore, in order to lower the threshold for applying the developed optimization method, it is aimed that:

> **Subgoal #2:** The algorithm should use a *minimal number of input parameters* to ensure a straightforward utilization in practical applications.

Last but not least, any optimization tool is useless if the generated result is not implementable in practice. In some cases, additional constraints for manufacturability are even programmed into the algorithms, cf. [23, 41], so that the ecological added value gained

by the optimisation is not negated by a possibly more expensive manufacturing process. Therefore, it is also aimed that:

Subgoal #3: The application patterns optimized by the algorithm should be *applicable and producible in reality* using common manufacturing methods.

3.3 Structure of this Thesis

Part I just introduced the reader into the scientific topic and gave a brief overview on the state of the art — beginning with experimental investigations on squeeze flow processes and Particle Image Velocimetry including multiple examples. Subsequently, numerical methods for the simulation of squeeze flow processes, including commercial CFD tools were shown and the specialized PFGM software was introduced. The state of the art was completed by presenting different approaches on topology optimization for structural and fluid applications, including multiple examples. Afterwards, the objectives and the scientific goal were defined.

Part II of this thesis addresses all the questions that need to be clarified before the optimization can be performed. It is first demonstrated how to measure adhesive squeeze flows accurately by combining PIV with the Hele-Shaw approach. Afterwards, this methodology will be applied to experimentally validate the PFGM to prove if it provides the accuracy that is needed for the optimization of adhesive application pattern. Last but not least, the influence of the surface structure on the squeeze flow process will be addressed to clarify if it has to be considered in the simulation process within the optimization algorithm. Then, some interim conclusions will be drawn wherein the three hypothesis defined in the objectives will be addressed.

Part III will focus on the main goal — the optimisation of application patterns — once the mentioned questions have been clarified. First, an optimization methodology is proposed according to which subsequently an optimization algorithm, that utilizes the PFGM simulation tool, will be developed. The algorithm should optimize adhesive application pattern with the goal of minimizing adhesive spill out and to avoid under filled domains in any bond. The choice of the optimization strategy is clarified, and the optimization capabilities are extensively demonstrated in several examples. Some of the examples will also be investigated experimentally and be compared to the simulation. At the same time, it is shown how to automatically apply these optimized patterns in a simple way.

Part IV will discuss the scientific impact and the technical benefit of the developed op-

timization methodology — beginning with a summary of the work followed by a discussion about the gained advantages, current limitations, and possible improvements, as well as the experimental verification of the optimization algorithm. Thereafter, conclusions are drawn and the scientific goal as well as the three subgoals defined in the objectives will be addressed. Furthermore, an outlook will be given at the end.

Part II

Experimental Validation of the Partially Filled Gap Model

4 Measuring Adhesive Squeeze Flows

This chapter presents an adapted methodology to measure adhesive squeeze flows to enable the validation of the PFGM. It is demonstrated how an existing HSC at Fraunhofer IFAM needs to be modified for the specific problem of this thesis. Therefore, the methodology of PIV is implemented to the HSC to enhance the measurements and allow for the validation of the simulated velocity fields by the PFGM. A model fluid is then selected, and its rheological behaviour is characterised to show that it can be used as a transparent dummy fluid throughout the thesis.

4.1 Adapting the Hele-Shaw Approach

The classical Hele-Shaw approach needs to be adapted for the investigation of adhesive squeeze flows, as the original HSC, cf. [80], consist of two plates which are stationary, and the fluid of interest was injected in-between them. However, in the case of squeeze flows — as the name already suggests — the flow is enforced by the movement of the plates.

Furthermore, it is crucial to carefully consider the calibration and stiffness of the HSC due to the significant squeezing forces caused by highly viscous liquids, such as most adhesives, which can potentially deform the experimental setup. Additionally, the successful implementation of PIV requires the coordination of key components, including the selection of a transparent dummy fluid, tracer particles, and the camera system with a suitable lighting source.

4.1.1 Experimental Setup

The test setup is specifically designed to replicate and observe adhesive flow during a joining process experimentally. In a nutshell, the fluid of interest is squeezed in-between two parallel surfaces and consequently propagates outwards in several directions while yielding an orthogonal force on the squeezing surfaces. To conduct this experimental investigation, a new cell was developed at Fraunhofer IFAM which is modified in this thesis. When combining it with a Universal Testing Machine (UTM, from *ZwickRoell* (RetroLine), 10 kN load cell), this apparatus can measure the forces (designated as F) that occur as a function of the

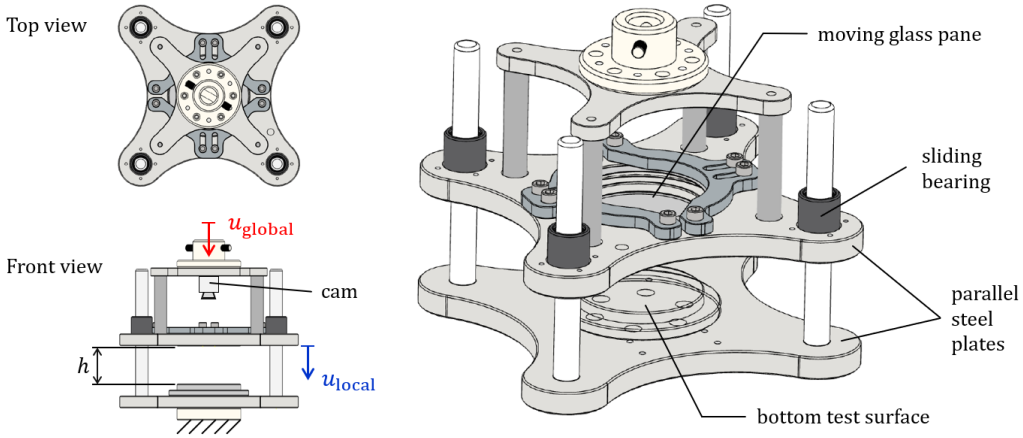

Figure 4.1: Experimental setup of the adapted closing Hele-Shaw cell.

gap height (referred to as h), that results from an initial gap height minus the displacement of the Universal Testing Machine (UTM): $h = h_0 - u$.

The revised HSC, developed during this thesis, is illustrated in Figure 4.1. It consists of two solid steel plates (15 mm thickness), which can be moved to each other via four sliding bearings. A glass pane (80 mm diameter) is arranged in the centre of the top steel plate, through which the fluid can be observed with a high-resolution camera. The camera, on which more details will follow in subsection 4.3.1, is directly centred above the moving glass pane. The bottom test surface is positioned and fixed on the second (bottom) steel plate. Optionally, when using two glass surfaces as substrates, the squeezed fluid can be illuminated from below with a light-unit, that holds three LED rings and thus improves the recording quality.

4.1.2 Calibrating the Cell

Before starting an experiment, the setup needs to be calibrated. Therefore, the force is zeroed while the HSC is open ($F := 0$ at $h > 0$). Then the glass panes are moved together until they touch each other, and a very low force of $F < 10\,\mathrm{N}$ is applied. In this closed but almost stress-free state, the displacement signals of both sensors are zeroed ($h := 0$). Then the cell is opened again to check if the local, and the global displacement measurements match.

4.1.3 Stiffness Correction

In order to measure the gap height and simultaneously control the squeeze velocity w in displacement, at which the gap h closes, the global displacement sensor of the UTM is used.

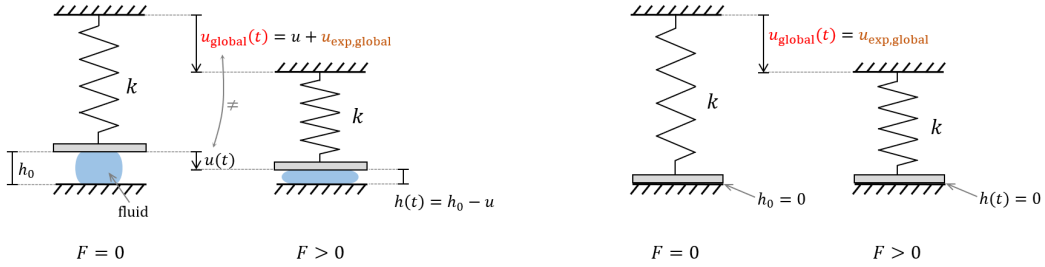

Figure 4.2: Idealized experimental setup as a spring model for the squeeze-flow scenario with fluid (left) and for the determination of the experimental setup deformation and stiffness without fluid (right). The linear spring considers the stiffness k of the whole experimental setup, including the deformation of the UTM and HSC under load. For the sake of clarity, only the global displacement is shown here.

However, this measured displacement (u_{global}) does not exactly represent the true displacement, u, at which the fluid is squeezed, because the experimental setup is not completely rigid, as illustrated in Figure 4.2 (left). In most cases the very small deformation of an experimental setup, u_{exp}, can be neglected, but here, in the case of squeeze flow, F increases highly non-linearly to h. This means the measurement of h needs to be very accurate.

Consequently, h is determined locally (in addition to the global measurement) with an additional, external displacement sensor (an incremental length gauge, Model MT 2571 from *Heidenhein* with 0.2 µm accuracy class) directly positioned between the steel plates of the HSC. Under load the whole experimental setup, especially the HSC deforms slightly. Thus, the local sensor should enable a more accurate measurement due to its close position to the glass panes. However, it turned out that even the measurement of the local sensor, which is perfectly fine in most cases, is not precise enough here, because of the mentioned high non-linearity, i.e. $F \sim 1/h^5$. To overcome this challenge and provide the accuracy needed, the global deformation (or stiffness) of the experimental setup, $u_{\text{exp,global}}$, was considered separately by subtracting it from the globally measured displacement — to obtain the true displacement: $u = u_{\text{global}} - u_{\text{exp,global}}$. Then the accurate gap height h can be calculated by subtracting the correct(ed) deformation u from the starting gap: $h = h_0 - u = h_0 - u_{\text{global}} + u_{\text{exp,global}}$.

To determine $u_{\text{exp,global}}$, the HSC was stressed in the closed state ($h_0 = 0$) and the displacement was measured simultaneously with the global sensor, as illustrated in Figure 4.2 (right), and local sensor. Although the cell is already completely closed, the global sensor detects a displacement of about 69.1 µm/kN, see Figure 4.3, which can only result from the deformation of the experimental setup, i.e. here $u_{\text{global}} = u_{\text{exp,global}}$. An identical correction of the gap height following the same procedure is also done for the local displacement

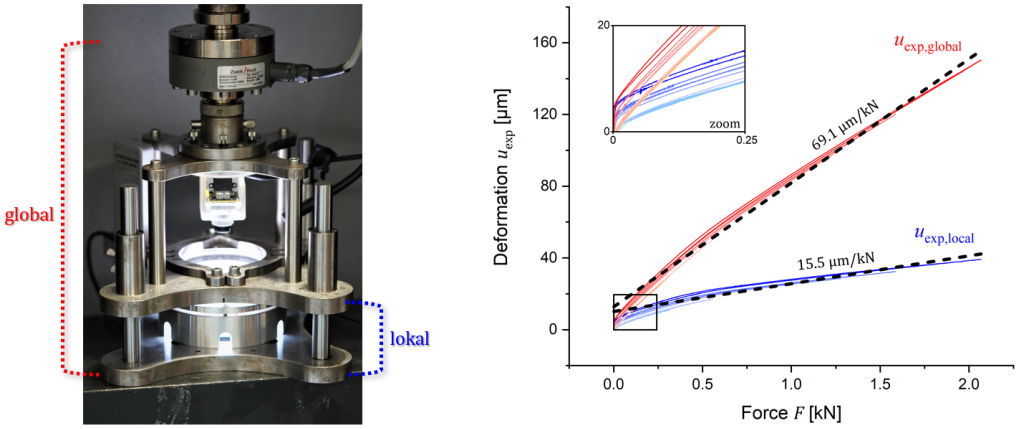

Figure 4.3: Stiffness determination of the Hele-Shaw cell: The cell mounted in the UTM with indications of the distance between which the deformation of both sensors is measured (left) and measured global and local deformation of the experimental setup while the HSC was in the closed state, i.e. $h_0 = 0$ (right).

sensor, which still detects about 15.5 µm/kN of local deformation in the *remaining* experimental setup, see Figure 4.3, however both corrections lead to the same result.

To clarify the need for stiffness correction, assume that some experiments will reach forces around 2 kN, resulting in 31 µm error in the deformation measurement by the local sensor. At this point the final gap of, let's assume, $h_{\text{fin}} = 300$ µm will be reached, so there is about 10 % error in gap height if the stiffness of the experimental setup is not taken into account. But then, to predict the forces at a certain gap height $h = h_0 - u$ which are highly nonlinear to h, in fact $F \sim 1/h^5$, so the error scales by an exponent of five. Consequently, the stiffness correction is crucial to later be able to compare the experimental results with the simulation.

4.1.4 Test Procedure

At the beginning of each experiment, a defined mass m of liquid adhesive (which properties will be described in more detail in subsection 4.2.1) is applied to the bottom test surface in the desired shape, e.g. in the form of a drop. The test surfaces were previously cleaned with isopropanol. The fluids mass is determined with a precision scale (from Kern, model PB400-3, reproducibility and readability 0.001 g) by means of differential weighing. Subsequently, the initial gap h_0 is approached. Beginning from h_0, a final gap of h_{fin} is approached at a constant squeeze velocity w which is controlled in displacement. During the experiment, F as well as u_{global} and u_{local} are measured as a function of time. In addition, the adhesive

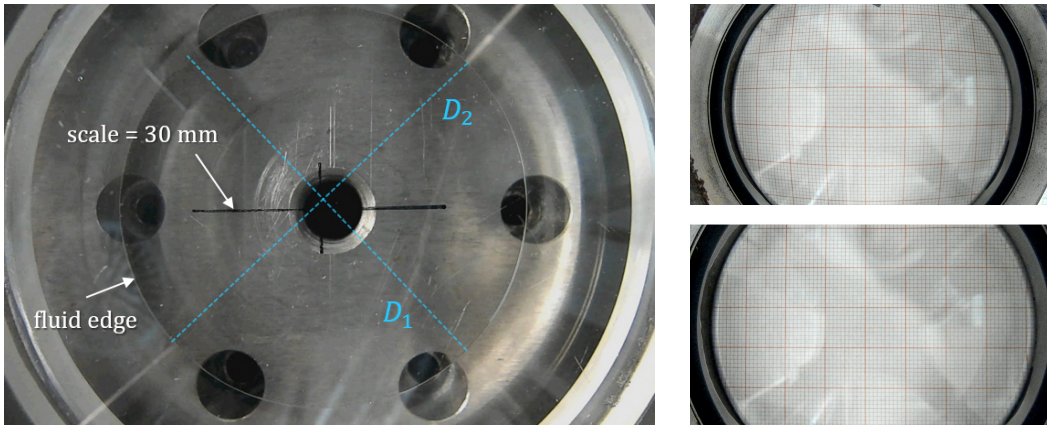

(a) Determination of fluid diameter (b) Correction of lens distortion

Figure 4.4: General procedure for fluid shape evaluation.

is filmed from above through the transparent glass pane with a high resolution camera to observe the spread of the fluid. All experiments are performed at room temperature.

4.1.5 Fluid Shape Evaluation

Additional parameters regarding the change of the fluid flow shape during squeeze can be analysed through the recorded video frames. With the help of reference points drawn on the glass panes or other objects of known size (i.e. a scale) the dimensions of the fluid shape can be evaluated at any desired time using the software *ImageJ*. Subsequently, the determined shape(s) can be compared to the simulation results of the PFGM in terms of wetted area or other fluid pattern dimensions such as width, length, or diameter (depending on the actual shape).

For example, the procedure for the determination of fluid diameter is shown in Figure 4.4 (a), where the fluid diameter was determined in terms of a mean diameter, $D = {}^1/_2(D_1 + D_2)$, through a 30 mm long scale that is drawn on the glass pane. The videos are synchronized to the measured force-displacement signal and the distortion of the camera is corrected by a suitable filter in advance, as shown in Figure 4.4 (b).

4.2 Adhesive Selection and Application Technique

For manufacturing processes that involve compression, it's advantageous for adhesives to possess high viscosity and exhibit thixotropic (shear thinning) behaviour. These properties prevent the adhesive from flowing due to gravity, allowing it to maintain its intended shape

until it is compressed between substrates.

To study the squeeze flow process using PIV comprehensively and reliably, the fluid must meet additional criteria. Most importantly, it needs to be transparent to track the flow using tracer particles. It's also beneficial if the adhesive doesn't cure during experiments conducted at room temperature, ensuring consistent rheological properties, and enhancing repeatability. This further eliminates the limitation imposed by the adhesive's pot life, i.e. the time constraints associated with cleaning the cell's glass surfaces after each test.

Since most adhesives aren't transparent and practical requirements rule out real adhesives, a substitute fluid was chosen for this study. A transparent, non-curing silicone oil, known as *Elbesil B 2.000.000* (referred to as fluid, oil, or silicone oil), was carefully selected as a suitable alternative because its rheological behaviour closely resembles that of real adhesives, i.e. highly viscous, thixotropic and shear-thinning. For the sake of brevity and clarity, this thesis primarily focuses on this selected fluid, with exceptions explicitly mentioned when other fluids are used.

4.2.1 Fluid Properties

The selected silicone oil *Elbesil B 2.000.000* is manufactured by *QUAX GmbH* in Germany. The density of the fluid was measured at $25\,^{\circ}\mathrm{C}$ to $\rho = 0.98\,\mathrm{g/cm^3}$. Three fluid viscosity laws are considered, Newtonian-, Power- and Yasuda-law, cf. subsection 2.4.3, and plausible parameters are chosen for these laws in conjunction with experimental studies [67] where this highly viscous fluid was selected as a model fluid and rheologically characterized as shown in Figure 4.5.

The viscosity of the used fluid at low shear rates is $\eta_0 = 1744\,\mathrm{Pa \cdot s}$, which serves the Newtonian flow law. However, in the rheological experiments, the fluid behaved shear-thinning which can be better described by the Power-law using $K = 1170\,\mathrm{Pa \cdot s^n}$ and $n = 0.864$ or by the Yasuda-law where $\eta_\infty = 0.000957\,\mathrm{Pa \cdot s}$, $\alpha = 0.775$, $n_{\mathrm{Yas}} = 0.322$, and $\lambda = 0.094\,\mathrm{s}$. This behaviour, as well as the range of viscosities, is quite comparable to actual highly viscous adhesives whose viscosity is approximately in the range of $1{,}000\,\mathrm{Pa \cdot s}$ to $10{,}000\,\mathrm{Pa \cdot s}$, thus it is a good choice for substitution. Further details about the determination of the unfilled rheological parameters of the fluid used can be found in [67].

4.2.2 Automated Application Process

The application pattern investigated in this thesis are applied using a dispenser (i.e. *Ultimus* from *Nordsond EFD*) that is linked to a xyz-Table (a aluminium flat bad/table unit, commonly used for CNC applications, $1350 \times 750\,\mathrm{mm}$ in size from the company *Isel*), so that

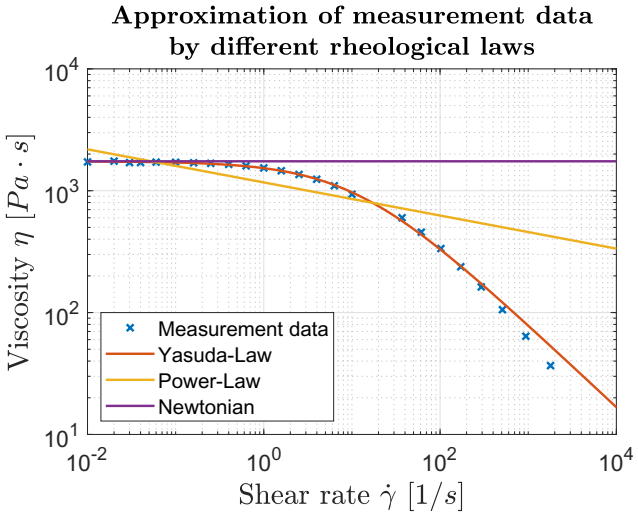

Figure 4.5: Rheological measurements and approximation with flow laws of the used silicone oil *Elbesil B 2.000.000*, taken from [67].

the desired application path and pressure for each pattern can be repeated very accurately. After some testing, an application pressure of $p = 1.85$ bar with an application head velocity of $v = 3.0\,\mathrm{mm/s}$ was found to be optimal for the considered silicone oil. The amount of adhesive applied is a result of the application pressure (which was constant) and application time (which was not constant due to the different application path length for different pattern). That said, while the application was controlled it didn't result in the same mass for all investigated patterns. The fluid is directly applied to a previously cleaned glass pane which fits into the HSC.

4.3 Implementation of Particle Image Velocimetry

The goal of the implementation of PIV to the HSC is to experimentally determine the velocity fields of the fluid during squeeze flow to later compare them with the calculated velocity fields of the PFGM simulations for different application pattern.

4.3.1 Setup and Analysis Procedure

The setup for PIV consists of one camera (See3CAM CU55 from *e-con Systems*) that is mounted within the HSC which films the fluid during squeeze flow looking from above. The camera has 5MP, a 1/2.5" image sensor with a resolution of 1920×1080 px and a framerate of 15 fps (66.66 ms frame-time). The recordings were analysed with the well documented and freely available software tool *PIVLab* [86, 87] based on *Matlab*. In detail a FFT

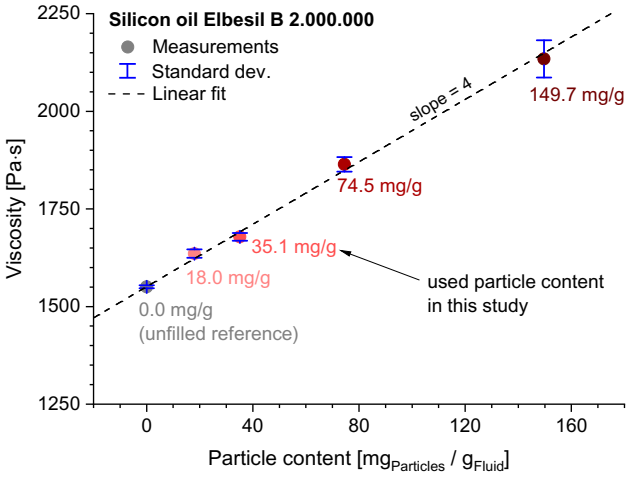

Figure 4.6: Viscosity in dependence of the tracer particle content of the used silicon oil. Measured with a rotational rheometer from TA Instruments Inc. (Discovery HR-2, plate-plate configuration, diameter $\varnothing = 25\,\mathrm{mm}$, gap height $h = 0.5\,\mathrm{mm}$, shear rate $\dot{\gamma} = 1.0\,\mathrm{s}^{-1}$) at an ambient temperature of $25\,^{\circ}\mathrm{C}$.

(Fast Fourier Transform) window deformation based multipass PIV algorithm with up to four passes beginning with an interrogation area of 128×128 px, followed by 64×64 px, and continued with 32×32 px and with 16×16 px if needed, applying extreme correlation robustness, was used to perform the PIV analysis.

The length was calibrated by putting an object of known size (functioning as a scale, $15.1\,\mathrm{mm}$ in length and $1.0\,\mathrm{mm}$ in thickness) in-between the glass panes where the fluid would normally be. A calibration image was taken and loaded into the PIV-software to determine the relationship between real length and number of pixels in the image. It was found that $1.0\,\mathrm{mm}$ in the plane of interest corresponds to 21 pixels in the image, and the tracer particles were mapped by three or more pixels which is ideal, cf. [87]. In addition, the PIV analysis was completed by choosing plausible velocity limits and interpolating missing velocity vectors, even the interpolation was barely needed.

4.3.2 Tracer Particles

Flake shaped tracer particles made from rayon fibres (manufactured by *Jofrika Cosmetics GmbH*, normally used as *glitter* make-up) and approx. $10 - 100\,\mu\mathrm{m}$ in size are used. They were mixed into the fluid at a proportion of $35.1\,\mathrm{mg}$ of particles per $1.0\,\mathrm{g}$ of fluid. The influence of the particles on the fluid's viscosity was investigated with a rotational rheometer. Therefore, a wide range of different particle contents (including the used particle content of $35.1\,\mathrm{mg/g}$ in this study) was investigated in addition to the unfilled fluid. It was found that

the fluid's viscosity increases approximately linear by adding tracer particles, as shown in Figure 4.6. The unfilled fluid viscosity ($\eta = 1551$ Pa · s) was thus increased by 8.2 % for the fluid-particle-mix ($\eta = 1678$ Pa · s) used in this study. This should be kept in mind since higher viscosity leads to increased forces during squeeze flow.

Furthermore, tests were performed to investigate the sedimentation rate of the particles. Hence, fluid-particle mixture was filled in a transparent cup which was observed over multiple weeks. The sedimentation rate was quantified by the velocity at which the particles sank. These pre-tests showed that the sedimentation rate of the particles is less than 1.0 mm/week, thus negligible for the comparatively short PIV experiments.

5 Identifying the Relevant Process Parameters with the Hele-Shaw Cell

Now that the experimental setup has been introduced, this chapter aims to apply the adapted cell and validate the PFGM in terms of fundamental quantities of the squeeze process. Specifically, it focuses on the behaviour of force, displacement, and the spread of the fluid (in terms of diameter evolution) during squeeze flow. To achieve this, a fundamental series of experiments is conducted.

5.1 Series of Experiments

The primary objective of this chapter is to investigate the impact of squeeze velocity (referred to as w, indicating the rate at which the gap closes) and adhesive mass (designated as m) on the resulting forces and the diameter of the squeezed fluid. Three distinct experimental series, designated as A, B, and C, were conducted to address these objectives.

For this investigation, four different squeeze velocities and three varied adhesive masses were taken into consideration, as detailed in Table 5.1. The chosen fluid mass values were deliberately selected to set the theoretical initial diameters within the range of $14\,\text{mm}$ and $18\,\text{mm}$. To accommodate the three different adhesive masses, the initial gap was adjusted accordingly for each series, ensuring that contact between the adhesive and the glass panes could be achieved at the outset of each test. Each individual test was repeated five times, resulting in a total of 60 individual runs (3 masses $\times$ 4 squeeze velocities $\times$ 5 repetitions).

5.2 Force during Squeeze Flow

In each particular experiment, the force evolution in the squeeze flow experiment is a key focus. Starting from the initial gap h_0, the UTM accelerates to the target squeeze velocity w, which remains as constant as possible thereafter. Notably, there is a discernible exponential rise in force, particularly evident from the 30 second mark onward. While slight variations in w occur due to continuous control, this is depicted in Figure 5.1 (top). Interestingly,

Table 5.1: Series of experiments and parameters, 5 repetitions per experiment.

Parameter			Series A	Series B	Series C
mass	m	[g]	0.679	0.302	0.873
initial gap	h_0	[mm]	3.5	2.0	3.5
target gap	h_{fin}	[mm]	0.3	0.3	0.3
squeeze velocity	w	[mm/s]	0.01	0.01	0.01
			0.10	0.10	0.10
			0.20	0.20	0.20
			1.00	1.00	1.00

no significant force is generated in the initial 20 seconds, despite the glass panes having already compressed the adhesive by nearly two-thirds of the required distance, as illustrated in Figure 5.1 (bottom).

The deformation of the experimental setup u_{exp} is directly proportional to the force F. With the increasing force and the corresponding deformation, the squeeze velocity gradually decreases from $0.10\,\text{mm/s}$ to approximately $0.07\,\text{mm/s}$ shortly before reaching the target gap. At around 33 seconds, the squeezing phase finishes; both force and u_{exp} reach their respective peaks for this run and the UTM then decelerates to $w = 0\,\text{mm/s}$. Following this, the accumulated deformation within the experimental setup reduces at a notably slow pace. This leads to an extended deceleration process compared to an ideal rigid setup. Additionally, the diameter continues to marginally increase, and the force decreases in tandem with u_{exp}. Even though u_{exp} is minimal, the final gap of $300\,\mu\text{m}$ is only achieved once the system reaches a state of mechanical relaxation.

The measured forces (coloured lines) and the simulation results of the PFGM (performed in [46] according to subsection 2.4.2) are shown in Figure 5.2. In all squeeze-flow experiments, the force increases exponentially, independently of squeeze velocity or fluid mass, as shown in Figure 5.2 (a–d). However, the squeeze velocity has the greatest impact on the associated force. At higher squeeze velocities, the force already increases significantly at relatively large gaps (e.g. Series A with $1.00\,\text{mm/s}$ results in 430 N at 0.75 mm gap), while lower squeeze velocities only lead to comparable forces at smaller gap heights (e.g. 0.10 mm/s results in about the same force of 430 N at $h = 0.53$ mm). Obviously, the rate at which the force increases is also dependent on the adhesive mass used. The larger the initial adhesive drop, the faster the force increases in relation to the remaining gap height, as shown in Figure 5.2 (d). All experiments were highly reproducible, as shown by the five overlaying curves of every sub-series, as well as the low standard deviation ($< 3\%$) of the maximum forces through all experiments.

For the simulations, the solid grey lines represent the results for the Power-law fluid model

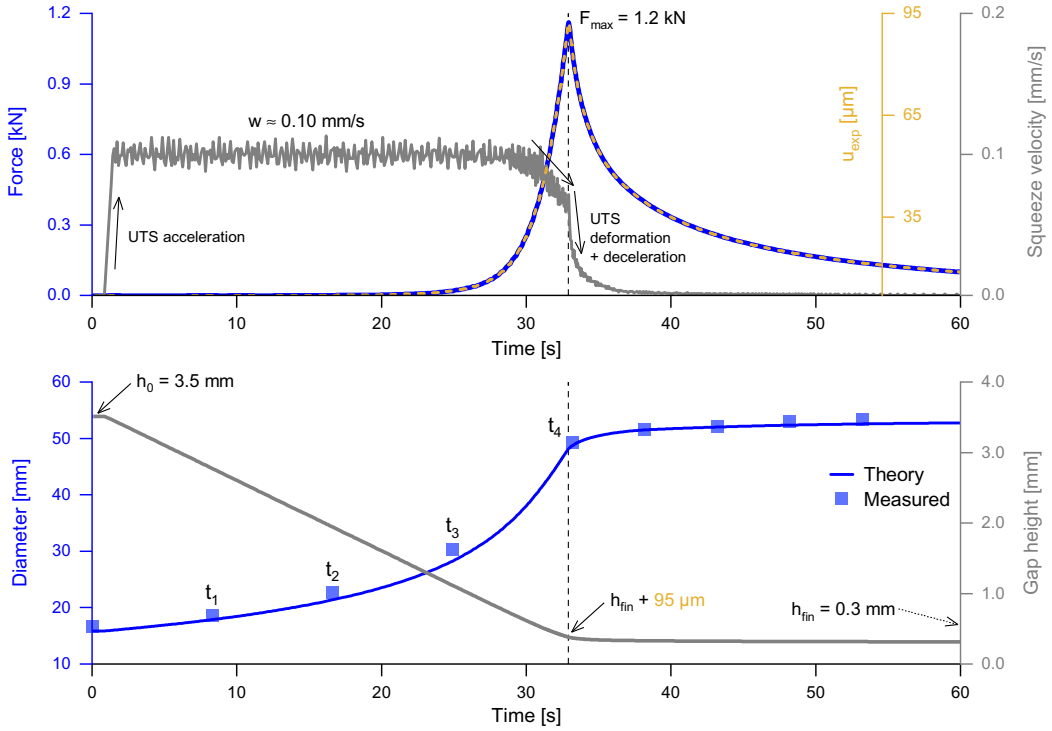

Figure 5.1: Development of squeeze force (top) compared with the fluid diameter (bottom) as function of time for a circular fluid drop with a mass of $m = 0.679\,\mathrm{g}$ and viscosity of $\eta \approx 1700\,\mathrm{Pa \cdot s}$ that is squeezed in-between two glass panes from an initial gap of $h_0 = 3.5\,\mathrm{mm}$ to a final gap of $h_{\mathrm{fin}} = 0.3\,\mathrm{mm}$ with a squeeze velocity of $w = 0.10\,\mathrm{mm/s}$.

and the black dashed line for the Yasuda model. It can be seen that the simulation reproduces the experiment very well if the Yasuda material model is used. If the Power-law is used for the simulation, the deviations increase with higher squeeze velocity and at high forces. This is a consequence of the different fluid models. At low shear rates, the viscosity is similar for Power-law and Yasuda. There, both material laws represent the used adhesive well. With increasing shear rates, the viscosity of the adhesive decreases non-linearly, which is better represented by the Yasuda model than by the Power-law. The Power-law overestimates the fluid viscosity. This leads to a larger force for Power-law simulations at higher flow velocities, which can be seen especially at $w = 1.0$ mm/s. Consequently, the Yasuda model is to be preferred for higher shear rates. The (slight) extra numerical effort using the Yasuda model is thus worthwhile, as these deviations to the measurements are very small considering the complexity of the fluid behaviour.

The deviations between experiment and Yasuda simulation are small. In the range be-

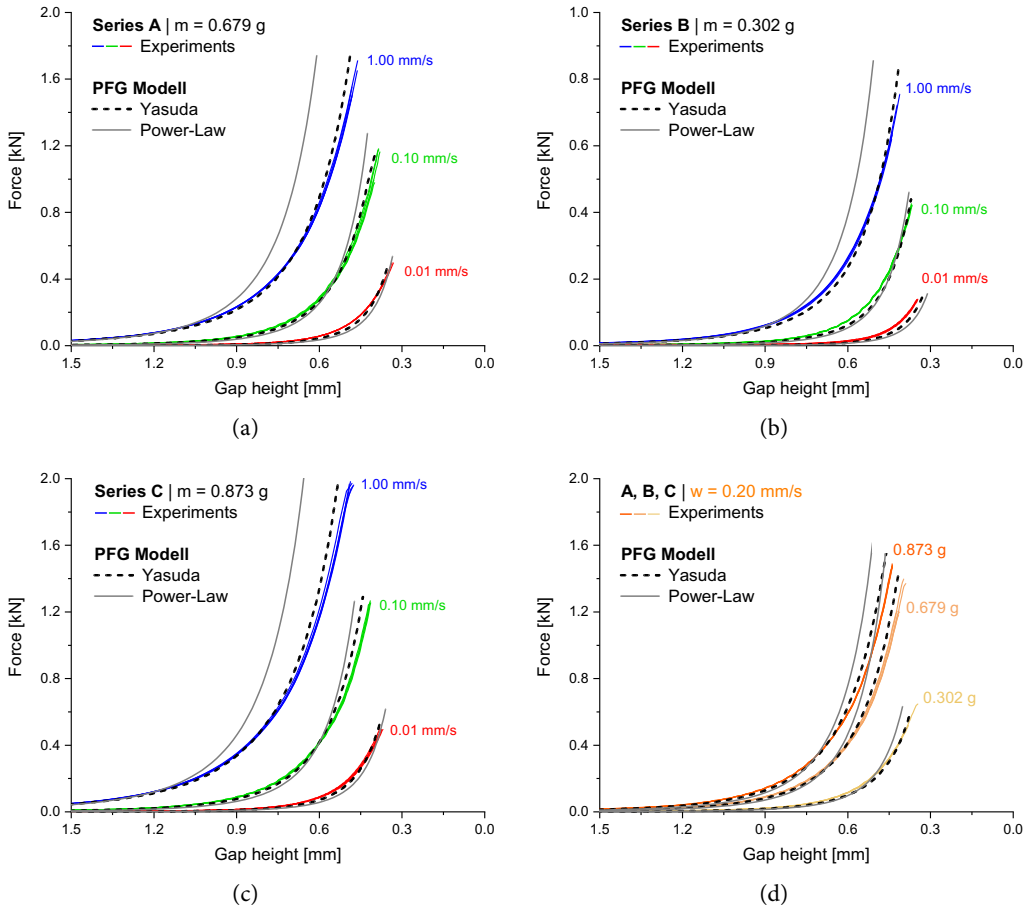

Figure 5.2: Measured force as a function of gap height compared to PFGM, for different squeeze velocities (a–c) and for different fluid masses (d). Simulation data taken from [46].

tween 400 N and 500 N, the force is predicted with very high accuracy. Below 400 N the simulation slightly underestimates the experimental values, above 500 N it overestimates them. At the point of maximum deviation (series C: 1.00 mm/s, at $F = 1874$ N), there is a difference in force of 18.9% for the same height and a difference in height of 8% for the same force. One possible reason for these deviations could be due to model assumptions, such as no-slip boundary conditions. Another reason is the uncertainty of the fluid flow model. The viscometers might not ideally represent the actual fluid shear in the experiment and the parameters of the Yasuda model are only a best fit of the viscosity measurements. Consideration of further effects in the PFGM or the inclusion of further rheological phenomena would possibly lead to smaller deviations, at the cost of experimental and numerical effort.

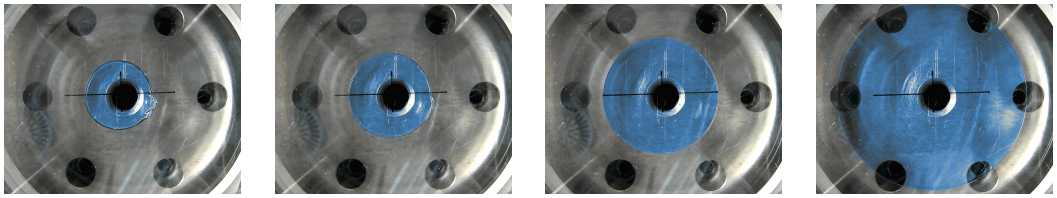

(a) $t_1 = 8.3\,\mathrm{s}$ (b) $t_2 = 16.6\,\mathrm{s}$ (c) $t_3 = 24.9\,\mathrm{s}$ (d) $t_4 = 33.2\,\mathrm{s}$

Figure 5.3: Development of the fluid shape and diameter at four successive time steps during squeeze flow (fluid dyed blue for better visibility).

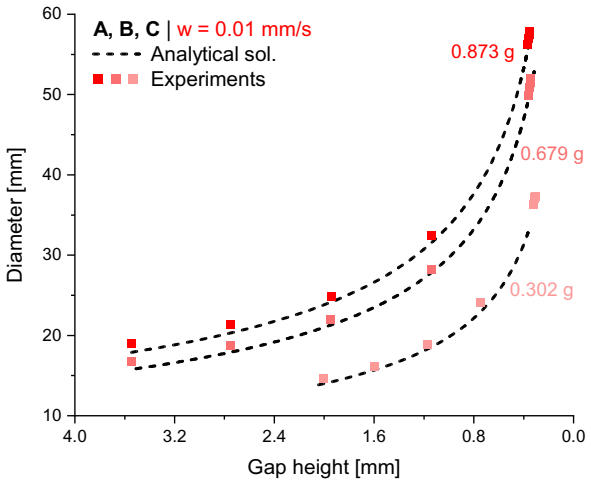

Figure 5.4: Evolution of diameter versus gap height during squeeze flow for different fluid masses.

The great strength of the PFGM is the relatively short computation time, which is essential for model extensions as planned in this thesis, and the use in practical applications.

5.3 Evolution of Adhesive Spread

The highly viscous fluid always spreads out circular in all series. Accordingly, the flow process can be quantified by the development of the diameter as a function of time or gap height. Unlike the force and the displacement, the diameter cannot directly be measured by the UTM. It is determined indirectly by the video recordings as described in subsection 4.1.5.

As the gap h becomes smaller, the diameter of the adhesive drop increases continuously from the first seconds of the experiment, as illustrated in Figure 5.3. The development of the diameter matches to the theory, see Figure 5.4, which simply calculates the diameter in relation to gap height by assuming a perfectly incompressible fluid and cylindrical flow

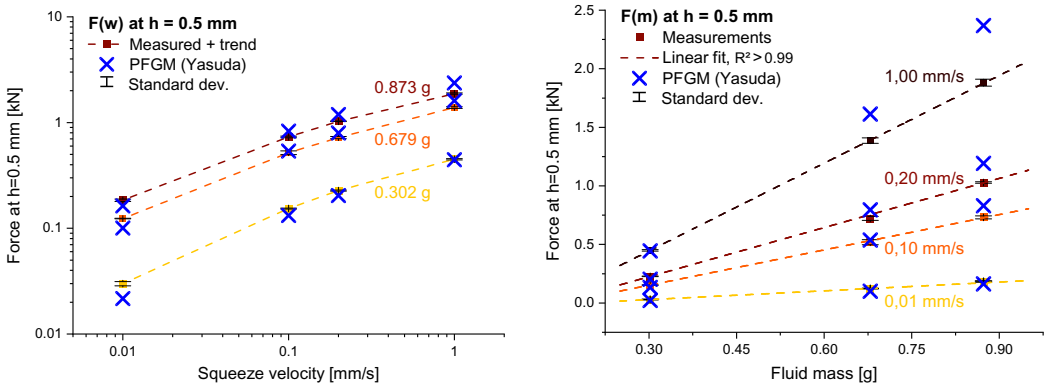

Figure 5.5: Squeezing force at a gap height of $h = 0.50\,\text{mm}$ in relation to the squeeze velocity (left) and fluid mass (right). The data points show the average values out of five measurements, i.e. repetitions. Simulation data taken from [46].

geometry, i.e. constant volume throughout the experiment. Thus, the diameter can be calculated as follows: $D = \sqrt{4V/(\pi h)}$.

5.4 Influence of Squeeze Velocity and Fluid Mass

The Influence of squeeze velocity and fluid mass on the force at a gap of $h = 0.5\,\text{mm}$ for different fluid masses (m) and squeeze velocities (w) is shown in Figure 5.5. For fluids described by the Power-law, including Newtonian fluids as a special case (where the flow index $n = 1$), it has been established that both pressure and normal force are proportional to w^n. Consequently, in a logarithmic plot such as in Figure 5.5 (left), a Power-law fluid is expected to manifest as a straight line with a slope n. However, a slight deviation in the slope of the curve suggests that the Power-law may not be the most appropriate for modelling the overall fluid behaviour with respect to squeeze velocity. The curves trajectory indicates that, up to a certain limit, the Power-law index (n) decreases with increasing squeeze velocity, signifying an amplified shear thinning effect at higher squeeze velocities. This behaviour aligns with the Yasuda-law until a finite intrinsic velocity is reached.

The force at $h = 0.5\,\text{mm}$ is graphed as a function of fluid mass in Figure 5.5 (right). The force exhibits a linear correlation with adhesive mass: $F \sim m$. The plots small error bars underscore the experiments exceptional repeatability, indicating low standard deviations. Additionally, the simulated forces by the PFGM, demonstrate a high level of agreement with the experimentally measured values, except for two measurements with $m = 0.679\,\text{g}$ and $m = 0.873\,\text{g}$ at $w = 1.00\,\text{mm/s}$, the force was overestimated by 16% and 26%.

6 Investigating Adhesive Squeeze Flow with Particle Image Velocimetry

The flow *velocity* and *direction* are crucial magnitudes for the optimization of adhesive application pattern. Deviations in the PFGM simulation of velocity magnitude and direction can prevent the correct tracing of the fluid, as illustrated by Figure 6.1. Since the optimization strategy of the algorithm, proposed in chapter 9, is based on the tracing of the fluid flow, the input values calculated by the PFGM need to be sufficiently accurate to generate plausible results. That said, this chapter is dedicated to check if the PFGM provides the accuracy that is needed for the chosen optimization strategy. To do so, the numerical model will be experimentally validated using Particle Image Velocimetry.

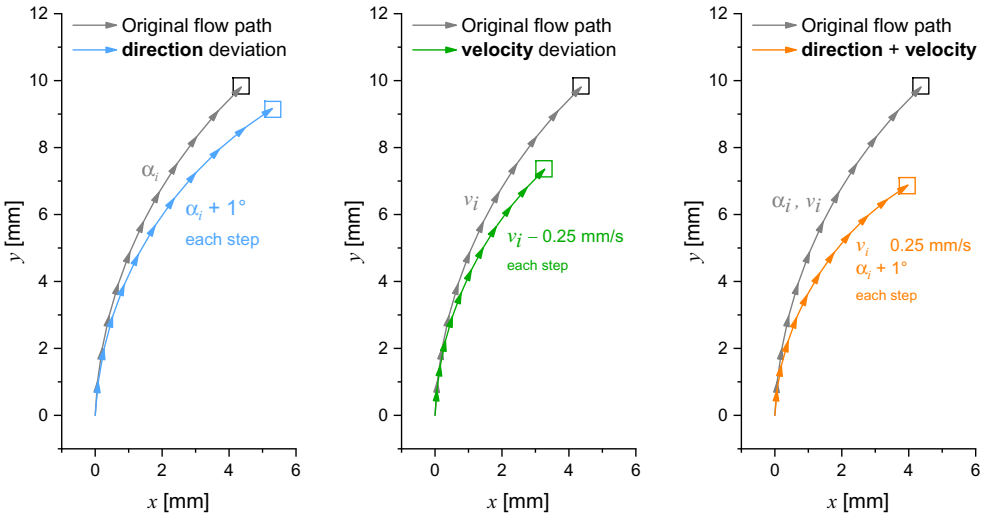

Figure 6.1: Illustration of fluid tracing errors due to deviation in flow direction (left, blue), velocity magnitude (middle, green) and both combined (right, orange) compared to a *correct* flow path (grey). The original pathline of the flow was chosen and generated so that each vector has a velocity magnitude of $v_i = 1\,\mathrm{mm/s}$ and is inclined in direction by $4°$ to the previous vector while each time step i lasts $\Delta t = 1\,\mathrm{s}$.

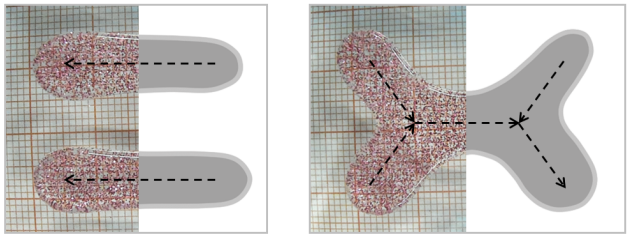

Figure 6.2: Investigated adhesive application pattern: II-pattern (0.69 g, left), X-pattern (0.94 g, right). In each case, the left side shows the real fluid-particle mix, the right side shows the simulation geometry input, the dashed arrows show the application path of the dispenser that is linked to the xyz-Table.

6.1 Validation Strategy

A transparent adhesive-like fluid with high viscosity was used for the validation, to which tracing particles were admixed, as described in subsection 4.3.2. Different adhesive application pattern will be investigated, that include different flow phenomena and meeting flow fronts. A series of squeeze flow experiments will be performed with the HSC and analysed using PIV to characterize the flow characteristics, according to the methodology described in section 4.3. The experiments are then compared to the simulation results of the PFGM which were performed in [46]. Special attention is given to the velocity magnitude and flow direction, both of which consequently lead to the development of the fluid-flow geometry.

6.1.1 Application Pattern

Two different application patterns are selected to be investigated. The first one consists of two parallel adhesive beads, subsequently referred to as II-pattern, see Fig. 6.2 (left). This pattern was selected, because it is expected that both flow fronts may meet and merge at some point during the squeeze process. The second pattern is shaped like a dog-bone or a stretched "X", subsequently referred to as X-pattern, see Fig. 6.2 (right). This pattern represents a first guess of an optimized shape which should flow into a nearly rectangular area during the joining process and thus minimize the spillage and waste of adhesive for rectangular shaped bonds.

6.1.2 Experimental Procedure

At the beginning of each experiment, the corresponding adhesive pattern is automatically applied on the previously cleaned glass surface (which was taken from the HSC) using a dispenser and xyz-Table, as described in subsection 4.2.2. Cleaning of the glass surfaces

was performed using isopropanol and lint-free wipes, with a minimum flash-off time of 10 minutes. Next the applied fluid-particle masses were measured by means of differential weighting and the glass surface with the applied fluid was positioned again in the HSC.

Then, starting from an initial gap of $h_0 = 3.5\,\text{mm}$, the fluid pattern is squeezed with a velocity of $w = 0.10\,\text{mm/s}$ until a final gap of $h_{\text{fin}} = 0.3\,\text{mm}$ is reached. Each experiment is repeated three times, however only one specific run per pattern was analysed using PIV. The time needed for each experiment, starting with the fluid application followed with differential weighting, recording data, and ending after the squeeze process is finished, is about 10 minutes.

Subsequently, the characteristics of the fluid squeeze flow are presented with focus on velocity and direction. Five characteristic points in time, t_1 to t_5, are considered per application pattern for which the experimental and numerical results are shown side by side — in particular

- the experimental fluid distribution,
- the PIV and PFGM simulated velocities along a path,
- the PIV velocity vector field and
- the PFGM simulated velocity vector field.

The video sequences of these results are linked in the corresponding figure captions. They can also be accessed by clicking on this link or by scanning the QR-Code in the Appendix.

6.2 Shape and Flow Behaviour

Before delving into the detailed results, it's important to provide some background on the data collection process. Each experiment was conducted three times, yielding highly consistent results. From these runs, a specific instance for each pattern was chosen for in-depth analysis.

To assess the magnitude of the velocity, paths are defined that run vertically through the frames. Both, experimental data (depicted with red steady-lines) and numerical data (shown in blue stepped-lines) were synchronized by aligning them using a reference point, typically the leading edge of the flow. It's worth noting that the frames were not distorted in any way during this process. The time difference between the experimentally recorded frames and the corresponding simulated time steps is within a margin of ± 0.1 s. The shaded grey area in the path plots indicates regions where the fluid is present, as determined by the experiments. These are the zones where non-zero fluid velocity should be observed. Each frame was quantitatively evaluated using a scale (introduced in subsection 4.1.5) and the software *ImageJ*.

6.2.1 II-Pattern

At the beginning of the squeeze process, at t_1, both adhesive beads are parallel to each other and are separated by an air corridor, as shown in Figure 6.3. At this time, a linear flow-profile occurs across each bead, so both, the upper and lower flow-fronts, move outwards the beads centre lines, with a peak velocity of approx. $v = \pm 0.35\,\mathrm{mm/s}$ at the fluid-edges. At t_2 the corridor of air became narrower and at t_3 the flow-fronts meet, slightly on the left side, which is due to imperfections during application of the II-pattern. However, in the centre (where the path runs through) there is still a slight air corridor left which is why one can still see two linear flow profiles at t_3 in the plot of the path. Until here the correspondence between experiment (PIV) and simulation (PFGM) in terms of quantitative velocity v and flow geometry, visualized by the grey fluid domain, is very high.

In addition to the velocity magnitude, the direction of the flow was predicted quite well by the simulation, as shown in Figure 6.4. For t_3, this is further clarified by the direct comparison of the flow direction within Figure 6.5. The coloured area represents the PIV result which agrees very well to the contour lines of the PFGM simulation; both of which are divided into $30°$ sections. At t_4 the flow-fronts have almost fully connected and now only one approximately linear flow profile can be seen. No air was trapped when the two beads merged. Finally, at t_5 the adhesive has flown into a circular shape, however the velocity scatters and is underestimated by the PIV analysis at t_4 and t_5 compared to the simulation result. Unsurprisingly, the flow velocity during the squeezing process is always maximal at the fluid edges.

The PIV methodology struggled to handle regions with zero velocity, since slight scattering around the zero coordinate can be seen in the non-fluid areas at every time, however as expected the simulation fully matches at these zones. The fact that the beads first met slightly to the left was also captured by the simulation, as the real applied fluid geometry served as input. Overall, the velocity magnitude and direction (the vector fields) generated with PIV as well as the fluid distribution over time agree very well to those simulated numerically using the PFGM, cf. Figure 6.4.

6.2.2 X-Pattern

During the first three frames shown, from t_1 to t_3, the X-pattern, which initially looks somehow like a thick bone, flows into a butterfly form. The corresponding flow profiles along the path are approximately linear, as shown in Figure 6.6. Looking from above (in 2D) one can see that the bays of the X-pattern are flowing faster than the rounded tips, as visualized by the PIV and PFGM images in Figure 6.7, thus at t_4 a nearly rectangular adhesive

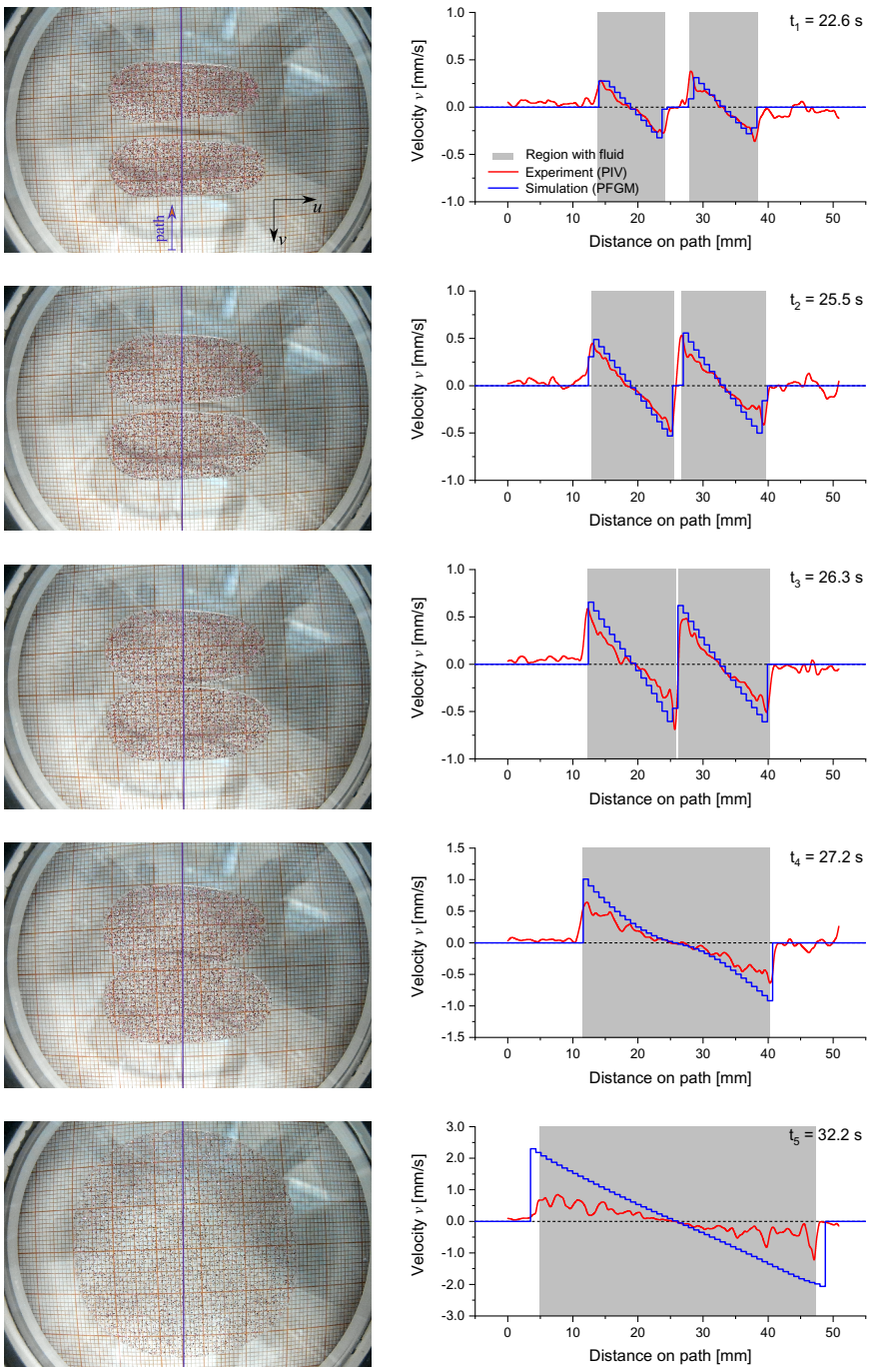

Figure 6.3: II-Pattern fluid distribution (left, see video) and velocity along path (right) for characteristic times during squeeze flow. Simulation data taken from [47].

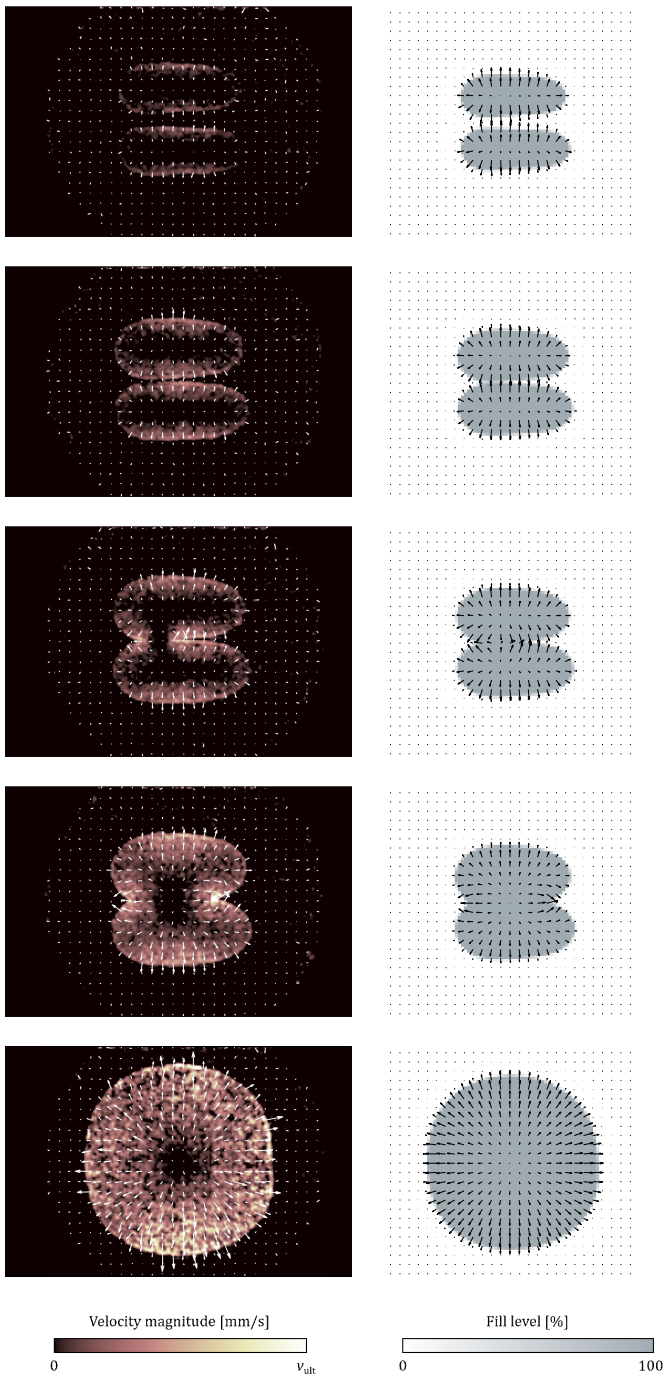

Figure 6.4: II-Pattern fluid velocity field calculated with PIV (left, see video) compared to PFGM simulation results (right). Simulation data taken from [47].

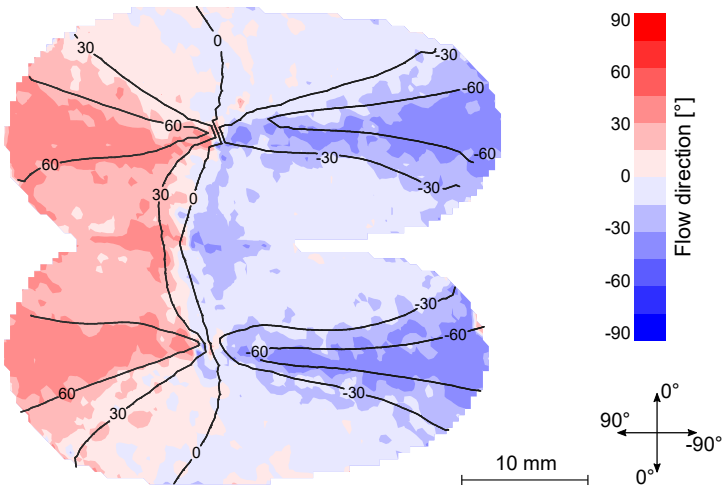

Figure 6.5: Fluid flow direction of the II-pattern at time t_3, comparison between PIV (coloured area) and PFGM simulation (contour lines). Simulation data taken from [46].

area is achieved (if the squeeze process would stop here). At t_5 the fluid has flown into an elliptical-like shape and short after that the target gap is reached and the squeeze process ends.

Within the first three time steps shown here, the agreement between the quantitative path data from PIV and PFGM which includes the velocity magnitude and direction is very high. However, later during the squeeze process the velocity of the PIV analysis is scattering and is underestimated compared to the simulation results. Just like before, the PIV methodology struggles to handle regions with zero velocity, which will be discussed later. However, the 2D fluid distribution during squeeze and the qualitative flow direction calculated with PIV and PFGM match very well. No air pockets have formed during the squeeze process of the X-pattern.

6.3 Remarks on PIV

Independent of the pattern investigated, the PIV methodology systematically underestimated the velocities at the end of the squeezing phase (at t_4 and t_5) compared to the simulation results. In addition, the scatter of the calculated flow profiles increased to the end phase, whereby the qualitative flow profile is still correct. This has two reasons.

The first and main reason for the underestimation of velocities at t_4 and t_5 might result from the characteristics of the fluid flow itself. Similar as for pipe or channel flows, a no-

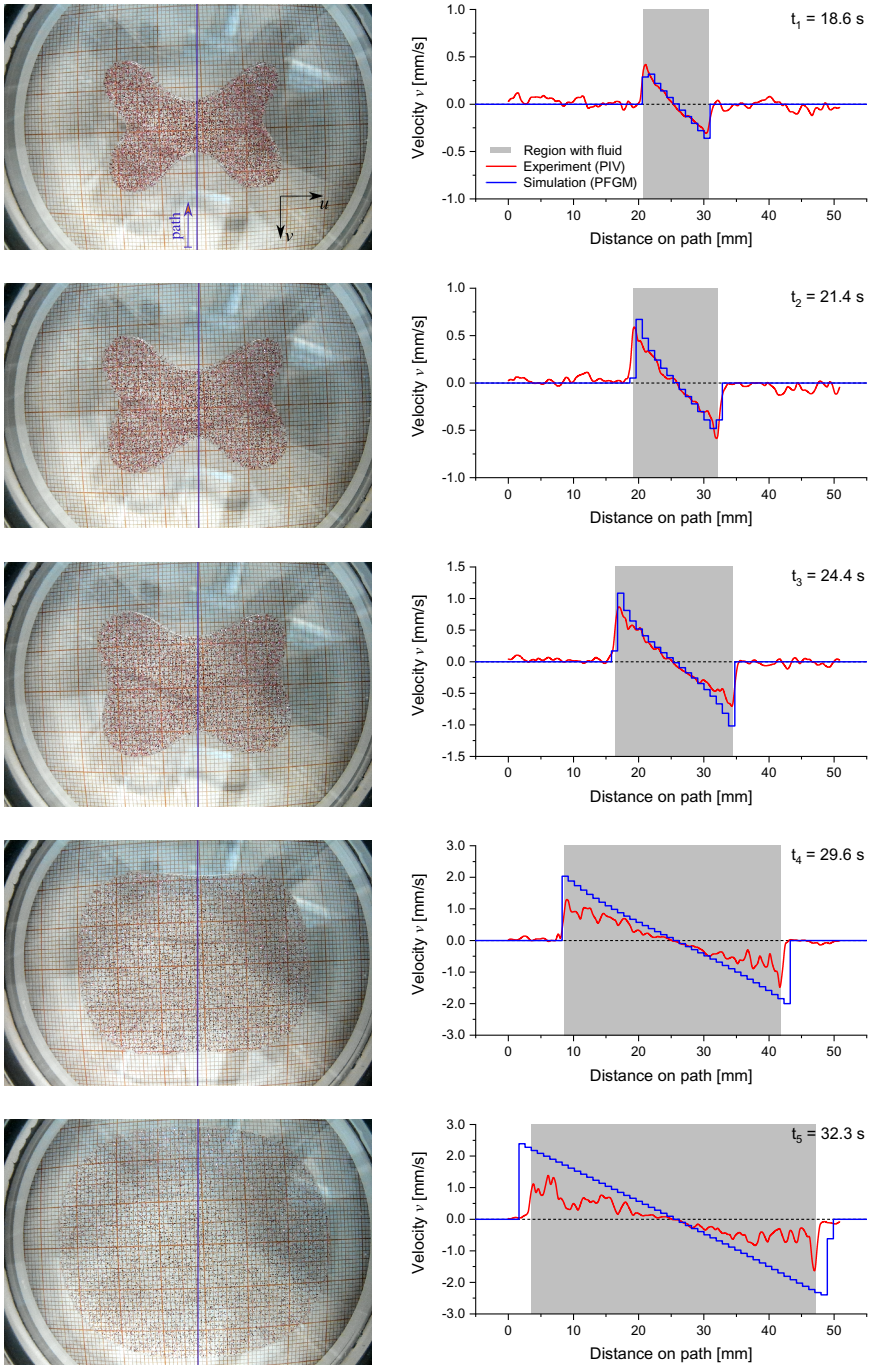

Figure 6.6: X-Pattern fluid distribution (left, see video) and velocity along path (right) for characteristic times during squeeze flow. Simulation data taken from [47].

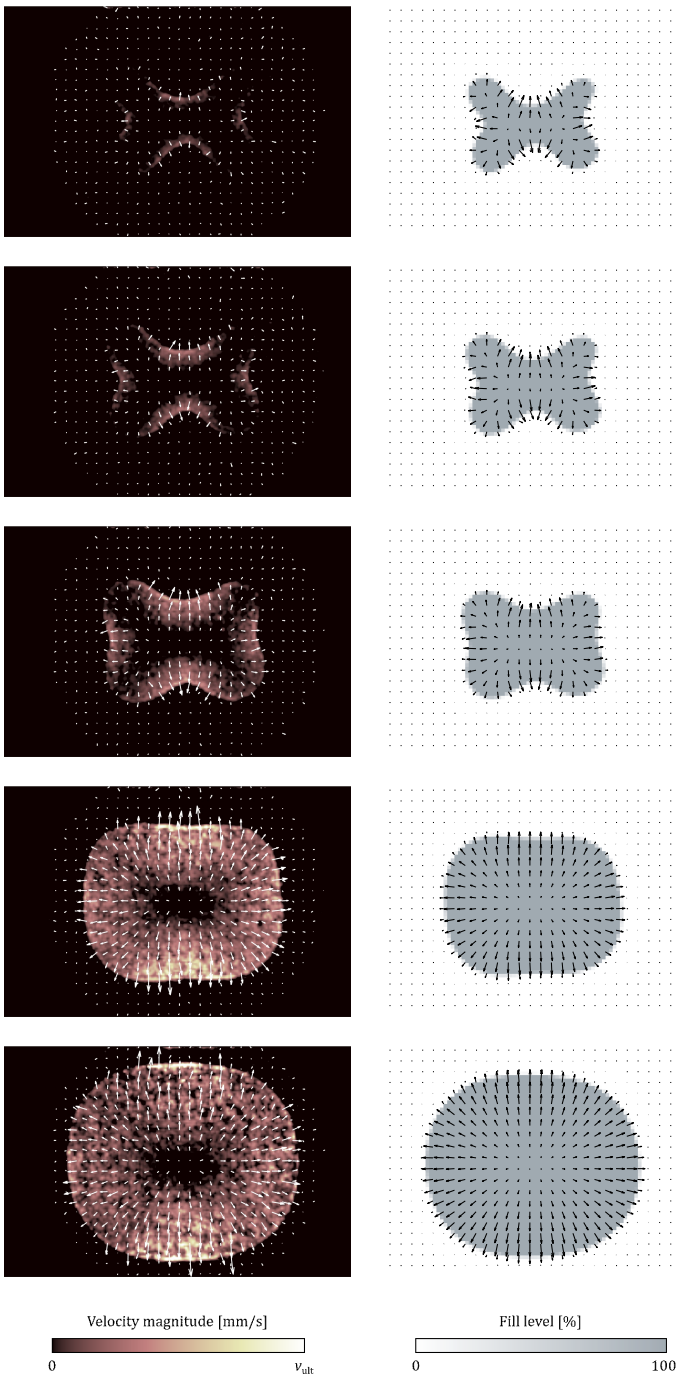

Figure 6.7: X-Pattern fluid velocity field calculated with PIV (left, see video) compared to PFGM simulation results (right). Simulation data taken from [47].

slip boundary condition ($v_{BC} = 0$) at the squeezing surfaces can be assumed in the case of squeeze flows (cf. section 7.4 for more details). The maximum flow velocity appears at half of the gap height because of symmetry; consequently, a non-constant flow profile is present in height direction during squeeze flow. Furthermore, the particles are not positioned at the exact same layer in height, thus raising the question which velocity is determined by the PIV methodology. Fortunately, PIV doesn't consider single particles but evaluates an interrogation area, thus, if the particles in that area are randomly distributed in height, we can assume that the calculated PIV velocities correspond to the average velocity along height – which is desired and average velocities are also calculated in the numerical simulation. However, during squeeze, the fluid continuously spreads and wets the boundary glass surfaces so more particles are transported near to the boundaries (which is visualized by the streamlines of a CFD study, shown in Figure 6.8) with progressing squeeze; note that the flow at the boundaries is slower because of the no-slip behaviour. Consequently, the assumption, that a group of particles in an interrogation area are randomly distributed along the height, is no longer justified at the end of the squeeze phase, and thus might be the reason for the systematic underestimation of velocities by the PIV methodology at t_4 and t_5.

The second and primary reason for the increasing scattering might result from the decrease in areal particle density during the squeeze phase because the fluid spreads. Looking from above, like the camera is filming, the distance between the particles increases due to the spread, thus the areal particle density decreases. Therefore, spots with too few or almost no particles appear, and the flow profile calculated with PIV is scattering more because the

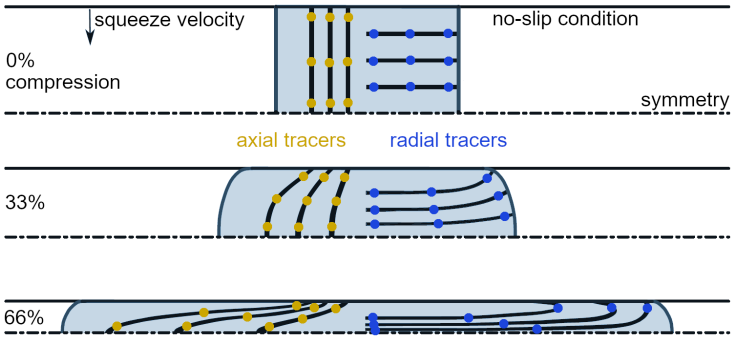

Figure 6.8: Cross-sectional view of a compaction sequence with axial and horizontal pathlines on which three tracer *particles* are positioned. Top: initial configuration, middle: 33% compaction, bottom: 66% compaction, taken & edited from [14]. The radial (blue) tracers indicate that particles near the symmetry line can flow vertical to the surfaces whereby their horizontal velocity (that was captured by PIV) decreases due to the no-slip boundary condition.

final interrogation area of 16×16 px is too small, i.e. simply speaking, the algorithm loses track in these regions. This might be prevented by using more particles.

The results obtained in this chapter have high significance and represent new insights in the context of adhesive bonding. The optimization of adhesive pattern can lead to huge reduction of adhesive needed as well as adhesive excess and waste (cf. X-pattern). Further, optimized application pattern can make reworks and cleaning unnecessary. Advanced application pattern which can consist of multiple adhesive beads do not pose any problems, flow fronts merge easily without any formation of imperfections (cf. II-pattern) as long as no air gets trapped.

It is reminded that a transparent model fluid with tracer particles was used as a substitution for real adhesives which are generally non-transparent. Only this substitution made it possible to characterize the flow using the PIV methodology and it is further justified because the range of viscosity of the model fluid is well comparable with those of highly viscous adhesives. The non-Newtonian, i.e. the shear thinning behaviour of the silicon oil, which can be described by the Yasuda-law, is also characteristic for many adhesives. A major difference between the used silicone oil and real adhesives is the wettability; however, here the flow is dominated by the squeezing boundaries, which literally *force* the fluid to flow, independent of its ability to wet a surface, thus effects resulting therefrom can be neglected. That said, the only question which remained unanswered until now is the influence of the surface condition — a topic that is addressed in the following chapter.

7 Do Surface Structures need to be Modelled?

With a thorough characterization of the behaviour of the squeezed fluid now in place, it's natural to inquire about the impact of surface structure. This inquiry gains significance because various surface pre-treatments are typically necessary for bonding, depending on the intended application. These treatments alter the surface's characteristics before the squeezing process, raising the question whether and how these modifications affect the flow of the adhesive. Moreover, it becomes imperative to explore whether the surface structure should be factored into the simulation of the PFGM to enhance the optimization of adhesive application patterns.

7.1 Surfaces and Pre-treatments

The material surfaces investigated in this chapter consist of float glass and construction steel (S235JR). In addition to the untreated reference surfaces, two different pre-treatment methods, which are widely used in adhesive applications, are considered – blasting and flame treatment. The different combinations of substrates and surface pre-treatment methods are illustrated in Figure 7.1.

Blasting was performed with high-grade corundum (grain F100) for both, glass and steel, until the surfaces were visually evenly roughened. Before and after blasting every surface was cleaned with isopropanol. The flame treatment, which generates a pyrolytic coating, was applied on the glass surfaces using a hand-held burner at a distance of approximately 15 cm to the surface; the flame was passed back and forth over the surface five times. The flame treated surfaces were only cleaned before the pre-treatment was applied.

To characterize the effect of the surface pre-treatments, roughness and surface energy (in terms of contact angle) were measured. The surface characteristics (i.e. arithmetic mean roughness R_a, root mean square roughness R_q, mean peak-to-valley height R_z and contact angle θ) were determined with a surface texture measuring instrument (MarSurf M300C, *Mahr GmbH*) and a contact angle measuring device (DSA100, *Krüss GmbH*) using water

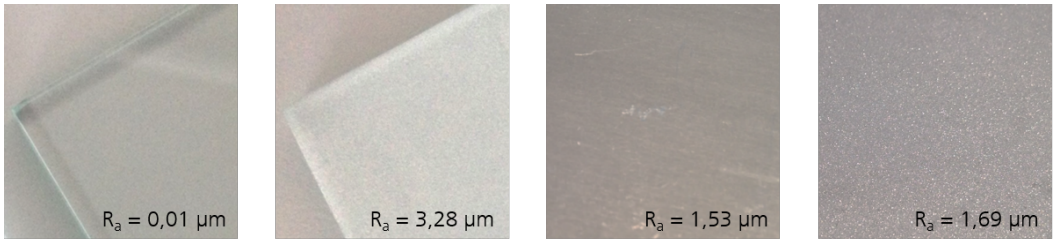

Figure 7.1: Considered glass and steel surfaces before and after blasting pre-treatment. From left to right: glass-untreated, glass-blasted, steel-untreated, steel-blasted.

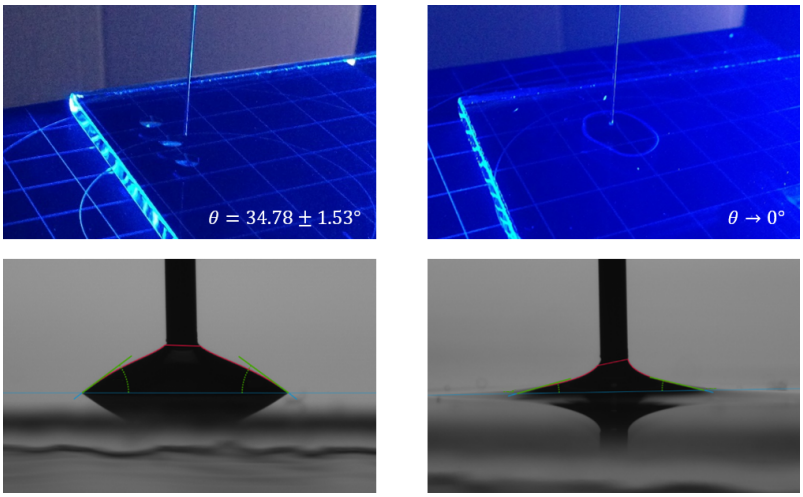

Figure 7.2: Measurement of the contact angle using water and air as liquid and gas phases. Untreated glass surface (left) vs. flame treated glass surface (right).

and air as fluid and gas phases, see Figure 7.2. The contact angle measurements are performed with the needle-in-drop configuration and the contact angle is determined by curve fitting of the drop contour which was done with the *Krüss* software. The needle material and geometry were considered for the evaluation of the contact angle since they can affect the results. The volume of the water droplet was carefully controlled to provide a stable measurement.

The untreated glass surface exhibited an average roughness of $R_a = 0.01 \pm 0.00$ µm and a mean peak-to-valley height of $R_z = 0.06 \pm 0.01$ µm. After blasting with high-grade corundum, the latter increased to $R_a = 3.28 \pm 0.02$ µm and $R_z = 19.37 \pm 0.14$ µm. The contact angle of the glass surface decreased from $\theta = 34.78 \pm 1.53°$ (untreated) to approximately $\theta \to 0°$ (flame treated), which indicates that the surface became highly hydrophilic as desired for bonding. For the steel surface the following surface parameters were determined before pre-treatment: $R_a = 1.53 \pm 0.00$ µm and $R_z = 9.91 \pm 0.03$ µm

Table 7.1: Surface parameters before and after blasting treatment (arithmetic mean roughness R_a, root mean square roughness R_q and mean peak-to-valley height R_z).

Material	Pre-treatment	R_a [µm]	R_q [µm]	R_z [µm]
Glass	untreated	0.01 ± 0.00	0.01 ± 0.00	0.06 ± 0.01
Glass	blasted	3.28 ± 0.02	4.12 ± 0.02	19.37 ± 0.14
Steel	untreated	1.53 ± 0.00	1.93 ± 0.00	9.91 ± 0.03
Steel	blasted	1.69 ± 0.07	2.19 ± 0.09	11.84 ± 0.21

and after pre-treatment: $R_a = 1.69 \pm 0.07$ µm and $R_z = 11.84 \pm 0.21$ µm. All further surface parameters are listed in Table 7.1.

7.2 Series and Procedure

To investigate the influence of surface condition on the squeeze flow, the measuring procedure presented in chapter 4 was followed and the silicone oil as before was used. The HSC was calibrated as mentioned and zeroed every time a new material is tested to account for any differences in the substrate thickness that would impact the gap size.

To further reduce measuring errors due to deviations from this re-calibration (as no re-calibration is perfect), one side of every material-plate remains untreated while the other one is pre-treated according to section 7.1 so that the surface-plates can be turned over without changing the gap height – eliminating the need of recalibration in-between groups and thus providing optimal comparability.

At the beginning of each experiment a circular drop with a target mass of $m = 0.679\,\mathrm{g}$ was applied on the bottom test surface. Starting from an initial gap of $h_0 = 3.5\,\mathrm{mm}$, the drop is squeezed with a velocity of $w = 0.10\,\mathrm{mm/s}$ until a final gap of $h_{\mathrm{fin}} = 0.3\,\mathrm{mm}$ is reached. Each experiment is repeated three times ($n = 3$) and an analysis of variance (ANOVA) is performed to test the statistical significance.

To investigate if the no-slip condition is valid, a special series of experiments is performed. Therefore, some tracer particles are placed on the surfaces before the fluid drop is applied on top, thus these particles are positioned as close as possible to the fluid-surface interface. Then a squeeze flow experiment is performed, and the movement of the particles is tracked to see if there is any flow velocity in the edge layer.

7.3 Measured Squeeze Force

The force needed to squeeze the fluid at a constant velocity of $w = 0.10\,\mathrm{mm/s}$ increases non-linear with the corresponding gap height reduction. The force-displacement behavior is very reproducible across all experiments, independently of the material or surface pre-treatment used, as shown by Figure 7.3 (a-c). Within the first 80 % of the squeeze process, the force remains almost unchanged, while only in the last 20 % the exponential character of the force displacement curves becomes apparent. The differences in terms of average maximum forces for the untreated and pre-treated surfaces are quite small, i.e. 27.3 N (3.0 % rel. difference) for untreated vs. blasted, 8.2 N (0.7 %) between glass untreated vs. flame treated, and 16.3 N (2.1 %) between steel untreated vs. blasted, respectively. These differences are so small that they may be considered irrelevant for industrial applications, even if the joining process is controlled in force instead of displacement.

An analysis of variance (ANOVA) was performed to investigate any statistic significant differences achieved by the different surface materials or pre-treatment methods. Since a recalibration was performed between the experiments with different materials no sound statement is possible between the surface materials without normalizing the data between groups. To perform the ANOVA the average maximum force of a group was considered and normalized to their corresponding maximum value. According to the ANOVA, no significant difference could be observed regarding the squeeze flow, neither comparing different surface materials nor pre-treatment methods, as shown in Figure 7.4.

7.4 Boundary Condition

The experimental results agree well with numerical simulation, see Figure 7.3 (d), which are similar to those performed in [46, 67]. For the simulation, the decisive question is whether the no-slip condition applies to the wall or whether wall sliding can occur. If the latter is the case, the resistance of the fluid to shear decreases significantly, which in turn results in a considerable reduction of the force to be applied. Since the no-slip condition was used in the simulation and the calculated forces correspond very well with the measured forces, it seems likely (according to the numerical simulations) that the no-slip condition is fulfilled both in the reference test and for the pre-treated surfaces.

In contrast, the series of squeeze flow experiments with particles positioned next to the fluid-surface layer indicates that the no-slip condition is not valid, because during squeeze some of the particles did move, independent of the surface pre-treatment, as shown in Figure 7.5. However, it should be mentioned that, due to the particle size, the observed particle

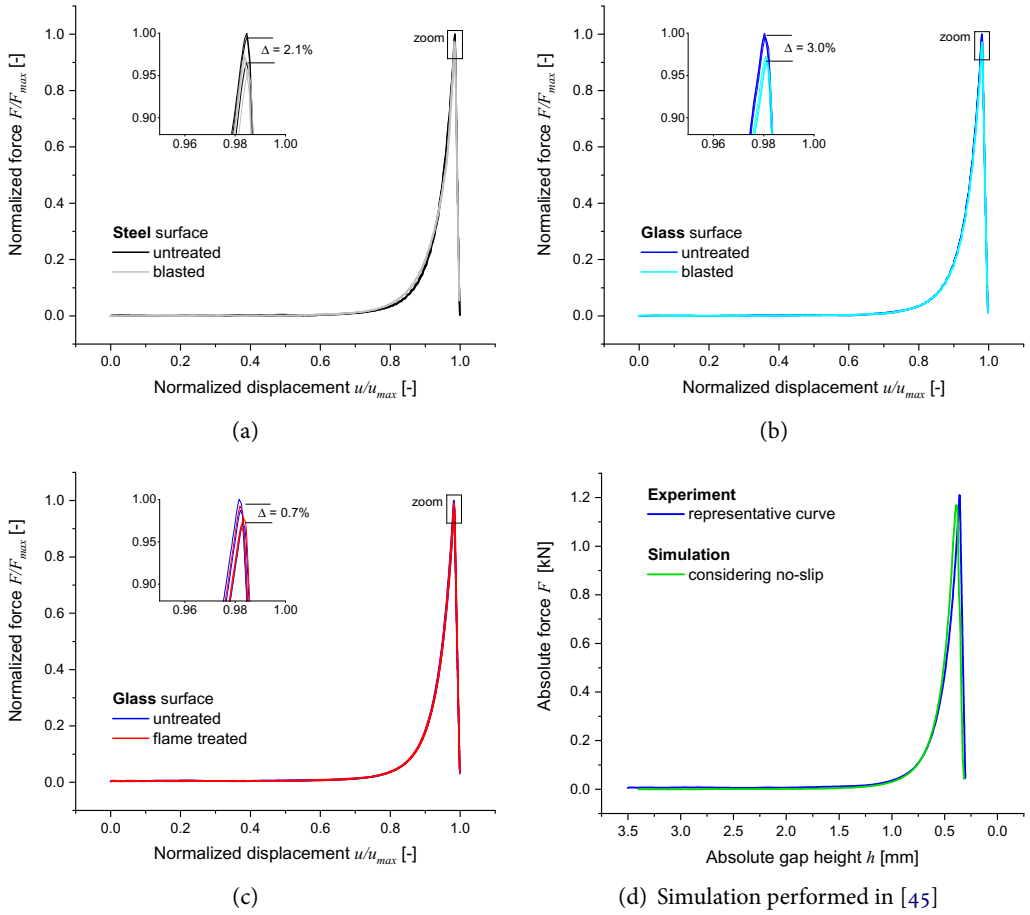

Figure 7.3: Force-displacement behaviour during squeeze flow for all investigated surfaces and pre-treatments (a-c) and comparison with numerical simulation considering no-slip condition (d).

movement only shows the fluid velocity very close to the fluid-surface interface, but not exactly at the interface. Therefore, the question of whether the no-slip condition is valid and how it is influenced by the surface pre-treatments cannot be answered with certainty.

7.5 Observed Flow Propagation

In each experiment the fluid propagates in a circular shape, which diameter was determined as described in subsection 4.1.5. By comparing the diameters in different experiments at the same time-step, i. e. at $t = 30$ s, a very good agreement was observed, regardless of the substrate (glass or steel) and the pre-treatment (roughening or flame-treatment). In figures,

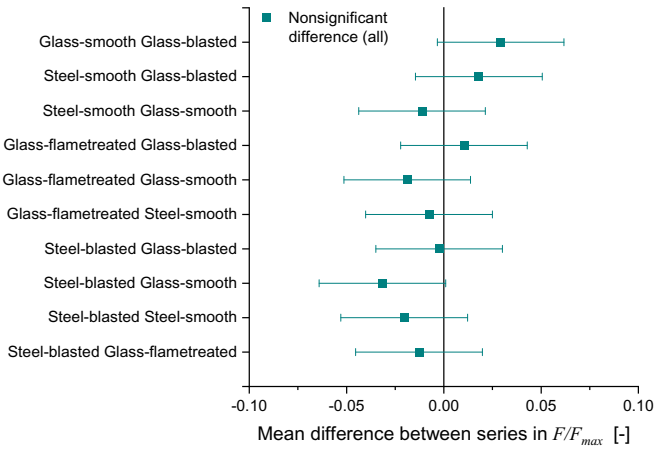

Figure 7.4: Analysis of variance of the normalized average maximum forces from all series.

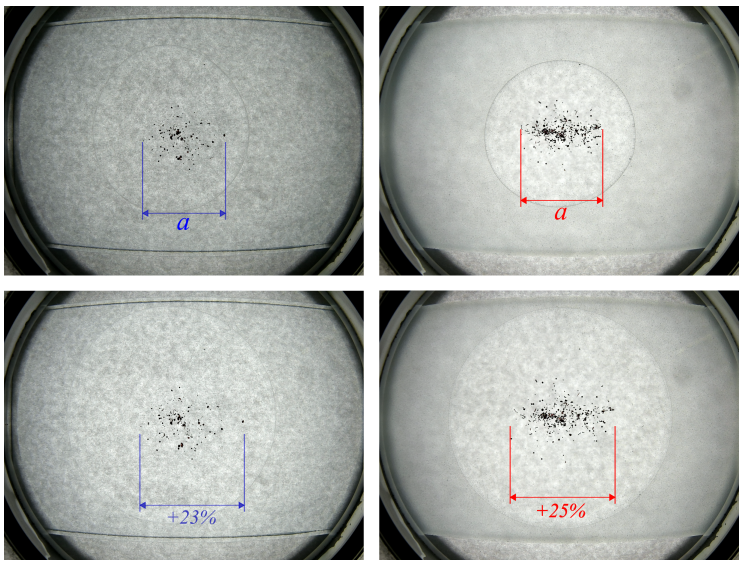

Figure 7.5: Flow tracking with particles positioned next to the fluid-surface interface: glass untreated (left), glass blasted (right), before squeeze (top) after squeeze (bottom).

there is almost no difference in diameter between the untreated and blasted glass or steel surfaces (i. e. glass-untreated: $D = 41.5 \pm 0.3$ mm vs. glass-blasted: $D = 41.3 \pm 0.3$ mm, and steel-untreated: $D = 40.4 \pm 0.2$ mm vs. steel-blasted $D = 40.4 \pm 0.7$ mm). This further indicates that pre-treatment has no significant influence on the squeeze flow.

8 Interim Conclusions

Before diving into the main part of this thesis — the optimization of adhesive application pattern — let's take a moment to draw an interim conclusion. This Part II was dedicated to present and validate the PFGM tool, that — *spoiler alert* — proved to be an ideal method for the planed optimization of adhesive application, which will follow in Part III. The PFGM simulation went through extensive validations and the requirements that are needed to be fulfilled were addressed in terms of three research hypothesis that are addressed below.

8.1 Combining PIV with the Hele-Shaw Approach

Squeeze flow processes which occur during joining of adhesive bonds were investigated experimentally by adapting the Hele-Shaw approach and combining it with PIV as proposed in chapter 4. A highly viscous fluid was used to which tracer particles were admixed to observe and characterize the flow of two different application pattern. The selected scenarios included pattern which are likely and unlikely to trap air, as flow fronts would merge during the compaction process. The experiments were performed using the adapted Hele-Shaw cell and the squeeze forces were measured in relation to time and gap height. In addition, the flow shape of the patterns was recorded with a camera to further allow the calculation of the corresponding velocity fields using PIV. The combination of PIV with the HSC proved to be a new method that is capable to measure the flow characteristics of squeeze processes qualitatively and quantitatively with reasonable accuracy, so that the hypothesis:

> **Hypothesis #1:** Adhesive squeeze flow processes can be experimentally characterized by combining PIV and the Hele-Shaw approach. ✓

can be confirmed. Especially the X-pattern showed that the optimization of adhesive application pattern holds great potential to reduce the amount of adhesive needed to minimize adhesive waste and further reduce working tasks like cleaning and refinishing. Flow fronts are able to merge easily without the formation of imperfections if done correctly, which further expands the design possibilities of new and innovative application patterns.

8.2 Accuracy of the Partially Filled Gap Model

The experimental investigations performed with the HSC and extended with PIV were intensively compared to PFGM simulations that were performed in [46] and [47]. As demonstrated in much detail in chapter 5 and chapter 6, the simulation results have reached a high level of agreement with the experiments in terms of squeeze forces, flow geometry as well as velocity magnitude and direction, so that the hypothesis that:

> **Hypothesis #2:** The Partially Filled Gap Model provides the accuracy that is needed for the optimization of adhesive application pattern. ✓

can be confirmed. The Yasuda flow law proved to be very accurate in predicting the force-displacement behaviour of these processes. However, the optimization intended to be developed in Part III does not target the force, but the shape of the resulting pattern. Therefore, the high level of accuracy that the PFGM achieved in terms of predicting the shape of the flow pattern as well as the calculation of velocity vector fields, especially the velocity magnitude and direction, will be a huge advantage.

8.3 Influence of Surface Pre-Treatments

In chapter 7 the influence of surface pre-treatments on the squeeze flow process of adhesives was investigated experimentally. Two materials (glass and steel) and two surface pre-treatments (blasting and flame-treatment) as well as an untreated reference surface were considered, in-between which a highly viscous adhesive-like fluid was squeezed.

For the subset of materials and methods considered, the investigations indicate that the adhesive squeeze flow process is independent of the substrate surface condition, even if they were pre-treated, thus the third hypothesis can be approved:

> **Hypothesis #3:** The surface structures of the substrates which squeeze the adhesive can be neglected in the Partially Filled Gap Model simulation. ✓

However, the limited amount of surface materials and pre-treatment methods considered does not allow to claim that the squeeze flow process is independent for *any* surface pre-treatment even though its general validity seems plausible.

These findings have practical implications for the numerical modelling of squeeze flow phenomena since the surface condition does not appear to be a significant input parameter. Thus, the specific determination of surface parameters such as surface roughness or energy is not required for simulation and thus neither for the development of the optimization algorithm.

Now that the PFGM has been successfully validated and proven to be sufficiently accurate, the development of an optimization algorithm that utilizes this tool can pe performed.

Part III

How to Optimize Adhesive Application Pattern

9 Development of a Numerical Optimization Algorithm

This chapter presents a numerical method that aims to optimize adhesive application in manufacturing processes by finding initial adhesive application patterns that flow into any desired bond geometry. This is achieved by considering the joining kinematics, which involves pressing two substrates together and allowing the adhesive to flow and wet both surfaces. By using this method, the adhesive application pattern can be precisely controlled, resulting in a more efficient manufacturing process.

The optimized application pattern ensures that the adhesive flows into the desired shape, reducing the need for additional shaping or cleaning of excess adhesive by hand. This results in higher product quality and fewer defects, as well as reduced material costs and a more streamlined production process. Overall, the method presented in this chapter aims to improve the efficiency and quality of manufacturing processes that involve the use of adhesive bonds. It provides a clear and practical approach to optimizing the application of adhesive which can be useful for a wide range of industries that rely on adhesives in their manufacturing processes.

9.1 Optimization Methodology

The strategy of the optimization procedure is to iteratively modify an application pattern so that the resulting adhesive distribution, in which the optimized pattern is squeezed into, is equal to the desired shape of the bond. Before the methodology of this procedure is explained in detail a short definition of this theoretical problem is given ahead.

9.1.1 Problem Definition

Two substrate surfaces which have a perfectly plane topology, are ideal rigid and infinitely large in length and width dimensions are assumed. The surfaces can move relative to each other, which can be described by a defined velocity and kinematics (linear and rotational translation, or a combination thereof). This thesis focuses on the linear squeeze kinematic

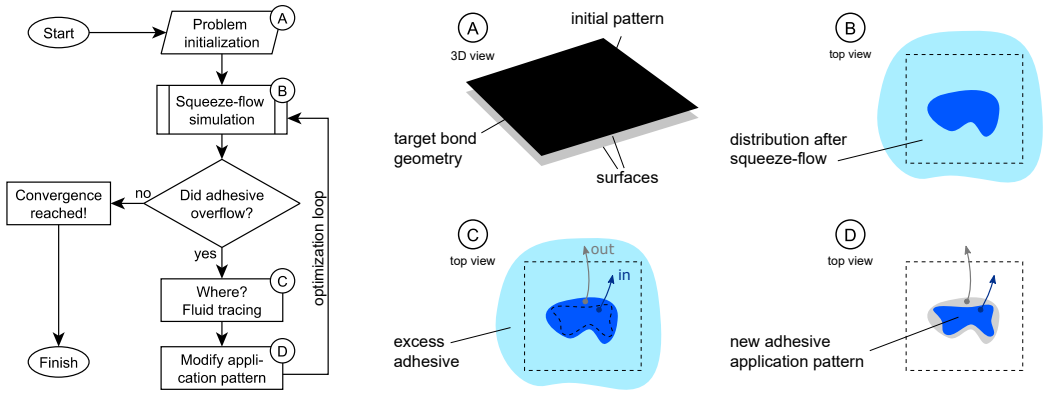

Figure 9.1: Flowchart and schematic representation of the methodology for optimizing adhesive application patterns.

(where the substrates stay parallel to each other): beginning with an initial gap height of h_0, the substrates approach each other with a constant squeeze velocity of w until the final gap height of h_{fin} is reached.

The object of interest, the adhesive, is positioned in-between both surfaces, which is shown in Figure 9.1 (A). It is a highly viscous fluid which can be described by a certain viscosity law. Further information about the modelling of the fluid were given in subsection 2.4.3.

The shape in which the adhesive is applied in-between the surfaces at a gap height of h_0 is called *initial pattern*. During squeeze the initial pattern flows and subsequently reaches its *resulting distribution* when the final gap of h_{fin} is obtained.

9.1.2 Optimization Procedure

The first step of the optimization methodology is to initialize the problem, see Figure 9.1 (A). This includes all the information about the targeted bond geometry as well as the initial adhesive application pattern. Furthermore, the squeeze kinematic, including the initial gap height h_0, squeeze velocity w and final gap height h_{fin}, as well as the fluid viscosity law $\eta(\dot{\gamma})$ are defined.

Now, a squeeze-flow simulation is performed, and the resulting adhesive distribution is determined, as shown in Figure 9.1 (B). This can be done by using numerical fluid simulation tools – details on the simulation will follow in subsection 9.1.3. Next, the initial domain of adhesive, which has flown outside of the target bond geometry, see Figure 9.1 (C), will be gradually removed from its corresponding initial pattern – more details on the removal will follow in section 9.2.

Hereby, a new initial pattern is created, see Figure 9.1 (D), which is more likely to flow into the desired bond geometry. However, due to the new shape of the pattern, the flow will also slightly change, and an iterative procedure is necessary. The process is repeated in an optimization loop, as illustrated in the simplified flowchart of Figure 9.1, until the algorithm has converged, i.e. the application pattern has reached a steady state. In this case there shouldn't be any more excess adhesive after squeeze and the pattern is finally *optimized*.

9.1.3 Squeeze-flow Simulation

To calculate the flow characteristics of the squeeze process (i.e. the velocity field, fluid distribution, pressure, etc.) the Partially Filled Gap Model (PFGM) was used. As described extensively in subsection 2.4.2, this tool was developed by the Institute of Dynamics and Vibrations (IDS) from the Technical University of Braunschweig and is kindly provided for this study. It was validated in-depth and confirmed for the fast and reliable calculation of flows in narrow gaps, cf. Part II of this thesis as well as the publications [47, 65–69], including the consideration of non-Newtonian fluids [46].

Besides fast calculation times due to some simplifications of the Navier-Stokes equations (following the Reynolds equation), the main advantage is its stable and reliable solving of squeeze flows in narrow gaps. The fluid is discretised with regularly arranged cells which are given a fixed number of state variables (volume, pressure, velocity). For more details on the formulation of the state equations and the algorithm, readers may consult subsection 2.4.2 or [65–67, 69]. The PFGM is coded in Matlab which leaves all options for extensions and implementations, like in this thesis, which addresses the optimization of adhesive application pattern.

9.2 Numerical Implementation

9.2.1 Criteria for Fluid Removal

The key part of the algorithm is to iteratively remove fluid from an initial pattern according to a defined criterion, as indicated, but not fully explained in subsection 9.1.2. The original idea was to remove *every* cell of fluid *completely* from the initial pattern once it has flown outside of the desired bond geometry after the squeeze process. This simple approach worked somehow ok, but was far from perfect, so it is further improved as follows.

Firstly: once fluid has overflown at any iteration step, the initial filling degree of the corresponding cell is only gradually reduced by a pre-defined *reduction ratio*, RR, instead of completely removing the entire cell. And secondly: not all of the initially filled cells which

have overflown, but only a pre-defined percentage (*elimination rate*, ER) of them, i.e. the cells which have flown furthest out of the desired bond geometry, will be reduced according to the RR. These two strategies correspond to a numerical damping of the algorithm.

This procedure penalizes cells which have overflown further than others and therefore, in combination with the gradual removal (soft kill), improves the speed and stabilizes the convergence behaviour of the algorithm. A detailed flowchart of the algorithm is shown in Figure 9.2. During development and testing of the algorithm a reduction ratio of RR $= 0.25$ (meaning that at least four iterations are needed to remove one entire cell) and an elimination rate of ER $= 0.10$ (which ensures that only the furthest 10% of cells overflown are modified at once) was found to be efficient.

Furthermore, the initial pattern of the first iteration should be chosen in a way that it completely overflows the boundaries of the target bond after the first squeeze process. In this way the algorithm approaches the solution *from one side* and can be kept simple, thus no bi-directional procedure, where material also needs to be added (in addition to its removal) is necessary. An always working guess for the initial pattern of the first iteration is to simply start with the target bond geometry.

9.2.2 Implementation of Fluid Removal

The implementation of the optimization algorithm was performed in *Matlab R2020b* to directly connect with the used squeeze flow simulation tool (PFGM). For the implementation, the domain is discretized into n_x times n_y finite cells that are labelled with the running row and column variables j and k. To initialize and modify an **ini**tial adhesive pattern a matrix, $\mathbf{M}^{\text{ini}}$, is used to assign each cell with a filling degree $m_{j,k}$, as defined according to Equation 9.1:

$$ {}^{i}\mathbf{M}^{\text{ini}}_{j,k} = m_{j,k} = \begin{bmatrix} m_{1,1} & m_{1,2} & \cdots & m_{1,n_\text{y}} \\ m_{2,1} & m_{2,2} & \cdots & m_{2,n_\text{y}} \\ \vdots & \vdots & \ddots & \vdots \\ m_{n_\text{x},1} & m_{n_\text{x},2} & \cdots & m_{n_\text{x},n_\text{y}} \end{bmatrix} \text{ with } \begin{cases} j = 1, \cdots, n_\text{x} \\ k = 1, \cdots, n_\text{y} \end{cases} \tag{9.1} $$

Each cell can either be filled, unfilled or partly filled with fluid, which is defined by the cells filling degree, which values can range from zero (unfilled) to one (fully filled): $m_{i,j} \in [0, 1]$. In the same way the **res**ulting fluid distribution, is stored in a matrix called $\mathbf{M}^{\text{res}}$ as well as the **tar**get bond geometry being defined by a matrix $\mathbf{M}^{\text{tar}}$, all of which is exemplary illustrated in Figure 9.3.

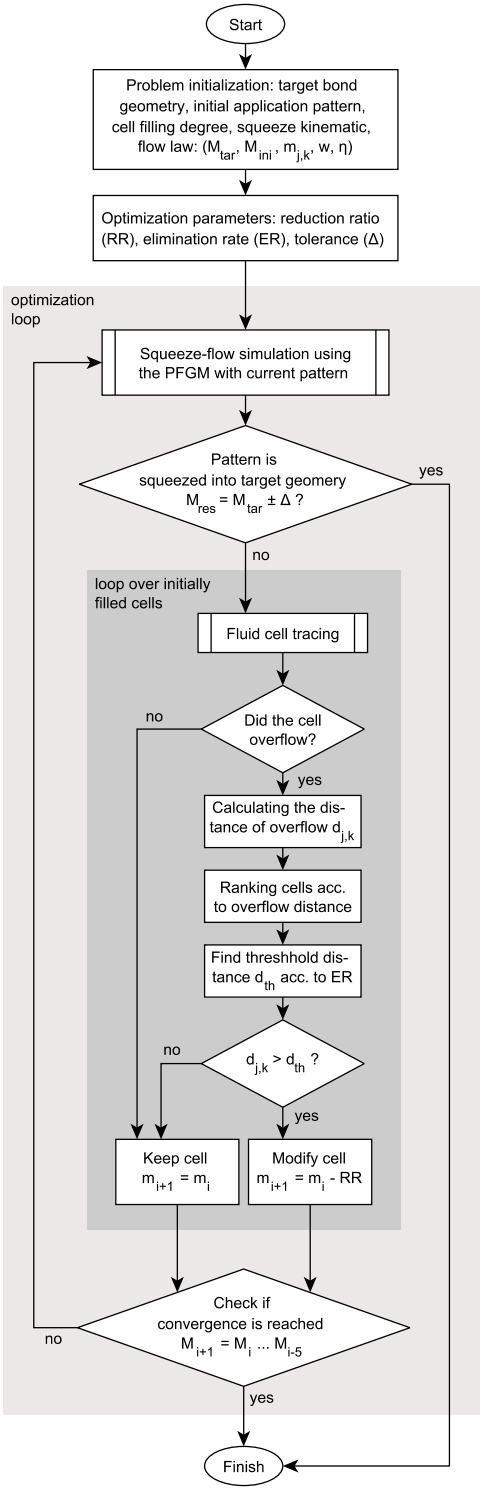

Figure 9.2: Detailed flowchart of the optimization algorithm.

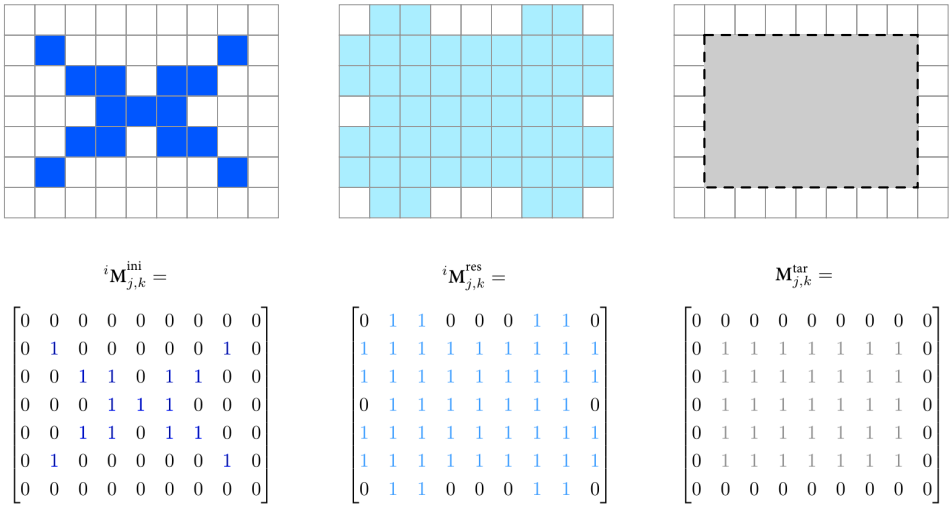

Figure 9.3: Exemplary illustration of initial application pattern, resulting distribution and target bond geometry definition using matrices.

The pressure p and velocities u and v of each cell are calculated by the PFGM in a transient simulation. The simulation starts with the initial gap height h_0 and ends with the final gap of h_{fin}, which is approached with a squeeze velocity w. One of these calculations represents an iteration step i of the optimization algorithm and gives the resulting fluid distribution $\mathbf{M}^{\text{res}}$. In each iteration step the resulting fluid distribution, ${}^{i}\mathbf{M}^{\text{res}}_{j,k}$, is compared to the target fluid distribution, ${}^{i}\mathbf{M}^{\text{tar}}_{j,k}$, in order to track the optimization progress i.e. the remaining over- and underfilled domains of fluid.

If $\mathbf{M}^{\text{res}} \neq \mathbf{M}^{\text{tar}} \pm \Delta$, the flow path of each cell (in-between ${}^{i}\mathbf{M}^{\text{ini}}$ and ${}^{i}\mathbf{M}^{\text{res}}$) is traced after each iteration step i, starting from the centre of each cell using a tracing function, which is further explained in subsection 9.2.3. In short, this function calculates the flow path and the distance of overflow, $d_{j,k}$, of each initially filled cell j, k. The information of overflow is then stored into a matrix ${}^{i}\mathbf{D} = d_{j,k}$ which is further converted into a column vector and sorted to determine a threshold distance d_{th}. The threshold distance corresponds to the distance where the elimination rate of ER $= 10\%$ is reached, i.e. it marks the distance beyond which overflown cells belong to the furthest flown 10%, as illustrated by Figure 9.4.

Subsequently, the filling degree of each cell which was initially filled (${}^{i}\mathbf{M}^{\text{ini}}_{j,k} > 0$), has overflown (i.e. ${}^{i}\mathbf{M}^{\text{tar}}_{j,k} = 0$), yet so far that it falls under the elimination rate of ER $= 10\%$ (${}^{i}\mathbf{D}_{j,k} > d_{\text{th}}$), will be gradually reduced by the reduction ratio of RR $= 0.25$ of the initial filling degree according to Equation 9.2.

$$ {}^{i+1}\mathbf{M}^{\text{ini}}_{j,k} = {}^{i}\mathbf{M}^{\text{ini}}_{j,k} - \text{RR} \tag{9.2} $$

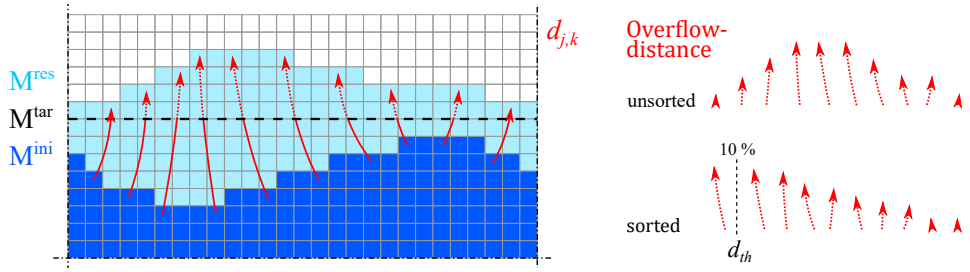

Figure 9.4: Illustration of overflow distance (dotted part of the red arrows) and exemplary determination of the threshold distance d_{th}. Only some cells are traced for illustration purposes.

The iterative optimization process continues until ${}^{i}\mathbf{M}^{\text{res}}_{j,k}$ and ${}^{i}\mathbf{M}^{\text{tar}}_{j,k}$ match within an acceptable tolerance Δ as well as convergence being reached, which is defined as the case when the modified application pattern does not change over five successive iterations.

9.2.3 Fluid Tracing

In order to execute the fluid reduction according to the previously described criteria, the flow path of every fluid cell needs to be known to determine if and how far it has overflown. Therefore, a tracing function was written which calculates the flow path of a *fluid particle* (i.e. a table of rows with time, $x-$ and $y-$position) by giving the start coordinates and time steps with the corresponding velocity fields as function input. An illustration of the outcome of this tracing function is shown in Figure 9.5 for three successive time steps of a plausible squeeze flow scenario. Within that function the particle flow coordinates of one time step t are calculated according to Equation 9.3:

$$\begin{pmatrix} x_{t+1} \\ y_{t+1} \end{pmatrix} = \begin{pmatrix} x_t \\ y_t \end{pmatrix} + \Delta t_t \cdot \begin{pmatrix} u_t(x_t|y_t) \\ v_t(x_t|y_t) \end{pmatrix} \tag{9.3}$$

Since the velocity field is calculated in a discrete (non-continuous) form by the PFGM simulation, the needed continuity for path tracing was created by bilinear interpolation in-between the surrounding four velocity vectors of the current path position to get the velocities u_t and v_t at the needed position, as indicated by the red plus signs in Figure 9.5. In addition to the flow path, the information of whether the tracked particle is inside or outside of the target bond geometry is listed in a binary form ($1 =$ inside, $0 =$ outside). The total distance of overflow, d_{th}, is then calculated by summing all sub-distances of the rows where the fluid is outside of the target bond geometry. Later, this entire function will be looped with the start coordinates set to the centre of each fluid cell.

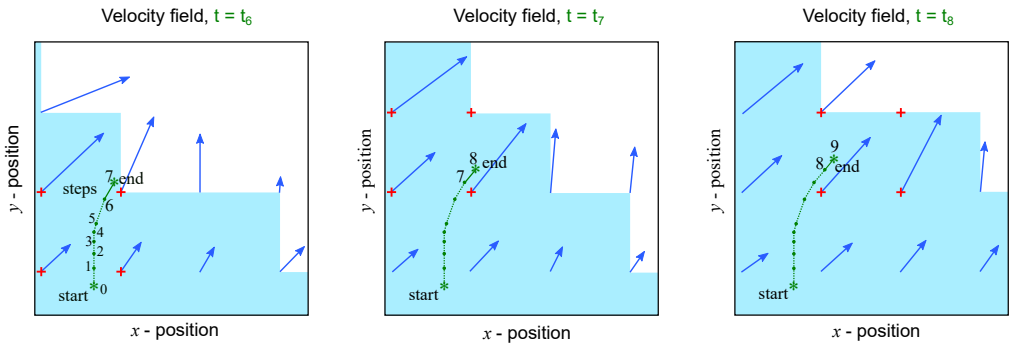

Figure 9.5: Illustration of the fluid tracing function for three consecutive time steps. The blue vectors represent a transient velocity field as it could occur during squeeze flow; cells filled with fluid are shown in light blue; the green dashed line shows the previous flow path of a fluid particle, which start and end position is indicated by the star-dots; in-between, each dot on that line represents the fluid particle position at a previous time step, the continuous line shows the flow path of the current time step. All time steps are labelled with numbers. The red plus signs mark the velocity vectors which contribute to the bi-linear interpolation of the velocity vector for the current respective position of the fluid particle.

9.3 Considered Examples

Subsequently a few examples are presented to demonstrate the optimization possibilities of the developed algorithm to find optimized application patterns for different desired bond shapes. Further, the examples are used to investigate the algorithm in terms of its convergence, different target thicknesses (degree of compression) and the influence of squeeze velocity and flow law. All examples are illustrated in Figure 9.6 and summarized in Table 9.1.

9.3.1 Example #1: Square

The first example addresses the question on how to apply adhesive, so that it spreads into a square form, see Figure 9.6 (left). This problem does not only arise in the context of adhesive bonding, but for example, also on how to apply thermal paste to chips or CPUs, so that it ideally distributes in the gap after mounting a heat sink or cooler. A square fluid distribution with the dimensions of $l_\mathrm{x} \times l_\mathrm{y} = 38 \times 38\,\mathrm{mm}$ is targeted for, which approximately reflect the dimensions of common consumer CPUs. A resulting thickness of $h_\mathrm{fin} = 1.0\,\mathrm{mm}$ is aimed for. The initial gap height is assumed to be $h_0 = 2.0\,\mathrm{mm}$ and the squeeze velocity is set to $w = 0.1\,\mathrm{mm/s}$, thus the squeeze process takes 10 s. For this simulation the Newtonian flow law was considered with a constant viscosity of $\eta_0 = 1744\,\mathrm{Pa \cdot s}$. The initial pattern of the first iteration was chosen the same as the target bond geometry ($\mathbf{M}^\mathrm{ini} = \mathbf{M}^\mathrm{tar}$).

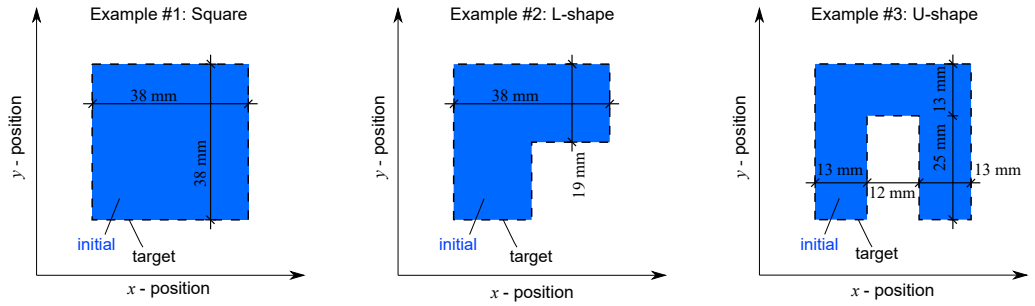

Figure 9.6: Illustration of the optimization examples.

Table 9.1: Parameters of the optimization examples.

			Example #1: Square convergence study			Example #2: L-shape degree of compression				Example #3: U-shape fluid model varied		
Domain												
length, width	L_x, L_y	[mm]	60.6	60.6	60.6	49.4	60.6	85.6	121.1	60.6	60.6	60.6
number of cells	n_x, n_y	[-]	**66**	**132**	**264**	108	132	186	510	132	132	132
fluid cells	f_x, f_y	[-]	40	80	160	80	80	80	160	80	80	80
Squeeze												
velocity	w	[mm/s]	0.1	0.1	0.1	0.1	0.1	0.1	0.1	**0.1**	**0.1**	**1.0**
initial gap	h_0	[mm]	2.0	2.0	2.0	2.0	2.0	2.0	2.0	2.0	2.0	2.0
final gap	h_{fin}	[mm]	1.0	1.0	1.0	**1.5**	**1.0**	**0.5**	**0.25**	1.0	1.0	1.0
Fluid												
model	η	[Pa · s]	Newt.	Newt.	Newt.	Newt.	Newt.	Newt.	Newt.	**Newt.**	**Yas.**	**Yas.**

To determine how many elements are needed for a converging simulation, i.e. the minimum number of elements in x- and y-direction needed to discretize the domain, a convergence study was performed in advance. Therefore, the domain was discretized with 66×66, 132×132 and 264×264 elements and the results were compared in terms of convergence and smoothness of the contour.

9.3.2 Example #2: L-Shape

As a second example, an L-shaped adhesive bond geometry is targeted. The geometric dimensions were the same as in example #1, except that the targeted fluid domain was reduced by one quarter to get the L-shaped bond geometry, see Figure 9.6 (middle). This example is further used to investigate the capability of the developed algorithm to find optimized pattern for different target bond thicknesses (i.e. degree of compression). In total, four different compression scenarios were investigated, which always started with an initial gap height of $h_0 = 2\,\text{mm}$ and then approached $3/4$, $1/2$, $1/4$ and $1/8$ of h_0 (i.e. resulting in target bond thicknesses, h_{fin}, of $1.50\,\text{mm}$, $1.00\,\text{mm}$, $0.50\,\text{mm}$ and $0.25\,\text{mm}$).

The Newtonian flow law is considered, and the initial pattern of the first iteration is set to the target bond geometry ($\mathbf{M}^{\text{ini}} = \mathbf{M}^{\text{tar}}$). Depending on the degree of compression the domain needs to be discretized with more cells to account for the increased squeeze and to keep the number of initially filled fluid cells large enough. Thus, the corresponding discretization was done with 108×108, 132×132, 186×186 and 510×510 cells.

9.3.3 Example #3: U-Shape

The third example targets a U-shaped bond geometry. The initial and target fluid geometry is illustrated in Figure 9.6 (right). This example is also used to investigate the influence of different flow laws on the optimization algorithms results. Besides Newtonian fluid behaviour at a squeeze velocity of $w = 0.10\,\text{mm/s}$ the non-Newtonian flow law according to Yasuda is investigated for two different squeeze velocities $w = 0.10\,\text{mm/s}$ and $w = 1.00\,\text{mm/s}$.

Just like before, the initial pattern of the first iteration is set to the target bond geometry ($\mathbf{M}^{\text{ini}} = \mathbf{M}^{\text{tar}}$). However, the discretization with 132×132 cells is always the same in this example.

9.3.4 Further Examples

In addition to the Square, L-shape and U-shape further application pattern are optimized to flow into the shape of an open circle, a heart shape, a rectangle as well as two arbitrary shapes. These further examples can be found in Appendix A and are not described in detail as they speak for themselves. All these examples were discretized with a domain that consists out of 264×264 cells. The compaction ratio was $4 : 1$ ($h_0 = 2.0\,\text{mm}$ and $h_{\text{fin}} = 0.5\,\text{mm}$) with a squeeze velocity of $w = 0.10\,\text{mm/s}$. In addition, the example of the square shape is shown for the higher degree of compression as well. The Newtonian flow law is considered, and the initial pattern of the first iteration is set to the target bond geometry ($\mathbf{M}^{\text{ini}} = \mathbf{M}^{\text{tar}}$) for all of these examples.

9.4 Optimization Results

One quick note before diving into the results. Additional video sequences of the results that follow are linked in the corresponding figure captions. They can also be accessed by clicking on this link or by scanning the QR-Code in the Appendix.

9.4.1 Example #1: Square

The optimization algorithm starts by reducing material at the four edges of the initial square application pattern, leaving the corners intact, see Figure 9.7 (left) at iteration step $i = 5$ and $i = 11$. In the subsequent iteration process, each of the originally straight edges develops into a bay-shaped contour and the pattern results in a form which reminds of the shape of the diamond suit of playing cards, see Figure 9.7 (left) at iteration step $i = 20$ and $i = 35$. Beyond iteration $i = 35$ no more changes are noticeable within the next five iterations, thus the algorithm has converged, and the pattern is now optimized.

At the beginning of the optimization process, i.e. at iteration step $i = 5$ and $i = 11$, the resulting distribution (in which the corresponding initial pattern flows into), shown in Figure 9.7 (middle), looks like a square contour, but with very rounded corners and slightly curved edges. Later in the iteration process, the contour refines and at $i = 20$ the square shape of the resulting pattern becomes more visible, but it still has rounded corners. Finally, at iteration step $i = 35$, a close to perfect square shape is approached after the squeeze process of the corresponding initial pattern.

The difference between the target pattern (the ideal square shape) and the current resulting distribution (gained by the algorithm) are shown in Figure 9.7 (right). It is distinguished between overfilling (purple) and underfilling (pink) in relation to the target geometry. In this example, there is a high degree of overfilling which gets minimized during the iteration until only a slight overfilling at the edges of the square shape is present, see Figure 9.7 (right). The targeted bond shape consists of approximately $26{,}200$ cells that need to be filled only. Yet approximately $47{,}500$ cells are filled at $i = 5$ (+81%), $40{,}600$ cells are filled at $i = 11$ (+55%), $32{,}700$ cells are filled at $i = 20$ (+25%) and $26,900$ cells are filled at $i = 35$ (+3%). The number of both, over- and underfilled, cells can be seen as a measurement of residual optimization error.

The squeeze flow process itself is illustrated and compared in Figure 9.8 before and after optimization with the developed algorithm. It can be seen that the optimized pattern flows into the desired square shape, while the non-optimized pattern flows into a circular shape.

The convergence study shows that the number of iterations needed to optimize the square pattern is approximately 35, no matter if the domain is discretized with 66×66, 132×132 or 264×264 cells, see Figure 9.9. Furthermore, all of the optimized application pattern look approximately the same regardless of the number of cells used for discretization Figure 9.10, thus the algorithm is mesh-independent.

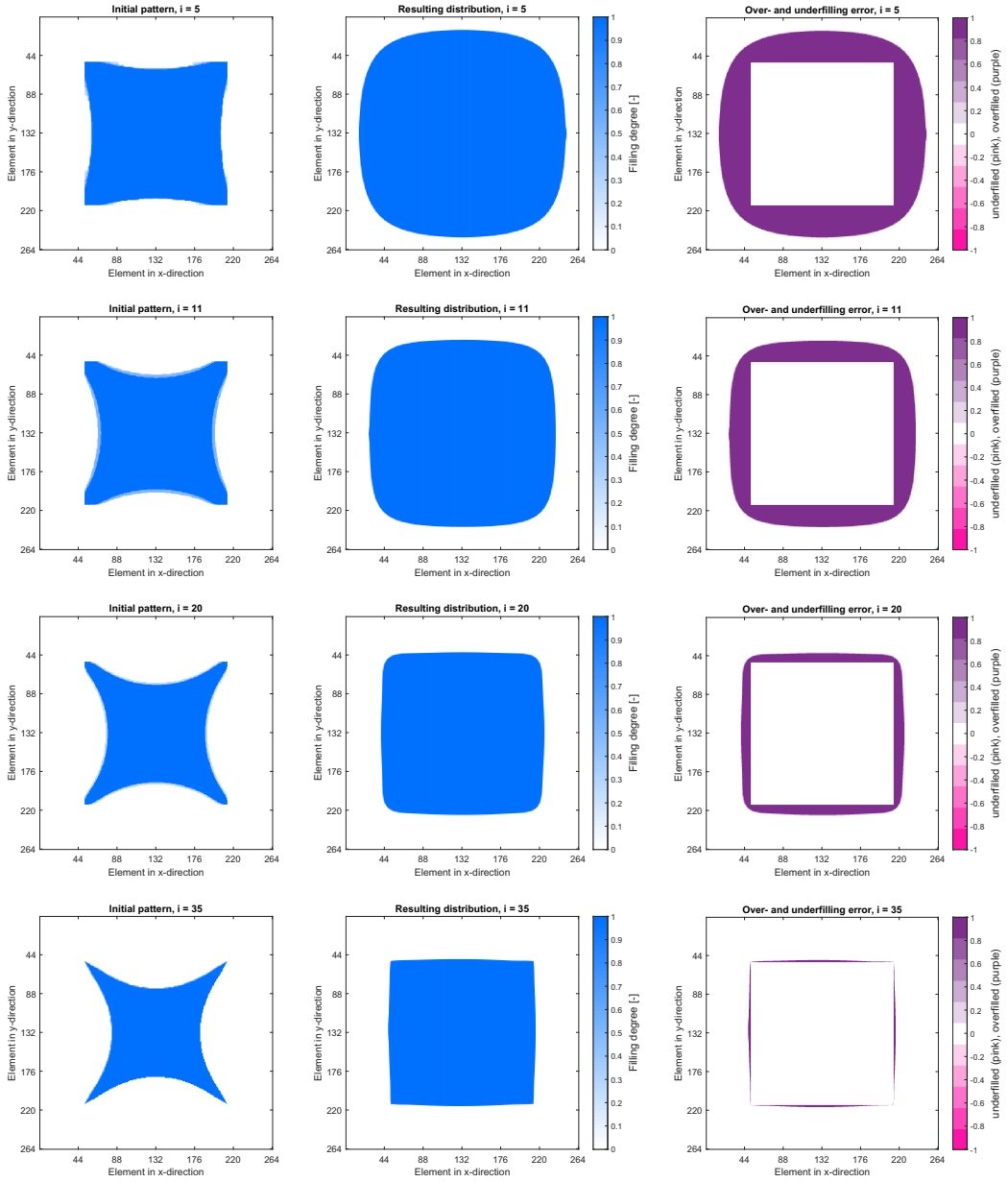

Figure 9.7: Process to find an optimized initial pattern to be squeezed into a square bond: iterative development of initial pattern (left), resulting distribution (middle) and difference between resulting and target distribution (right).

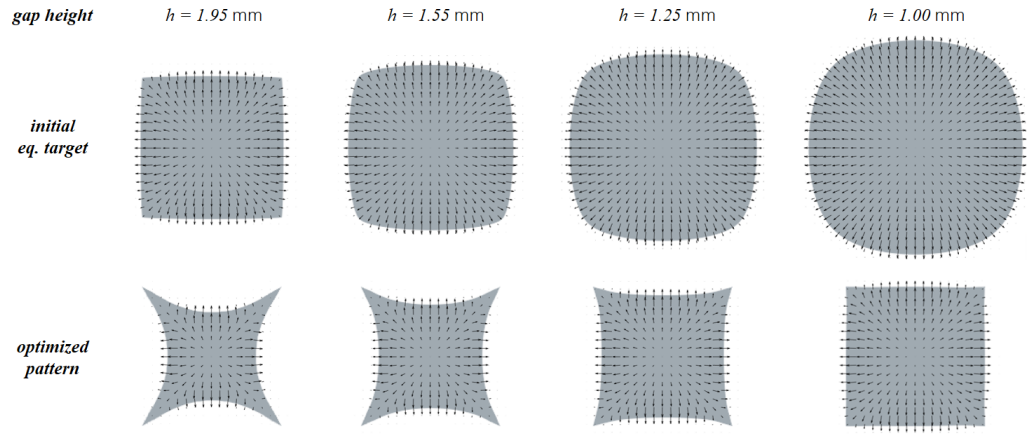

Figure 9.8: Comparison of the fluids squeeze flow process before (top) and after (bottom) optimization.

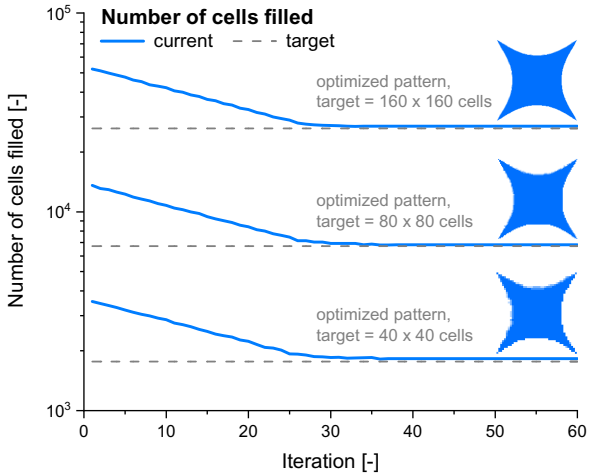

Figure 9.9: Convergence study.

9.4.2 Example #2: L-Shape

Just like with the square shape, the optimization algorithm starts by reducing material at the edges (or borders) of the initial square application pattern, not touching the corners at the beginning, see Figure 9.11 (left) at iteration step $i = 5$ and $i = 11$. Subsequently, each of the originally straight edges develops into a bay-shaped contour, see Figure 9.11 (left) at iteration step $i = 21$ and $i = 39$. Beyond iteration $i = 39$ no more changes are noticeable, thus the algorithm has converged, and the pattern is optimized.

At iteration step $i = 5$ and $i = 11$, the resulting distribution (in which the corresponding initial pattern flows into), shown in Figure 9.11 (middle), does not look like an L-shape and

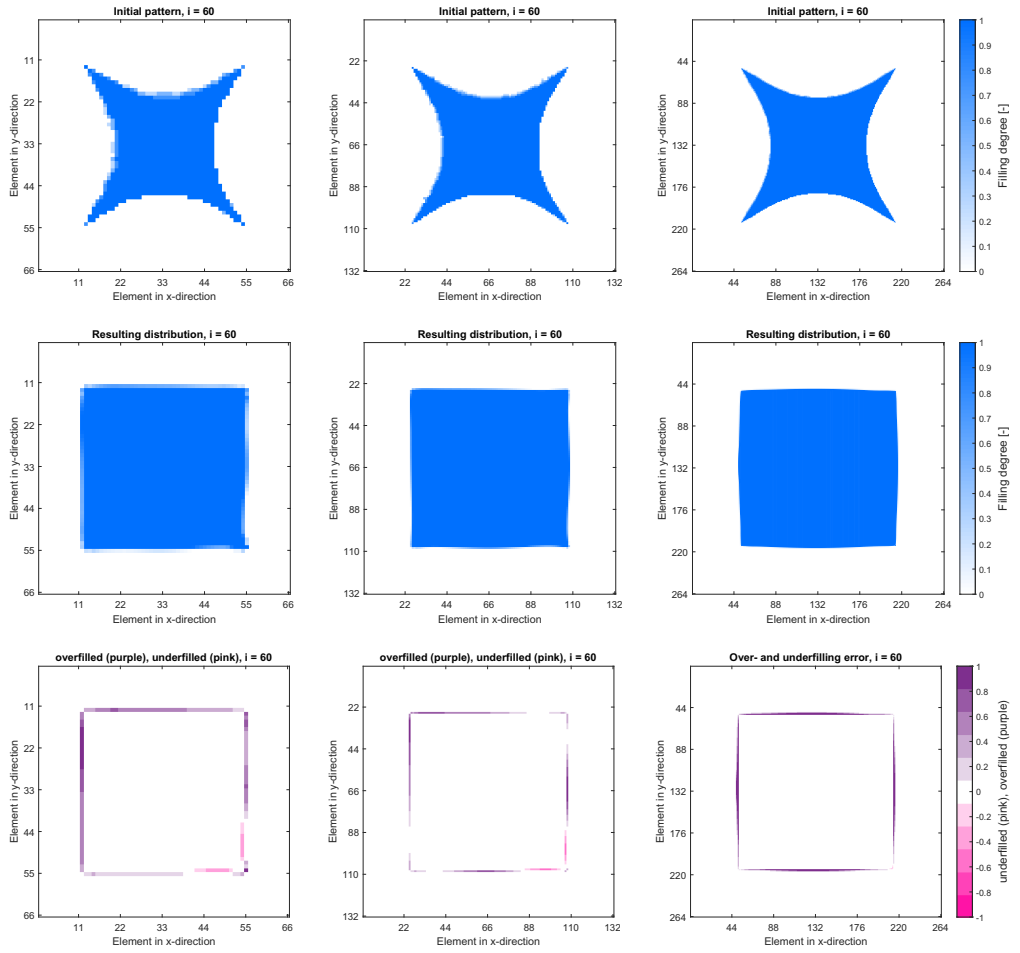

Figure 9.10: Convergence study: initial pattern (top), resulting distribution (middle) and over- and underfilling (bottom) for three different degrees of discretization, i.e. 66×66 cells (left), 132×132 cells (middle) and 264×264 cells (right).

has very rounded corners and curved edges. Later in the iteration process, the contour refines and at $i = 21$ the L-shape of the resulting pattern becomes more visible, but it still has rounded corners. At iteration step $i = 39$, a close to perfect L-shape is approached. Only the inner corner of the L-shape remains slightly rounded and overfilled.

The difference between the target pattern and the resulting distribution are shown in Figure 9.11 (right). In this example, there is a high degree of overfilling which gets minimized during the optimization process until only a slight overfilling at the inner corner of the L-shape is present, see Figure 9.11 (right) at $i = 39$.

Furthermore, the target thickness was varied with the example of the L-shape and the results are shown in Figure 9.12. With a low degree of compression (i.e. squeeze from $h_0 =$

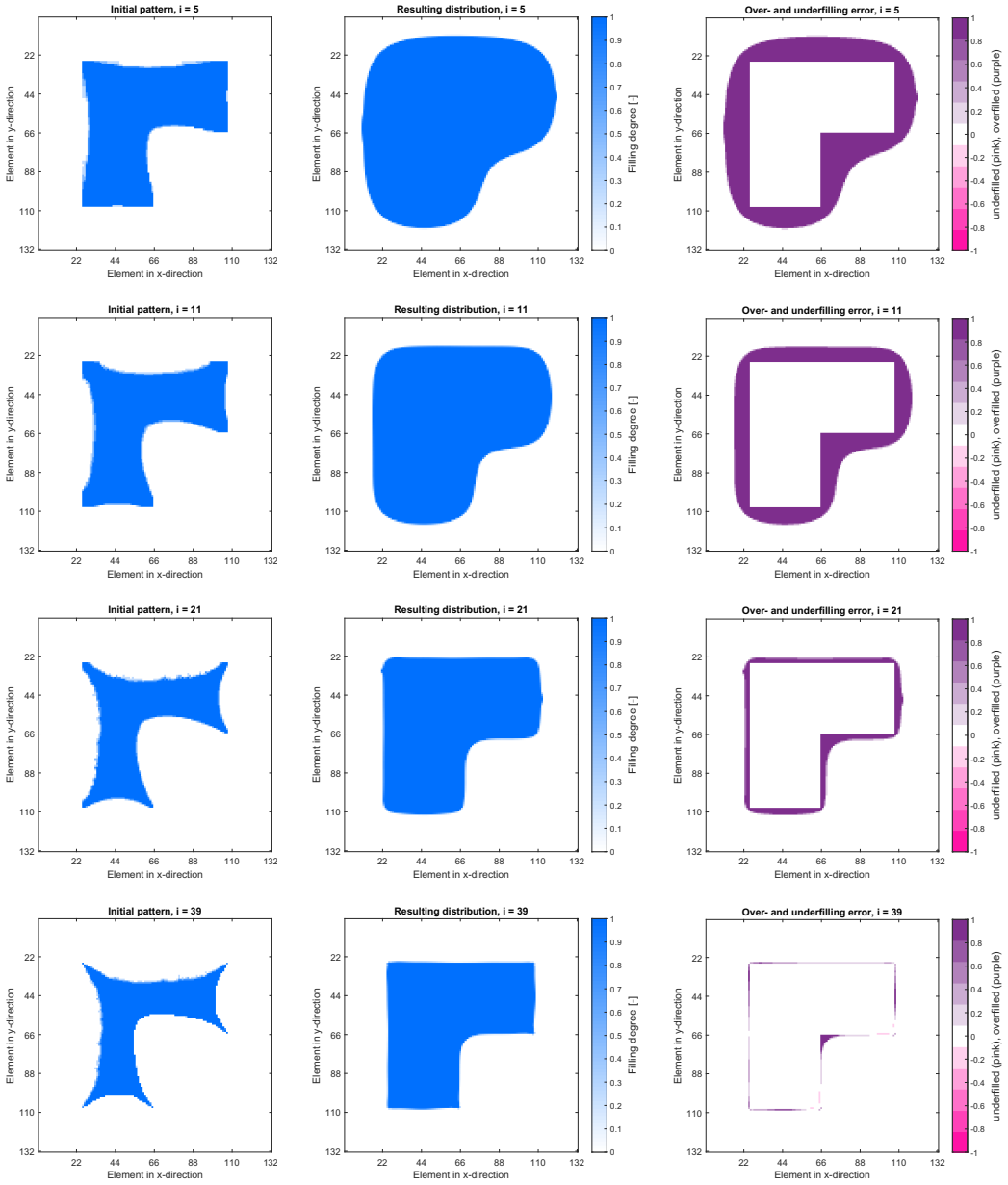

Figure 9.11: Process to find an optimized initial pattern for a L-shaped bond with $h_{\text{fin}} = 0.5 \cdot h_0$: iterative development of initial pattern (left), resulting distribution (middle) and difference between resulting and target distribution (right).

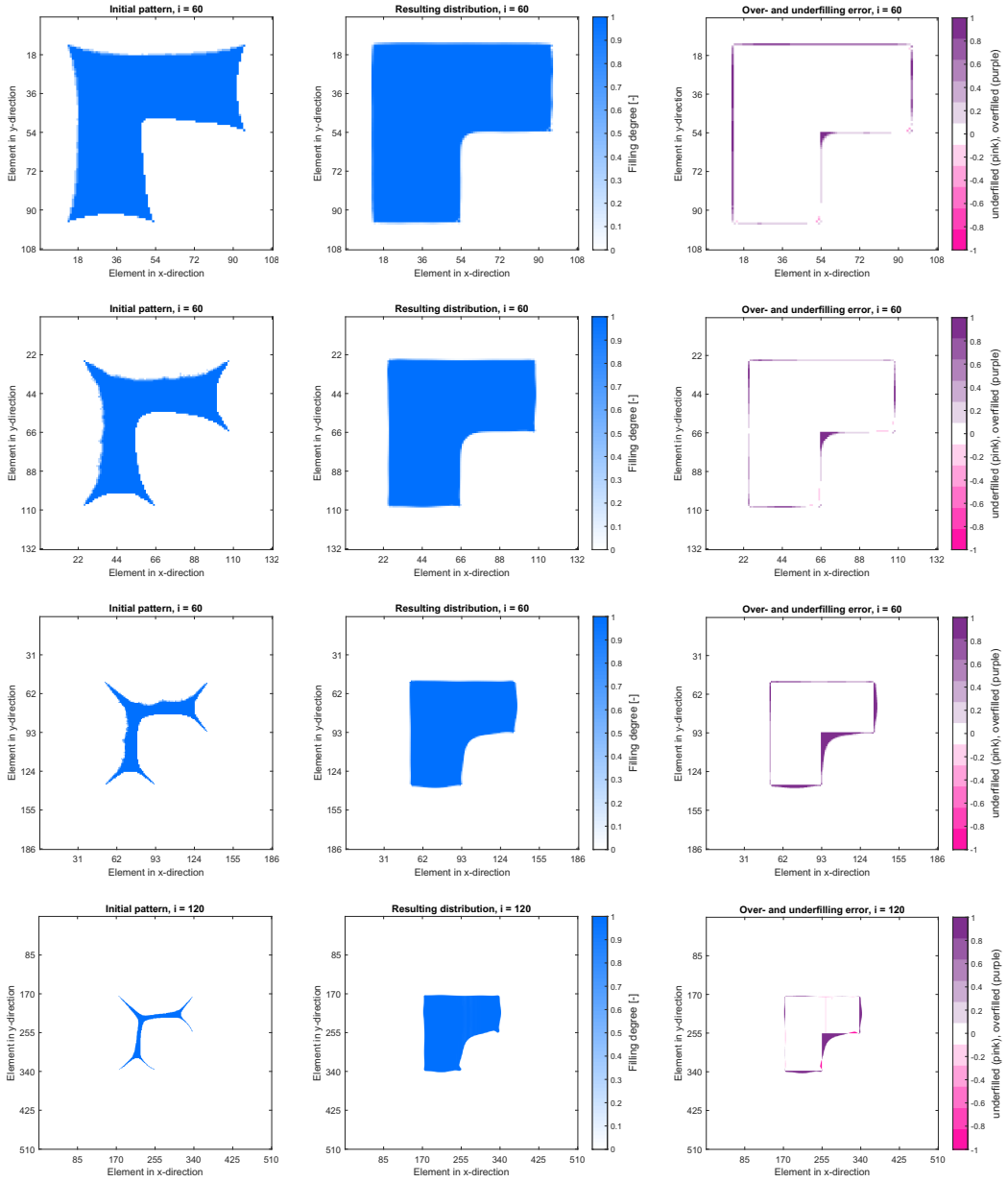

Figure 9.12: Optimization of L-shape with varied degree of compression: $h_0/h_{\text{fin}} = 2.0/1.5$, $2.0/1.0$, $2.0/0.5$ and $2.0/0.25$ mm (from top to bottom); initial pattern (left), resulting distribution (middle) and over- and underfilling (right).

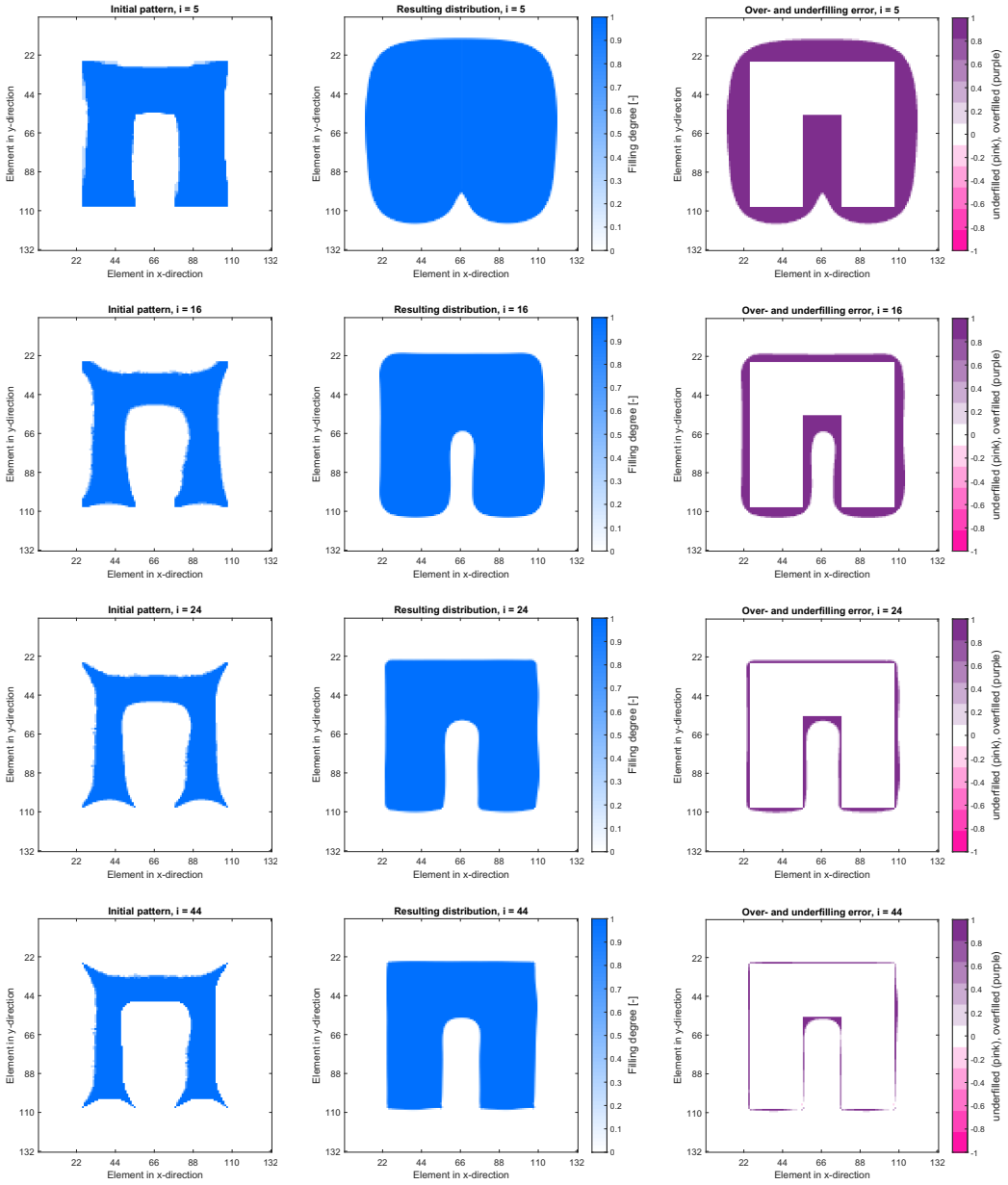

Figure 9.13: Process to find an optimized initial pattern to be squeezed into a U-shaped bond: iterative development of initial pattern (left), resulting distribution (middle) and difference between resulting and target distribution (right).

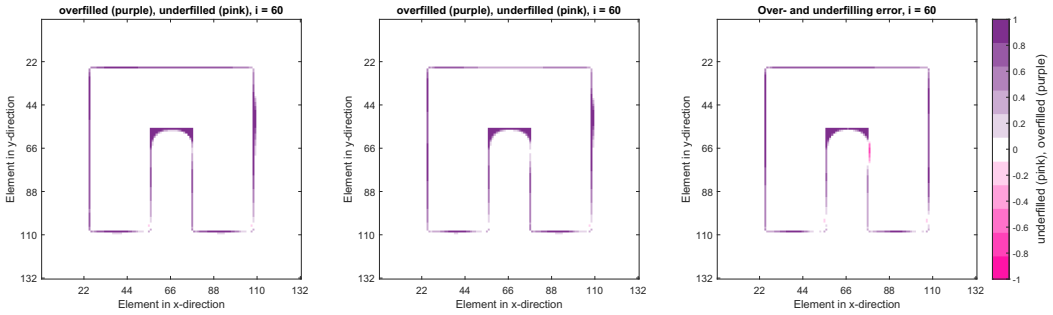

Figure 9.14: Over- and underfilling of the optimized U-pattern with varied flow law and squeeze velocity: Newtonian with $w = 0.10\,\mathrm{mm/s}$ (left), Yasuda-Law with $w = 0.10\,\mathrm{mm/s}$ (middle), Yasuda-Law with $w = 1.00\,\mathrm{mm/s}$ (right).

2.0 mm to $h_{\mathrm{fin}} = 1.5$ mm or $h_{\mathrm{fin}} = 1.0$ mm) the algorithm finds a pattern which almost perfectly flows into the desired L-shape. However, at thinner target bond thicknesses ($h_{\mathrm{fin}} = 0.50$ mm or $h_{\mathrm{fin}} = 0.25$ mm) the amount of over- and underfilled cells of the corresponding optimized pattern increases. If the degree of compression is higher the optimized initial application pattern gets slimmer and very pointy structures form towards the corners.

9.4.3 Example #3: U-Shape

The way the initial application pattern adapts during optimization also follows the same *rules* as previously observed. Fluid material is gradually removed at the edges and a bay-like contour is formed, while the outer corners form into a spike like shape, as shown in Figure 9.13 (left). The resulting distribution, in which the initial pattern flows into is shown in Figure 9.13 (middle). Between iteration $i = 5$ and $i = 16$ the indentation of the targeted U-shape forms and becomes wider at $i = 24$. The algorithm has converged at $i = 44$ and the optimized initial pattern almost perfectly flows into the target shape, apart from the two inner corners were only a round contour evolved. The evolution of the over- and underfilling error is shown in Figure 9.13 (right).

In addition, in this example, the fluid flow law was varied (Newtonian and Yasuda-law) as well as the squeeze velocity (0.10 mm/s and 1.00 mm/s) to investigate its influence on the optimization result. It was found that the optimized initial pattern as well as its resulting distribution are not influenced by these factors, since there are no significant differences in the final fluid distributions, as shown in Figure 9.14.

9.4.4 Further Examples

The results of the further examples which include the optimization of application pattern, which should flow into an open circle, a heart shape, a rectangle as well as two arbitrary shapes, are shown in Appendix A.

10 Experimental Validation of the Optimization Procedure

The objective of this chapter is to experimentally validate the developed optimization algorithm. Therefore, optimized pattern will be experimentally investigated in the HSC to compare the resulting fluid distributions of the experiment with the simulation — and show whether or not the numerically optimised application pattern will actually flow into the desired shape in reality.

10.1 Validation Methodology

The goal of validation is to show that the optimised pattern will flow into the desired bond geometry in a real experiment. To do so, some of the previously shown optimized pattern are applied onto a plane surface and are investigated within the adapted HSC. At this point in should be noted that these investigations can be seen as an addition to the validation of the PFGM software performed in Part II. However, this verification is needed to allow statements about the optimization quality as well as feasibility and applicability in practical applications. It should also demonstrate that the optimized shapes, which in some cases became quite filigree, can be applied with reasonable accuracy for manufacturing.

10.1.1 Considered Examples

Four different examples of optimized application pattern are considered to validate the developed algorithm: the square shape, L-shape, Heart as well as the Arbitrary form. These patterns are chosen because they include various shapes and thus many flow possibilities are covered. In detail, target shapes with in- and outside corners and straight edges (i.e. square and L-shape) as well as a pattern with steady curved contours (i.e. heart shape) and an arbitrary shape that combines all of the previous characteristics, are investigated. These quite different patterns are considered to verify the algorithm's ability to optimize application pattern as general as possible. Furthermore, it should demonstrate that any target geometries are possible to optimize initial pattern for. The patterns are scaled to fit into

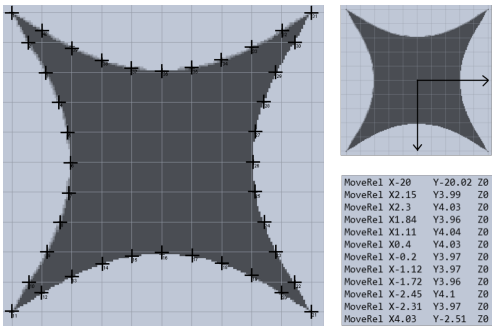

(a) Creation of the application path code

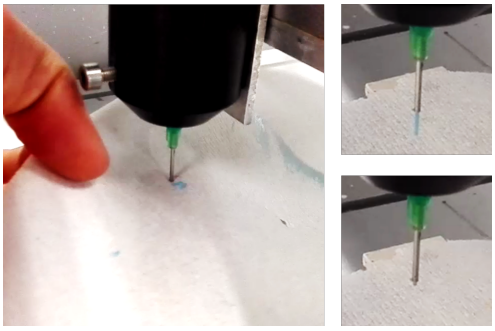

(b) Preparation of the dispenser nozzle

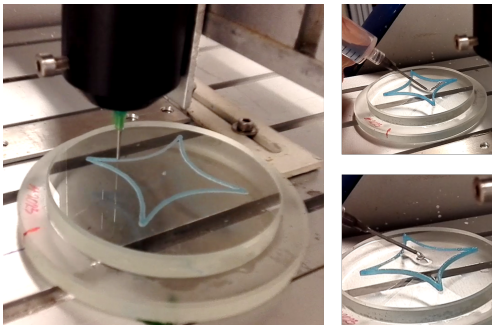

(c) Application of the optimized bi-pattern

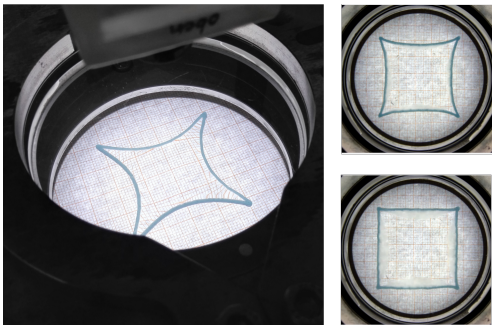

(d) Squeeze flow experiment in the HSC

Figure 10.1: Procedure how to apply optimized pattern for the experimental validation.

a box of approximately $4\,\text{cm} \times 4\,\text{cm}$. The degree of compression is chosen as $4 : 1$ with $h_0 = 1.00\,\text{mm}$ and $h_{\text{fin}} = 0.25\,\text{mm}$, while the squeeze velocity is $w = 0.2\,\text{mm/s}$. Each experiment was repeated three times.

10.1.2 Adhesive Application

The challenge in dispensing the optimized patterns is to apply the very filigree and pointy shapes as precisely as possible. For the application, the *dam* & *fill* method, cf. subsection 2.2.3, was used because it is quite easy to implement in practice.

First, the contour of the application pattern was defined as an application path by taking coordinates at regular intervals (using a polygon line), as shown in Figure 10.1 (a). Then, this path was applied using a dispenser linked to a xyz-Table, shown in Figure 10.1 (b). Therefore, a highly thixotropic (stable) fluid, i.e. technical Vaseline (dyed blue) was used. The dispenser's pressure to apply the dam was set to $p = 1.05\,\text{bar}$ and a nozzle velocity of $v = 5.0\,\text{mm/s}$ was used. To obtain an initial pattern height of $h_0 = 1.0\,\text{mm}$, three layers were applied on top of each other to form the dam, see Figure 10.1 (c).

Subsequently, a syringe filled with a low viscous (flowable) fluid, i.e. a silicone oil of the same type as previously, but with a lower viscosity of $\eta = 10\,\mathrm{Pa}\cdot\mathrm{s}$ (*Elbesil B 10.000*), was used to manually fill the dam. Finally, the pattern is positioned and squeezed within the modified HSC, as shown in Figure 10.1 (d).

10.2 Validation Results

All of the video sequences of the results that will follow are linked in the corresponding figure captions. They can also be accessed by clicking on this link or by scanning the QR-Code in the Appendix.

The application of the optimized patterns using the *dam* & *fill* method worked with very good accuracy. Except from the spiky tips, which could not be realised as pointy as in the simulation, the applied patterns look exactly like the model optimized them, see Figure 10.2. However, the L-shape was slightly modified at the inside corner by purpose, to improve the fluid distribution after the squeeze process in that area, as the algorithm struggled to minimize spill out at that particular spot.

The corresponding resulting distributions in which the four patterns flow into according to the simulation and experiment are shown side by side in Figure 10.3. Without further quantification, it can be seen that the patterns that are squeezed in the HSC match very well to the squeeze flow simulation as well as to the target bond geometries. Especially the example of the square shape demonstrates the benefit of the proposed optimization methodology. The edges are very straight where they should be, however the corners are slightly rounded where a sharp 90° angle was desired.

Same for the L-shape, where the manual modification resulted in an almost perfect inside corner and thus a very nice agreement with the target bond geometry. To the eye, the heart shape looks perfect, with no noticeable deviation between the resulting distribution and the target bond geometry. And even the arbitrary form, with its many features, came out very good. However, the corners are slightly rounded compared to the pointy edges of the target shape. These rounded edges are caused by the imperfect application of the spiky tips in the initial patterns.

10.3 Technical Application Example

This section finishes the chapter with an exciting demonstration example. The chosen example involves a CPU on which a square cooling paste pattern is should be applied. One further requirement is that the application process should be very fast to gain a high number

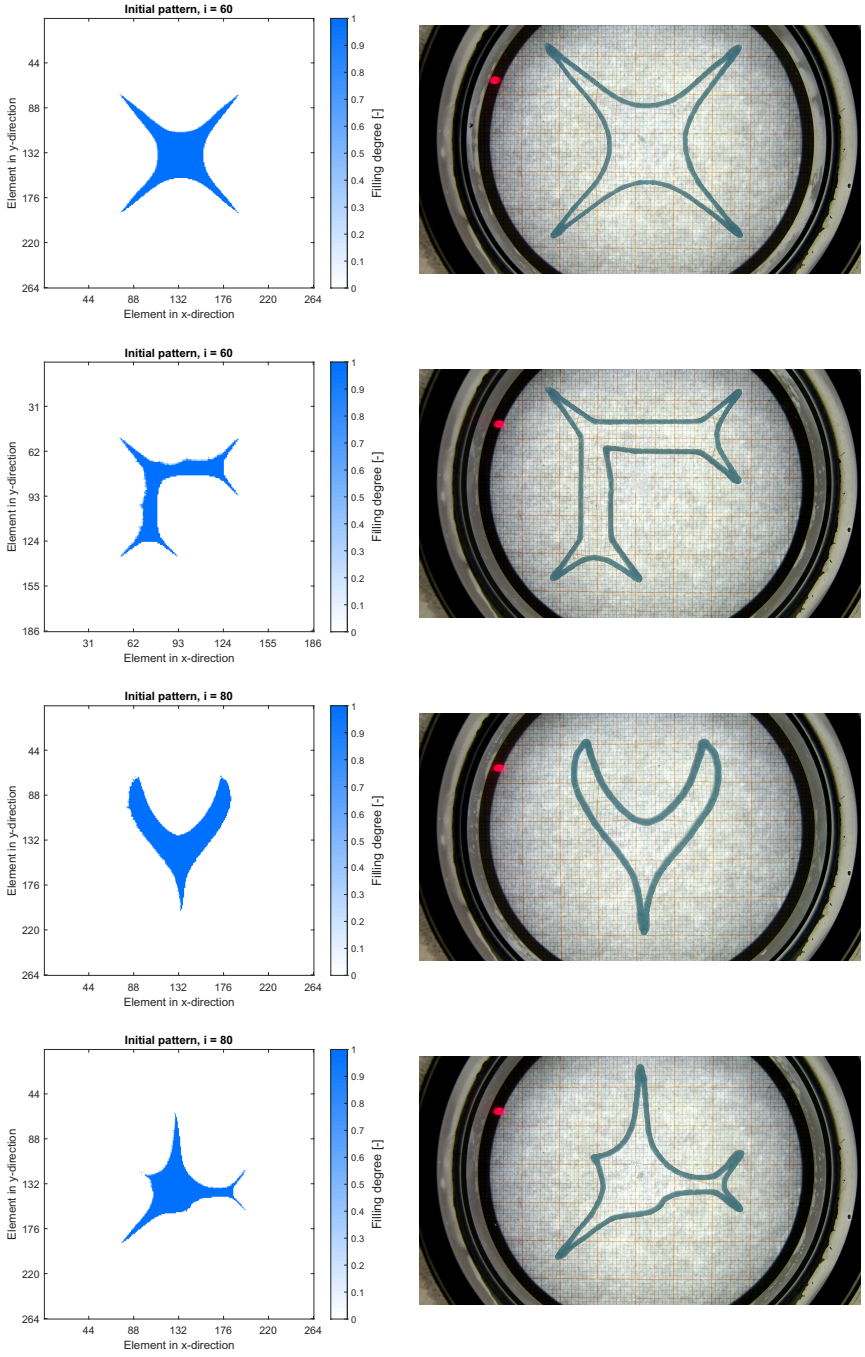

Figure 10.2: Four optimized application pattern before squeezing: numerical simulation result (left), real initial application pattern (right). Note that the inner fluid is transparent. Watch the full videos here.

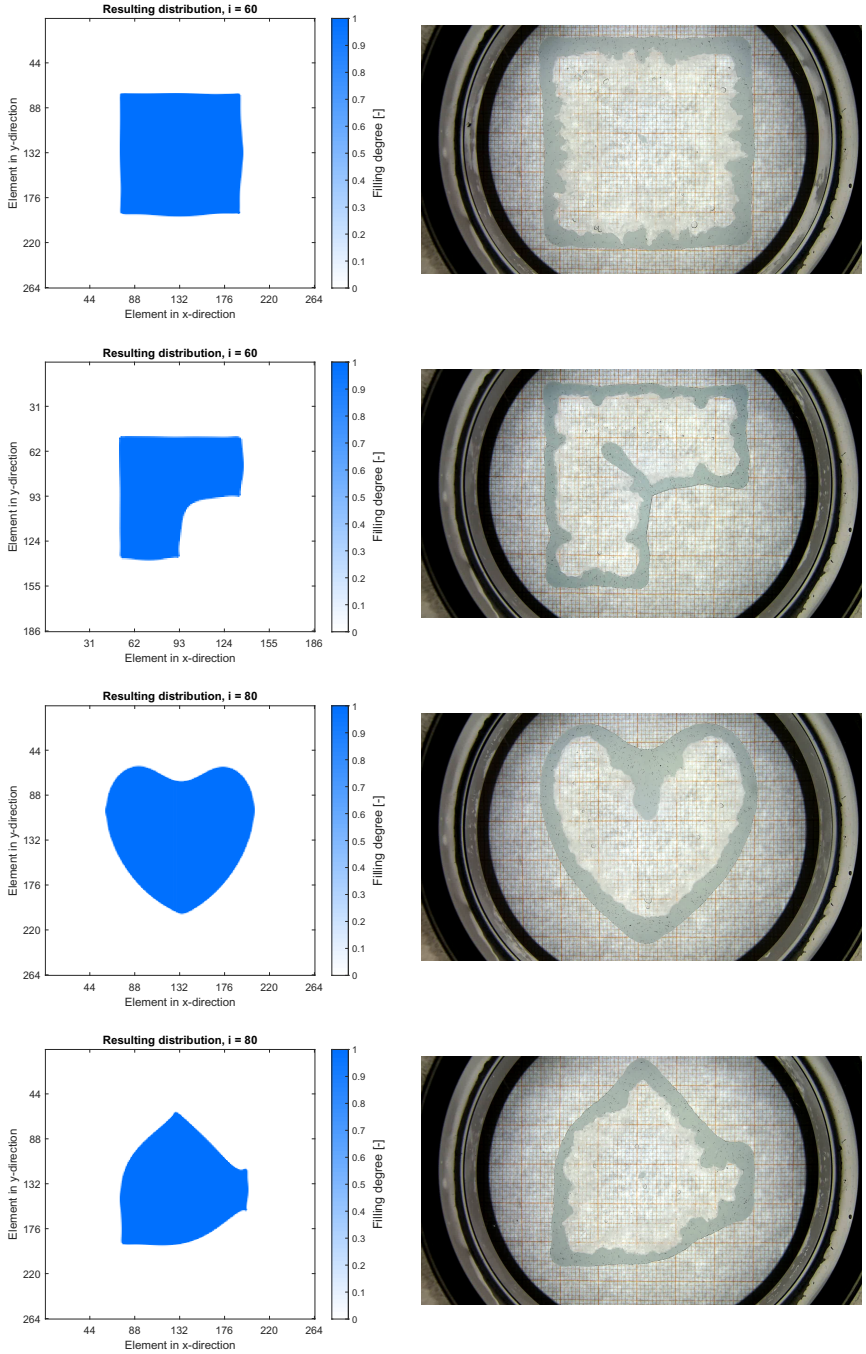

Figure 10.3: Corresponding resulting distributions after squeezing: numerical simulation result (left), real resulting fluid distribution (right). Note that the inner fluid is transparent. Watch the full videos here.

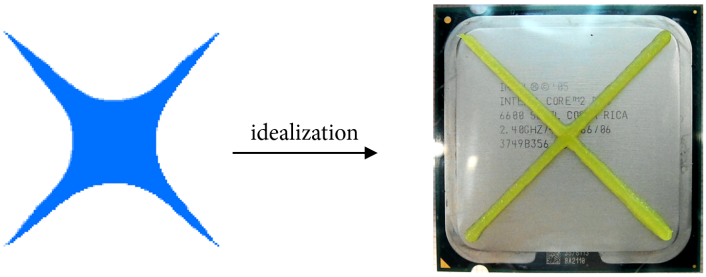

Figure 10.4: Simplification of the optimized star shaped application pattern into a simple X-pattern for easy cooling paste application on a CPU.

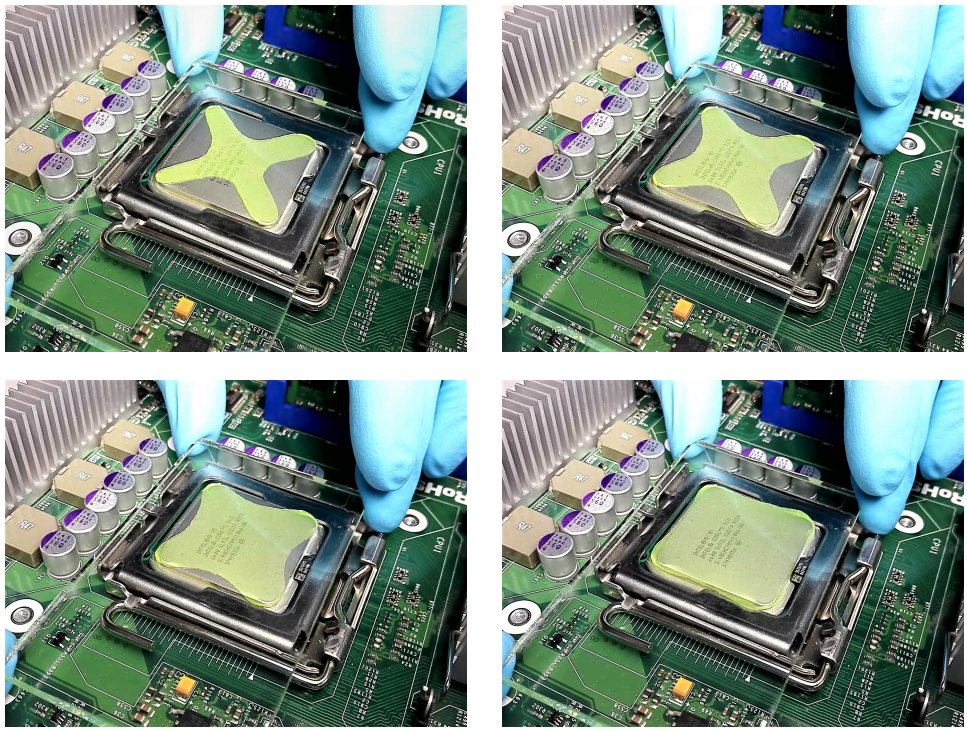

Figure 10.5: Corresponding squeeze flow process of an simplified optimized X-pattern for a square CPU cooling paste target geometry.

of production cycles. To achieve this, the optimized initial pattern, as obtained in subsection 9.4.1, serves as a baseline. It is then simplified into two crossing beads to enable an easy and fast application process, as illustrated in Figure 10.4.

The simplified X-pattern is carefully squeezed until the entire geometry is completely filled with cooling paste, as depicted in Figure 10.5. It is evident from the figure that the paste flows into the desired shape with a satisfactory level of precision, despite the fact that

the originally optimized star-like pattern has been simplified to a strict X-shape. This approach, compared to the application of circular drops, significantly reduces the consumption of expensive cooling paste material.

While there are numerous other industrial examples to consider, this simple yet effective approach, which includes an idealization step, demonstrates the wide applicability of the developed optimization methodology for industrial routines.

Part IV

Closing Chapters: Scientific Impact, Technical Benefit and Final Words

11 Summary

This thesis proposed a methodology to optimize the application pattern of adhesively bonded joints, so that the liquid adhesive automatically flows into the desired bond shape during manufacturing — leaving no spots over- or underfilled, thus the adhesive is used in the most efficient way. Besides preventing adhesive excess and waste that eliminates the need for cleaning and reworking steps after joining, this optimization approach ultimately led to a more ecological and economic adhesive manufacturing processes.

To achieve this goal, an optimization algorithm was developed that iteratively modifies the shape of adhesive application pattern until it flows into the desired bond shape. Established methods from topology optimisation for solids were used, re-interpreted, and applied in the context of fluid mechanics in a new way. At each iteration, the resulting distribution obtained after squeezing an initial adhesive application pattern is calculated. The *resulting* distribution is then compared to the *desired* adhesive distribution, and the overflown adhesive is traced back to its origin in the initial pattern (using the calculated velocity and direction). These overflown areas were then removed from the initial pattern and the iteration loop continued until the resulting distribution matches the desired bond geometry within an acceptable tolerance.

This optimization strategy relied on the accurate simulation of squeeze flow processes for which a special numerical model was chosen. This model was extensively validated in a comprehensive experimental study in advance, to prove its suitability. By combining the Hele-Shaw Approach, a method to investigate squeeze flow processes, with Particle Image Velocimetry, a method to measure fluid flows, it has been demonstrated that the simulation model is sufficiently accurate and can be implemented to calculate the quantities that were required by the optimization algorithm. Further, the surface structure has proven to be of secondary importance and doesn't need to be considered in the optimization.

The algorithm was applied to optimize a variety of different application patterns. It was found that the optimized shapes have recurring features such as pointy fingers which reach to the corners and merge into bays that flow into straight edges. Furthermore, quantities like the degree of compression, number of cells and considered flow-laws were varied to investigate their influence on the algorithms results. However, it was found that the algorithm

is mesh and flow-law independent, which highly improves its applicability and simplicity for practical use. It is capable to identify optimal patterns for frequently used adhesive layer thicknesses and degrees of compression.

Finally, the optimized patterns obtained through theoretical analysis were validated in real-world experiments, that confirmed their ability to flow into the desired shapes. Overall, this thesis presents an innovative approach to optimize adhesive application patterns. Due to the performed optimization, the environmentally questionable adhesive waste and costly post-cleaning work can be eliminated — thus, a more ecological and economical manufacturing process is achieved.

11.1 Discussion

The results demonstrate the algorithms capability to optimize adhesive application pattern so that the fluid flows into any desired bond shape with reasonable accuracy for industrial applications. The manufacturing of adhesively bonded joints can be improved by a high degree due to this novel method, e.g. minimizing over- and underfilling and thus highly increasing the efficient use of adhesive material. This new technique is a great example to be implemented to utilize modern manufacturing techniques in terms of automated application.

11.1.1 Gained Advantages

Besides the main advantage of the presented optimization method, i.e. its capability to optimize adhesive application pattern, the algorithm only needs a very limited amount of input data to work. This study showed that the only parameters needed to optimize any adhesive application pattern are:

1. the targeted bond geometry ($\mathbf{M}^{\text{tar}}$) and
2. the degree of compression (h_0/h_{fin}).

No information about the fluid behaviour (fluid model) and squeeze velocity (w) are needed since these factors have almost no influence on the optimization result, cf. subsection 9.4.3. The methodology is very simple to work with and no complex experimental adhesive characterization is needed in advance. An always working guess for the initial pattern is to set it equal to the target bond geometry, as done in every example in this thesis. However, it is also possible to start with any other guess, provided that this initial pattern, in the first iteration, will flow beyond the limits of the intended bond geometry after pressing.

Furthermore, the algorithm has proven to be mesh independent, cf. subsection 9.4.1 and a discretization of about 132×132 cells already gives a good approximation of the fluid shape. At this resolution, calculation times of a few hours are needed to optimize one pattern — which might be improved, but for the sake of this study were fast enough, especially for an algorithm which iterates over a transient fluid flow simulation.

11.1.2 Current Limitations

In the current form, the optimization quality (in terms of areas remained over- or under-filled) decreases with pattern that are pressed into a very thin adhesive layer. In detail, the algorithm struggles to find well suited patterns for degrees of compression higher than $h_0/h_{\text{fin}} > 10$ — which for example are present in hybrid joints [18].

Furthermore, the computation time increases if a high degree of compression is opted for. This has multiple reasons: firstly, the time steps of the transient squeeze flow simulation need to be smaller here, because small changes in gap height, result in large changes in the state variables (pressure, velocity, etc.) which need to converge before the next time step. In addition, a finer discretization using more fluid cells is needed to adequately approximate these optimized patterns, since they get very filigree with higher degrees of compression.

Furthermore, the algorithm struggles to get the fluid distribution perfect in inside corners (see L-shape and U-shape). In contrast to the outer corners, there is always a slight rounding or fillet at the inner corners after squeezing the optimized fluid pattern. Due to the choice of a unidirectional algorithm, fluid can only be removed, thus once a cell within the targeted domain remains unfilled, it cannot be corrected.

11.1.3 Possible Improvements

To overcome these limitations the following improvements and approaches are discussed. This new optimization technique might be extended to a bi-directional algorithm, where fluid can not only be removed, but it can also be added if needed. A suitable criterion would aim to add fluid to the initial pattern in locations which remain unfilled after the squeeze process — thus following the same logic of the fluid removal, which is performed for locations which overflow. For mechanical optimization problems, the extension to bi-directional algorithms (which was done by Querin et al. [74]) was a decisive development to improve convergence and efficiency.

Apart from making the algorithm bi-directional, the computation time can be further shortened by implementing a dynamic rejection ratio (RR) and elimination rate (ER). Both, the RR and ER can be higher at the beginning of the iteration process to quickly find an

approximate optimized shape. But at the end of the optimization process, they need to be smaller to prevent fluid from being removed in places where it is actually needed. Such strategies using dynamic optimization parameters were already successfully implemented in algorithms for mechanical optimization problems. For example, Lin et al. [55] have improved the convergence speed by implementing dynamic optimization parameters which follow a sigmoid function. Last but not least, an improved guess of the initial application pattern will further decrease the computational time of the developed algorithm.

11.1.4 Experimental Validation

Overall, the experimental validation was a success and proved the validity of the developed optimization method in the real world. The agreement between simulation and experiment in terms of the initial and resulting fluid distribution was very good across all patterns. It was not trivial how to apply the actual shapes that have resulted from the optimization, because of their filigree and pointy character. However, using the *dam* & *fill* method these patterns could be applied with reasonable balance of accuracy vs. effort and thus demonstrated one option on how to implement the technique in adhesive manufacturing industry.

During the experiments, it became evident that particular emphasis should be placed on the adhesive layer thickness of the initial pattern. If the actual height of the applied fluid pattern does not match to the theoretical initial and target gap size it was optimized for, spill-out or underfilling will occur. That said, special attention needs to be paid on tolerances. It seems very challenging, maybe even impracticable, to gain good results with the proposed optimization method if the tolerances of the substrates or the joining process become too large. This is the case for very thin, elastic, soft structures with large dimensions, i.e. for structures with a high ratio of slenderness, e.g. as in the case of bonding rotor blades for wind turbines.

On the other hand, the proposed optimization method, performs very well at smaller scales. Using this method, a huge benefit can be gained if a high volume of production is aimed for. It can also be technically applied in other fields than bonding, e.g. to obtain a square cooling paste pattern for a CPU, as demonstrated in section 10.3. Furthermore, the method can be used to inspire the application shape with manual application by hand.

12 Conclusions

Based on the numerical examples presented in chapter 9 and the experimental validation performed in chapter 10 the scientific goal of the thesis, which was defined in the Objectives section as follows:

> **Scientific goal:** The goal of this thesis is to develop an optimization methodology which finds adhesive application pattern that flow into the desired bond geometry during the joining process and thus *reduce adhesive spill-out and underfilling*.

has been achieved!

Several different application patterns which should flow into square, L-, U-, rectangular-, circular-, heart- as well as arbitrary and odd shaped bond geometries were optimized with the developed algorithm. These examples have shown that the developed algorithm is capable to find optimal initial application patterns that flow into the desired bond shapes during the joining process. Combined, these examples should have covered all of the relevant flow phenomena which can occur during adhesive bonding squeeze flow processes. That said, the first subgoal

> **Subgoal #1:** The algorithm is supposed to find an optimal application pattern that flows into *any desired adhesive layer* geometry and thickness.

has been accomplished! — At least for practical relevant bond geometries and adhesive layer thicknesses. However, the target thickness, or degree of compression, was varied with some examples and it was found that the optimization quality (in terms of areas remained over- or underfilled) decreases with a higher degree of compression. It should also be mentioned that there might be a theoretical or academic example for a target bond geometry which the algorithm might fail to optimize an initial pattern for.

Furthermore, a convergence study was performed, which proved the algorithm to be mesh independent. In addition, it was found that the fluid's viscosity and flow law have almost no influence on the optimization result. Thus, the only two information needed for optimization are the desired (targeted) bond geometry and the degree of compression, which means that the second subgoal

> **Subgoal #2:** The algorithm should use a *minimal number of input parameters* to ensure a straightforward utilization in practical applications. ✓

has been achieved! — Which makes this method very easy to use and implement into the industrial practice. No complex adhesive characterization is needed in advance. However, manufacturing tolerances must be considered.

Last but not least, the experimental validation has proven that the optimized adhesive application pattern can be applied in the real world, e.g. by using the *dam* & *fill* method, and that they actually flow into the desired bond geometries. This means that the third subgoal

> **Subgoal #3:** The application patterns optimized by the algorithm should be *applicable and producible in reality* using common manufacturing methods. ✓

has also been reached! — Minimizing obstacles for the implementation into industrial routines and practices. With some tweaking, common and existing techniques, such as simple bead application, can be used to apply the optimized adhesive application pattern gained by the algorithm proposed in this thesis.

12.1 Outlook

In addition to the improvements suggested in subsection 11.1.3, different joining kinematics may be considered in the future, as perfectly parallel squeeze surfaces are not always the case in manufacturing. The algorithm could also be constrained to gain patterns that can be realised with existing application techniques, such as simple adhesive bead application. An extension to optimize a pattern considering the third, i.e. the height dimension, is also conceivable. Using highly thixotropic (stable) adhesives, a 3D application pattern could further prevent trapping air.

Furthermore, the optimization method could be extended to consider non-rigid substrates, as the occurring squeeze forces will deform the parts to be joined to some extent, and thus influence the gap height. In extreme cases, plastic deformations can occur, e.g. in automotive manufacturing when bonding thin-walled aluminium body components. Such elastic, or plastic deformations can be calculated with numerical methods, e.g. FEM and be implemented within the optimization routine of the optimization algorithm. However, an iterative procedure will be needed because the forces and additional deformations influence one another until the gap is closed.

References

[1] M. J. Adams et al. "A finite element analysis of the squeeze flow of an elasto-viscoplastic paste material". In: *Journal of Non-Newtonian Fluid Mechanics* 71.1-2 (1997), pp. 41–57. DOI: 10.1016/S0377-0257(96)01546-7.

[2] Martine Ben Amar and Daniel Bonn. "Fingering instabilities in adhesive failure". In: *Physica D: Nonlinear Phenomena* 209.1-4 (2005), pp. 1–16. DOI: 10.1016/j.physd.2005.07.002.

[3] Oded Amir and Ole Sigmund. "Reinforcement layout design for concrete structures based on continuum damage and truss topology optimization". In: *Structural and Multidisciplinary Optimization* 47.2 (2013), pp. 157–174. DOI: 10.1007/s00158-012-0817-1.

[4] Elisa Arikan et al. "The role of chemical surface modification for structural adhesive bonding on polymers - Washability of chemical functionalization without reducing adhesion". In: *International Journal of Adhesion and Adhesives* 95 (2019), p. 102409. DOI: 10.1016/j.ijadhadh.2019.102409.

[5] Mads Baandrup et al. "Closing the gap towards super-long suspension bridges using computational morphogenesis". In: *Nature Communications* 11.1 (2020), p. 2735. DOI: 10.1038/s41467-020-16599-6.

[6] A. Baldan. "Adhesively-bonded joints and repairs in metallic alloys, polymers and composite materials: Adhesives, adhesion theories and surface pretreatment". In: *Journal of Materials Science* 39.1 (2004), pp. 1–49. DOI: 10.1023/B:JMSC.0000007726.58758.e4.

[7] Aleksandra Biszczanik, Krzysztof Talaśka, and Dominik Wilczyński. "Analysis of the adhesive spread and the thickness of the adhesive bonded joint depending on the compressive force applied to bonded materials with different surface structure". In: *International Journal of Adhesion and Adhesives* 114 (2022), p. 103081. DOI: 10.1016/j.ijadhadh.2021.103081.

[8] José Pedro Blasques and Mathias Stolpe. *Multi-material topology optimization of laminated composite beam cross sections*. Vol. 94. 2012.

[9] Michael Bogomolny and Oded Amir. "Conceptual design of reinforced concrete structures using topology optimization with elastoplastic material modeling". In: *International Journal for Numerical Methods in Engineering* 90.13 (2012), pp. 1578–1597. DOI: 10.1002/nme.4253.

[10] Thomas Borrvall and Joakim Petersson. "Topology optimization of fluids in Stokes flow". In: *International Journal for Numerical Methods in Fluids* 41.1 (2003), pp. 77–107. DOI: 10.1002/fld.426.

[11] Neil Buckney et al. "On the structural topology of wind turbine blades". In: *Wind Energy* 16.4 (2013), pp. 545–560. DOI: 10.1002/we.1504.

[12] Pierre J. Carreau. "Rheological Equations from Molecular Network Theories". In: *Transactions of the Society of Rheology* 16.1 (1972), pp. 99–127. DOI: 10.1122/1.549276.

[13] J.-D. Chen. "Radial viscous fingering patterns in Hele-Shaw cells". In: *Experiments in Fluids* 5.6 (1987), pp. 363–371. DOI: 10.1007/BF00264399.

[14] Agustín Chiminelli et al. "Analysis of mixed adhesive joints considering the compaction process". In: *International Journal of Adhesion and Adhesives* 76 (2017), pp. 3–10. DOI: 10.1016/j.ijadhadh.2017.02.003.

[15] D.Nha Chu et al. "Evolutionary structural optimization for problems with stiffness constraints". In: *Finite Elements in Analysis and Design* 21.4 (1996), pp. 239–251. DOI: 10.1016/0168-874X(95)00043-S.

[16] Lucas Filipe Martins da Silva et al. *Introduction to Adhesive Bonding*. 1. Auflage. Weinheim: Wiley-VCH GmbH, 2021. ISBN: 9783527830541.

[17] Lucas F.M. da Silva and Maria João C.Q. Lopes. "Joint strength optimization by the mixed-adhesive technique". In: *International Journal of Adhesion and Adhesives* 29.5 (2009), pp. 509–514. DOI: 10.1016/j.ijadhadh.2008.09.009.

[18] Christian Denkert et al. "Experimental investigations on pre-tensioned hybrid joints for structural steel applications". In: *The Journal of Adhesion* (2021), pp. 1–36. DOI: 10.1080/00218464.2021.2003786.

[19] Mohammed El-Adawy et al. "Stereoscopic particle image velocimetry for engine flow measurements: Principles and applications". In: *Alexandria Engineering Journal* 60.3 (2021), pp. 3327–3344. DOI: 10.1016/j.aej.2021.01.060.

[20] Jan Engmann, Colin Servais, and Adam S. Burbidge. "Squeeze flow theory and applications to rheometry: A review". In: *Journal of Non-Newtonian Fluid Mechanics* 132.1-3 (2005), pp. 1–27. DOI: 10.1016/j.jnnfm.2005.08.007.

[21] Amin Etminan et al. "Flow visualization: state-of-the-art development of microparticle image velocimetry". In: *Measurement Science and Technology* 33.9 (2022), p. 092002. DOI: 10.1088/1361-6501/ac75b0.

[22] Helen E. Fairclough et al. "Theoretically optimal forms for very long-span bridges under gravity loading". In: *Proceedings. Mathematical, physical, and engineering sciences* 474.2217 (2018), p. 20170726. DOI: 10.1098/rspa.2017.0726.

[23] Vlad Florea et al. "3D multi-material and multi-joint topology optimization with tooling accessibility constraints". In: *Structural and Multidisciplinary Optimization* 60.6 (2019), pp. 2531–2558. DOI: 10.1007/s00158-019-02344-1.

[24] A. Gersborg-Hansen, O. Sigmund, and R. B. Haber. "Topology optimization of channel flow problems". In: *Structural and Multidisciplinary Optimization* 30.3 (2005), pp. 181–192. DOI: 10.1007/s00158-004-0508-7.

[25] James K. Guest and Jean H. Prévost. "Topology optimization of creeping fluid flows using a Darcy–Stokes finite element". In: *International Journal for Numerical Methods in Engineering* 66.3 (2006), pp. 461–484. DOI: 10.1002/nme.1560.

[26] Gerd Habenicht. *Kleben: Grundlagen, Technologien, Anwendungen*. 6th ed. Springer-Link Bücher. Berlin, Heidelberg: Springer Berlin Heidelberg, 2009. ISBN: 978-3-540-85266-7.

[27] H. S. Hele-Shaw. "Flow of Water". In: *Nature* 58.1509 (1898), p. 520. DOI: 10.1038/058520a0.

[28] H. S. Hele-Shaw. "Flow of Water". In: *Nature* 59.1523 (1899), pp. 222–223. DOI: 10.1038/059222d0.

[29] H. S. Hele-Shaw. "The Flow of Water". In: *Nature* 58.1489 (1898), pp. 34–36. DOI: 10.1038/058034a0.

[30] Bernhard Hoffner et al. "Squeezing flow of a highly viscous incompressible liquid pressed between slightly inclined lubricated wide plates". In: *Rheologica Acta* 40.3 (2001), pp. 289–295. DOI: 10.1007/s003970000123.

[31] G. M. Homsy. "Viscous Fingering in Porous Media". In: *Annual Review of Fluid Mechanics* 19.1 (1987), pp. 271–311. DOI: 10.1146/annurev.fl.19.010187.001415.

[32] H. Hu et al. "Dual-plane stereoscopic particle image velocimetry: system set-up and its application on a lobed jet mixing flow". In: *Experiments in Fluids* 31.3 (2001), pp. 277–293. DOI: 10.1007/s003480100283.

[33] X. Huang and Y. M. Xie. "Bi-directional evolutionary topology optimization of continuum structures with one or multiple materials". In: *Computational Mechanics* 43.3 (2009), pp. 393–401. DOI: 10.1007/s00466-008-0312-0.

[34] X. Huang and Y. M. Xie. "Convergent and mesh-independent solutions for the bi-directional evolutionary structural optimization method". In: *Finite Elements in Analysis and Design* 43.14 (2007), pp. 1039–1049. DOI: 10.1016/j.finel.2007.06.006.

[35] X. Huang and Y. M. Xie. "Topology optimization of nonlinear structures under displacement loading". In: *Engineering Structures* 30.7 (2008), pp. 2057–2068. DOI: 10.1016/j.engstruct.2008.01.009.

[36] Xiaodong Huang and Mike Xie. *Evolutionary Topology Optimization of Continuum Structures: Methods and Applications*. 2nd ed. Hoboken: John Wiley & Sons Ltd, 2010. ISBN: 9780470746530.

[37] Xiaodong Huang and Yi-Min Xie. "A further review of ESO type methods for topology optimization". In: *Structural and Multidisciplinary Optimization* 41.5 (2010), pp. 671–683. DOI: 10.1007/s00158-010-0487-9.

[38] Xiaodong Huang, Yi Min Xie, and Mark Cameron Burry. "A New Algorithm for Bi-Directional Evolutionary Structural Optimization". In: *JSME International Journal Series C* 49.4 (2006), pp. 1091–1099. DOI: 10.1299/jsmec.49.1091.

[39] Simon Ingelsten et al. "Simulation of viscoelastic squeeze flows for adhesive joining applications". In: *Journal of Non-Newtonian Fluid Mechanics* 300 (2022), p. 104722. DOI: 10.1016/j.jnnfm.2021.104722.

[40] J. D. Jackson. "A study of squeezing flow". In: *Applied Scientific Research, Section A* 11.1 (1963), pp. 148–152. DOI: 10.1007/BF03184719.

[41] Davin Jankovics et al. "Developing Topology Optimization with Additive Manufacturing Constraints in ANSYS®". In: *IFAC-PapersOnLine* 51.11 (2018), pp. 1359–1364. DOI: 10.1016/j.ifacol.2018.08.340.

[42] Seung Hyun Jeong, Dong-Hoon Choi, and Gil Ho Yoon. "Fatigue and static failure considerations using a topology optimization method". In: *Applied Mathematical Modelling* 39.3-4 (2015), pp. 1137–1162. DOI: 10.1016/j.apm.2014.07.020.

[43] George Karapetsas and John Tsamopoulos. "Transient squeeze flow of viscoplastic materials". In: *Journal of Non-Newtonian Fluid Mechanics* 133.1 (2006), pp. 35–56. DOI: 10.1016/j.jnnfm.2005.10.010.

[44] Marvin Kaufmann and Till Vallée. "Topology optimization of adhesively bonded double lap joints". In: *International Journal of Adhesion and Adhesives* (2022), 1032 bibrangedash 38. DOI: 10.1016/j.ijadhadh.2022.103238.

[45] Marvin Kaufmann et al. "Do surface pretreatments for adhesives influence the squeeze flow?" In: *International Journal of Adhesion and Adhesives* (2023), p. 103362. DOI: 10.1016/j.ijadhadh.2023.103362.

[46] Marvin Kaufmann et al. "Experimental validation of a compression flow model of Non-Newtonian adhesives". In: *The Journal of Adhesion* (2021), pp. 1–30. DOI: 10.1080/00218464.2021.1971081.

[47] Marvin Kaufmann et al. "How adhesives flow during joining". In: *International Journal of Adhesion and Adhesives* (2022), p. 103315. DOI: 10.1016/j.ijadhadh.2022.103315.

[48] Serdar Koltuk, Tomas M. Fernandez-Steeger, and Rafig Azzam. "Einfluss der Bodenschichtung auf hydraulischen Grundbruch in Baugruben in nichtbindigen Böden". In: *Grundwasser* 26.3 (2021), pp. 255–268. DOI: 10.1007/s00767-021-00487-x.

[49] A. Kruse et al. "Surface pretreatment of plastics for adhesive bonding". In: *Journal of Adhesion Science and Technology* 9.12 (1995), pp. 1611–1621. DOI: 10.1163/156856195X00248.

[50] Dochan Kwak and Cetin C. Kiris. "Artificial Compressibility Method". In: *Computation of Viscous Incompressible Flows*. Ed. by Dochan Kwak. Scientific Computation Ser. Dordrecht: Springer Netherlands, 2011, pp. 41–77. ISBN: 978-94-007-0192-2.

[51] Yeon-Seung Lee et al. "Structural topology optimization of the transition piece for an offshore wind turbine with jacket foundation". In: *Renewable Energy* 85 (2016), pp. 1214–1225. DOI: 10.1016/j.renene.2015.07.052.

[52] Philip J. Leider. "Squeezing Flow between Parallel Disks. II. Experimental Results". In: *Industrial & Engineering Chemistry Fundamentals* 13.4 (1974), pp. 342–346. DOI: 10.1021/i160052a008.

[53] Q. Li, G. P. Steven, and Y. M. Xie. "A simple checkerboard suppression algorithm for evolutionary structural optimization". In: *Structural and Multidisciplinary Optimization* 22.3 (2001), pp. 230–239. DOI: 10.1007/s001580100140.

[54] Q. Q. Liang, Y. M. Xie, and G. P. Steven. "A performance index for topology and shape optimization of plate bending problems with displacement constraints". In: *Structural and Multidisciplinary Optimization* 21.5 (2001), pp. 393–399. DOI: 10.1007/PL00013281.

[55] Haidong Lin et al. "An ANSYS APDL code for topology optimization of structures with multi-constraints using the BESO method with dynamic evolution rate (DER-BESO)". In: *Structural and Multidisciplinary Optimization* 62.4 (2020), pp. 2229–2254. DOI: 10.1007/s00158-020-02588-2.

[56] Shutian Liu and Heting Qiao. "Topology optimization of continuum structures with different tensile and compressive properties in bridge layout design". In: *Structural and Multidisciplinary Optimization* 43.3 (2011), pp. 369–380. DOI: 10.1007/s00158-010-0567-x.

[57] R. M. Lueptow, A. Akonur, and T. Shinbrot. "PIV for granular flows". In: *Experiments in Fluids* 28.2 (2000), pp. 183–186. DOI: 10.1007/s003480050023.

[58] Yangjun Luo and Zhan Kang. "Layout design of reinforced concrete structures using two-material topology optimization with Drucker–Prager yield constraints". In: *Structural and Multidisciplinary Optimization* 47.1 (2013), pp. 95–110. DOI: 10.1007/s00158-012-0809-1.

[59] David C. Mandeville. "Methods for Applying Adhesives and Sealants on Body Assemblies in Robotic Applications". In: *SAE Technical Paper Series*. SAE Technical Paper Series. SAE International400 Commonwealth Drive, Warrendale, PA, United States, 1998.

[60] S. Mascia and D. I. Wilson. "Biaxial extensional rheology of granular suspensions: The HBP (Herschel-Bulkley for Pastes) model". In: *Journal of Rheology* 52.4 (2008), pp. 981–998. DOI: 10.1122/1.2930876.

[61] Gerald Meeten. "Constant-force squeeze flow of soft solids". In: *Rheologica Acta* 41.6 (2002), pp. 557–566. DOI: 10.1007/s00397-002-0241-3.

[62] Gerald Henry Meeten. "Flow of soft solids squeezed between planar and spherical surfaces". In: *Rheologica Acta* 44.6 (2005), pp. 563–572. DOI: 10.1007/s00397-005-0437-4.

[63] A. Melling. "Tracer particles and seeding for particle image velocimetry". In: *Measurement Science and Technology* 8.12 (1997), pp. 1406–1416. DOI: 10.1088/0957-0233/8/12/005.

[64] A. G. M. Michell. "LVIII. The limits of economy of material in frame-structures". In: *The London, Edinburgh, and Dublin Philosophical Magazine and Journal of Science* 8.47 (1904), pp. 589–597. DOI: 10.1080/14786440409463229.

[65] Michael Müller, Georg-Peter Ostermeyer, and Florian Bubser. "A contribution to the modeling of tribological processes under starved lubrication". In: *Tribology International* 64 (2013), pp. 135–147. DOI: 10.1016/j.triboint.2013.03.011.

[66] Michael Müller et al. "An efficient numerical model for the evaluation of compression flow of high-viscosity adhesives". In: *International Journal of Adhesion and Adhesives* 85 (2018), pp. 251–262. DOI: 10.1016/j.ijadhadh.2018.05.023.

[67] Michael Müller et al. "Development and validation of a compression flow model of non-Newtonian adhesives". In: *The Journal of Adhesion* (2021), pp. 1–38. DOI: 10.1080/00218464.2021.1895771.

[68] Michael Müller et al. "Simulative studies of tribological interfaces with partially filled gaps". In: *Tribology International* 78 (2014), pp. 195–209. DOI: 10.1016/j.triboint.2014.05.002.

[69] Michael Müller et al. "Towards the efficient modelling of trapped air pockets during squeeze flow". In: *Experimental and Computational Multiphase Flow* (2022), pp. 1–24. DOI: 10.1007/s42757-021-0125-3.

[70] Devang S. Nath et al. "Drag reduction by application of aerodynamic devices in a race car". In: *Advances in Aerodynamics* 3.1 (2021), pp. 1–20. DOI: 10.1186/s42774-020-00054-7.

[71] D. Nha Chu et al. "On various aspects of evolutionary structural optimization for problems with stiffness constraints". In: *Finite Elements in Analysis and Design* 24.4 (1997), pp. 197–212. DOI: 10.1016/S0168-874X(96)00049-2.

[72] Laurits Højgaard Olesen, Fridolin Okkels, and Henrik Bruus. "A high-level programming-language implementation of topology optimization applied to steady-state Navier-Stokes flow". In: *International Journal for Numerical Methods in Engineering* 65.7 (2006), pp. 975–1001. DOI: 10.1002/nme.1468.

[73] Anderson Pereira et al. "Fluid flow topology optimization in PolyTop: stability and computational implementation". In: *Structural and Multidisciplinary Optimization* 54.5 (2016), pp. 1345–1364. DOI: 10.1007/s00158-014-1182-z.

[74] O. M. Querin, G. P. Steven, and Y. M. Xie. "Evolutionary structural optimisation (ESO) using a bidirectional algorithm". In: *Engineering Computations* 15.8 (1998), pp. 1031–1048. DOI: 10.1108/02644409810244129.

[75] O. M. Querin, G. P. Steven, and Y. M. Xie. "Evolutionary structural optimisation using an additive algorithm". In: *Finite Elements in Analysis and Design* 34.3-4 (2000), pp. 291–308. DOI: 10.1016/S0168-874X(99)00044-X.

[76] O. M. Querin et al. "Computational efficiency and validation of bi-directional evolutionary structural optimisation". In: *Computer Methods in Applied Mechanics and Engineering* 189.2 (2000), pp. 559–573. DOI: 10.1016/S0045-7825(99)00309-6.

[77] Brooks D. Rabideau, Christophe Lanos, and Philippe Coussot. "An investigation of squeeze flow as a viable technique for determining the yield stress". In: *Rheologica Acta* 48.5 (2009), pp. 517–526. DOI: 10.1007/s00397-009-0347-y.

[78] Osborne Reynolds. "IV. On the theory of lubrication and its application to Mr. Beauchamp tower's experiments, including an experimental determination of the viscosity of olive oil". In: *Philosophical Transactions of the Royal Society of London* 177 (1886), pp. 157–234. DOI: 10.1098/rstl.1886.0005.

[79] Anna Rudawska. "Selected aspects of the effect of mechanical treatment on surface roughness and adhesive joint strength of steel sheets". In: *International Journal of Adhesion and Adhesives* 50 (2014), pp. 235–243. DOI: 10.1016/j.ijadhadh.2014.01.032.

[80] Philip Geoffrey Saffman and Geoffrey Ingram Taylor. "The penetration of a fluid into a porous medium or Hele-Shaw cell containing a more viscous liquid". In: *Proceedings of the Royal Society of London. Series A. Mathematical and Physical Sciences* 245.1242 (1958), pp. 312–329. DOI: 10.1098/rspa.1958.0085.

[81] J. G. Santiago et al. "A particle image velocimetry system for microfluidics". In: *Experiments in Fluids* 25.4 (1998), pp. 316–319. DOI: 10.1007/s003480050235.

[82] Dominik Schittenhelm, Andreas Burblies, and Matthias Busse. "Stahlverstärkter Aluminiumguss". In: *Forschung im Ingenieurwesen* 82.2 (2018), pp. 131–147. DOI: 10.1007/s10010-018-0263-3.

[83] Ahmed Sengab and Ramesh Talreja. "A numerical study of failure of an adhesive joint influenced by a void in the adhesive". In: *Composite Structures* 156 (2016), pp. 165–170. DOI: 10.1016/j.compstruct.2015.12.052.

[84] Mario Smarslik, Mark Alexander Ahrens, and Peter Mark. "Toward holistic tension- or compression-biased structural designs using topology optimization". In: *Engineering Structures* 199 (2019), p. 109632. DOI: 10.1016/j.engstruct.2019.109632.

[85] B. Stawarczyk et al. "Influence of plasma pretreatment on shear bond strength of self-adhesive resin cements to polyetheretherketone". In: *Clinical Oral Investigations* 18.1 (2014), pp. 163–170. DOI: 10.1007/s00784-013-0966-7.

[86] William Thielicke and René Sonntag. "Particle Image Velocimetry for MATLAB: Accuracy and enhanced algorithms in PIVlab". In: *Journal of Open Research Software* 9.1 (2021). DOI: 10.5334/jors.334.

[87] William Thielicke and Eize J. Stamhuis. "PIVlab – Towards User-friendly, Affordable and Accurate Digital Particle Image Velocimetry in MATLAB". In: *Journal of Open Research Software* 2.1 (2014). DOI: 10.5334/jors.bl.

[88] Simon Thomas, Qing Li, and Grant Steven. "Topology optimization for periodic multi-component structures with stiffness and frequency criteria". In: *Structural and Multidisciplinary Optimization* 61.6 (2020), pp. 2271–2289. DOI: 10.1007/s00158-019-02481-7.

[89] Xiaojie Tian et al. *Optimization design of the jacket support structure for offshore wind turbine using topology optimization method*. Vol. 243. 2022.

[90] M. Toloui et al. "Measurement of atmospheric boundary layer based on super-large-scale particle image velocimetry using natural snowfall". In: *Experiments in Fluids* 55.5 (2014), pp. 1–14. DOI: 10.1007/s00348-014-1737-1.

[91] Till Vallée et al. "Influence of stress-reduction methods on the strength of adhesively bonded joints composed of orthotropic brittle adherends". In: *International Journal of Adhesion and Adhesives* 30.7 (2010), pp. 583–594. DOI: 10.1016/j.ijadhadh.2010.05.007.

[92] Gieljan Vantyghem et al. "3D printing of a post-tensioned concrete girder designed by topology optimization". In: *Automation in Construction* 112 (2020), p. 103084. DOI: 10.1016/j.autcon.2020.103084.

[93] Morten Voß. "Accelerated curing of adhesives using inductively heated Curie particles". PhD thesis. Universität Bremen, 2023.

[94] Erwin Walraven, Matthijs T.J. Spaan, and Bram Bakker. "Traffic flow optimization: A reinforcement learning approach". In: *Engineering Applications of Artificial Intelligence* 52 (2016), pp. 203–212. DOI: 10.1016/j.engappai.2016.01.001.

[95] Steven T. Wereley and Carl D. Meinhart. "Recent Advances in Micro-Particle Image Velocimetry". In: *Annual Review of Fluid Mechanics* 42.1 (2010), pp. 557–576. DOI: 10.1146/annurev-fluid-121108-145427.

[96] Jerry Westerweel, Gerrit E. Elsinga, and Ronald J. Adrian. "Particle Image Velocimetry for Complex and Turbulent Flows". In: *Annual Review of Fluid Mechanics* 45.1 (2013), pp. 409–436. DOI: 10.1146/annurev-fluid-120710-101204.

[97] Liang Xia, Felix Fritzen, and Piotr Breitkopf. "Evolutionary topology optimization of elastoplastic structures". In: *Structural and Multidisciplinary Optimization* 55.2 (2017), pp. 569–581. DOI: 10.1007/s00158-016-1523-1.

[98] Liang Xia et al. "Bi-directional Evolutionary Structural Optimization on Advanced Structures and Materials: A Comprehensive Review". In: *Archives of Computational Methods in Engineering* 25.2 (2018), pp. 437–478. DOI: 10.1007/s11831-016-9203-2.

[99] Y. M. Xie and G. P. Steven. "A simple approach to structural frequency optimization". In: *Computers & Structures* 53.6 (1994), pp. 1487–1491. DOI: 10.1016/0045-7949(94)90414-6.

[100] Y. M. Xie and G. P. Steven. "A simple evolutionary procedure for structural optimization". In: *Computers & Structures* 49.5 (1993), pp. 885–896. DOI: 10.1016/0045-7949(93)90035-C.

[101] Y. M. Xie and G. P. Steven. "Evolutionary structural optimization for dynamic problems". In: *Computers & Structures* 58.6 (1996), pp. 1067–1073. DOI: 10.1016/0045-7949(95)00235-9.

[102] Kentaro Yaji et al. "Topology optimization in thermal-fluid flow using the lattice Boltzmann method". In: *Journal of Computational Physics* 307 (2016), pp. 355–377. DOI: 10.1016/j.jcp.2015.12.008.

[103] K. Yasuda, R. C. Armstrong, and R. E. Cohen. "Shear flow properties of concentrated solutions of linear and star branched polystyrenes". In: *Rheologica Acta* 20.2 (1981), pp. 163–178. DOI: 10.1007/BF01513059.

[104] V. Young et al. "3D and multiple load case bi-directional evolutionary structural optimization (BESO)". In: *Structural and Multidisciplinary Optimization* 18.2-3 (1999), pp. 183–192. DOI: 10.1007/BF01195993.

[105] Bingxiang Yuan et al. *Development of a Robust Stereo-PIV System for 3-D Soil Deformation Measurement*. Vol. 40. 2012.

[106] Yuri Petryna, Andreas Künzel, and Matthias Kannenberg, eds. *Fault Detection and State Evaluation of Rotor Blades*. 2014.

[107] Giulio Zani et al. "Three-dimensional modelling of a multi-span masonry arch bridge: Influence of soil compressibility on the structural response under vertical static loads". In: *Engineering Structures* 221 (2020), p. 110998. DOI: 10.1016/j.engstruct.2020.110998.

[108] Jihong ZHU et al. "A review of topology optimization for additive manufacturing: Status and challenges". In: *Chinese Journal of Aeronautics* 34.1 (2021), pp. 91–110. DOI: 10.1016/j.cja.2020.09.020.

Appendix

All additional video material provided can be accessed through the link:

https://owncloud.fraunhofer.de/index.php/s/3QtpEDO99pNMSdW

Or by scanning the QR-Code:

A Further Optimization Examples

A.1 Square

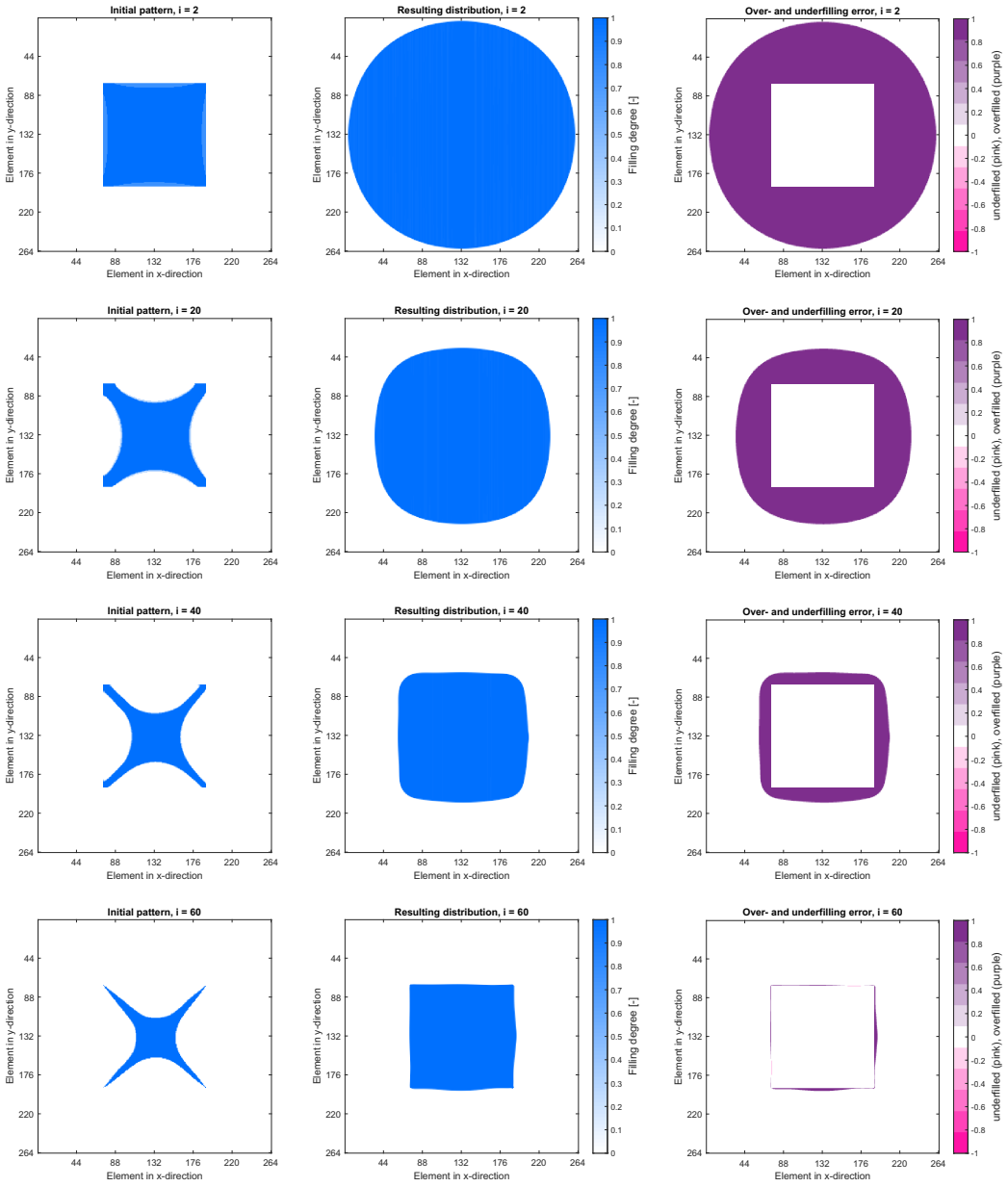

Figure A.1: Process to find an optimized initial pattern to be squeezed into a square: iterative development of initial pattern (left), resulting distribution (middle) and difference between resulting and target distribution (right).

A.2 Rectangle

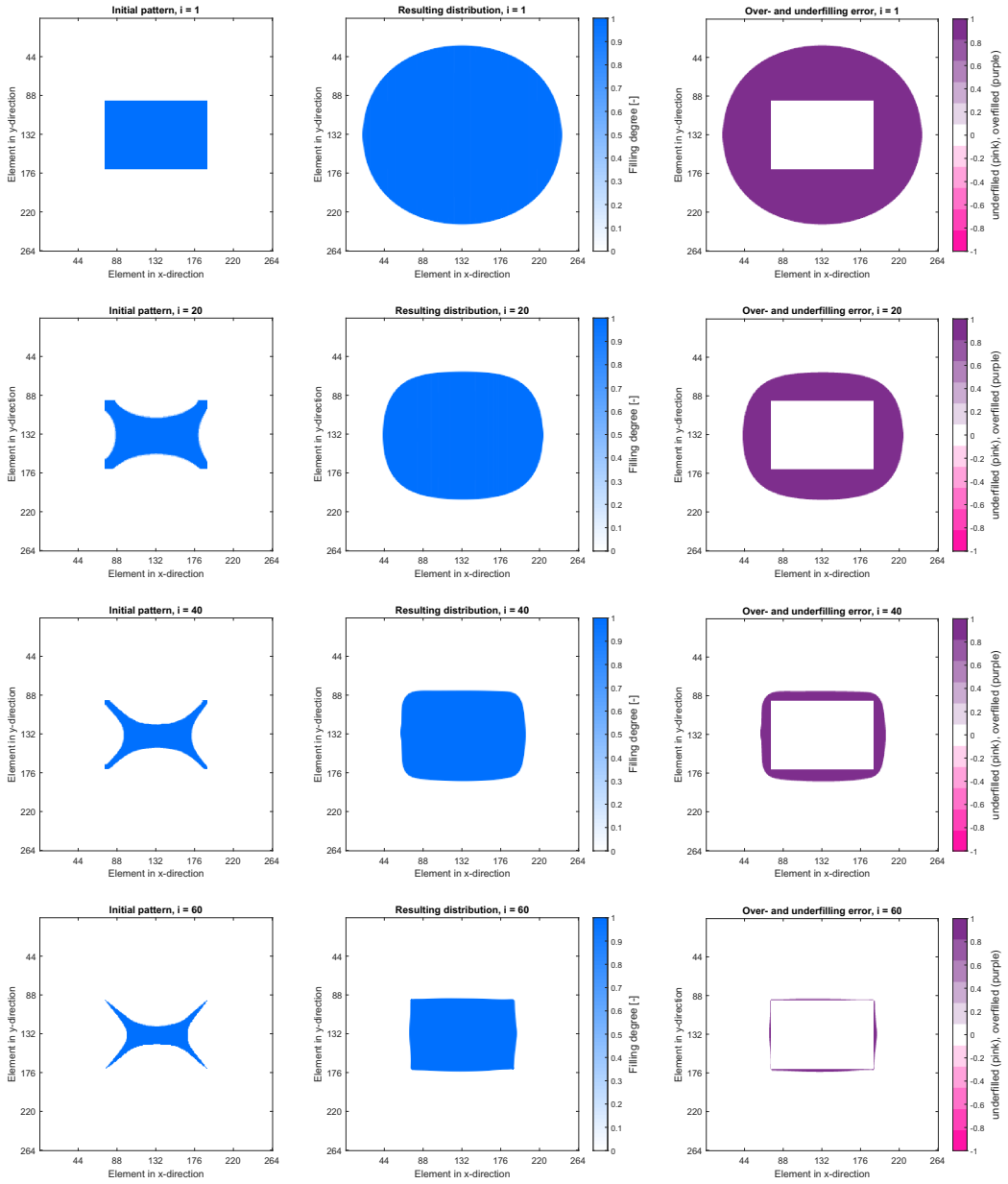

Figure A.2: Process to find an optimized initial pattern to be squeezed into a rectangle: iterative development of initial pattern (left), resulting distribution (middle) and difference between resulting and target distribution (right).

A.3 Open Circle

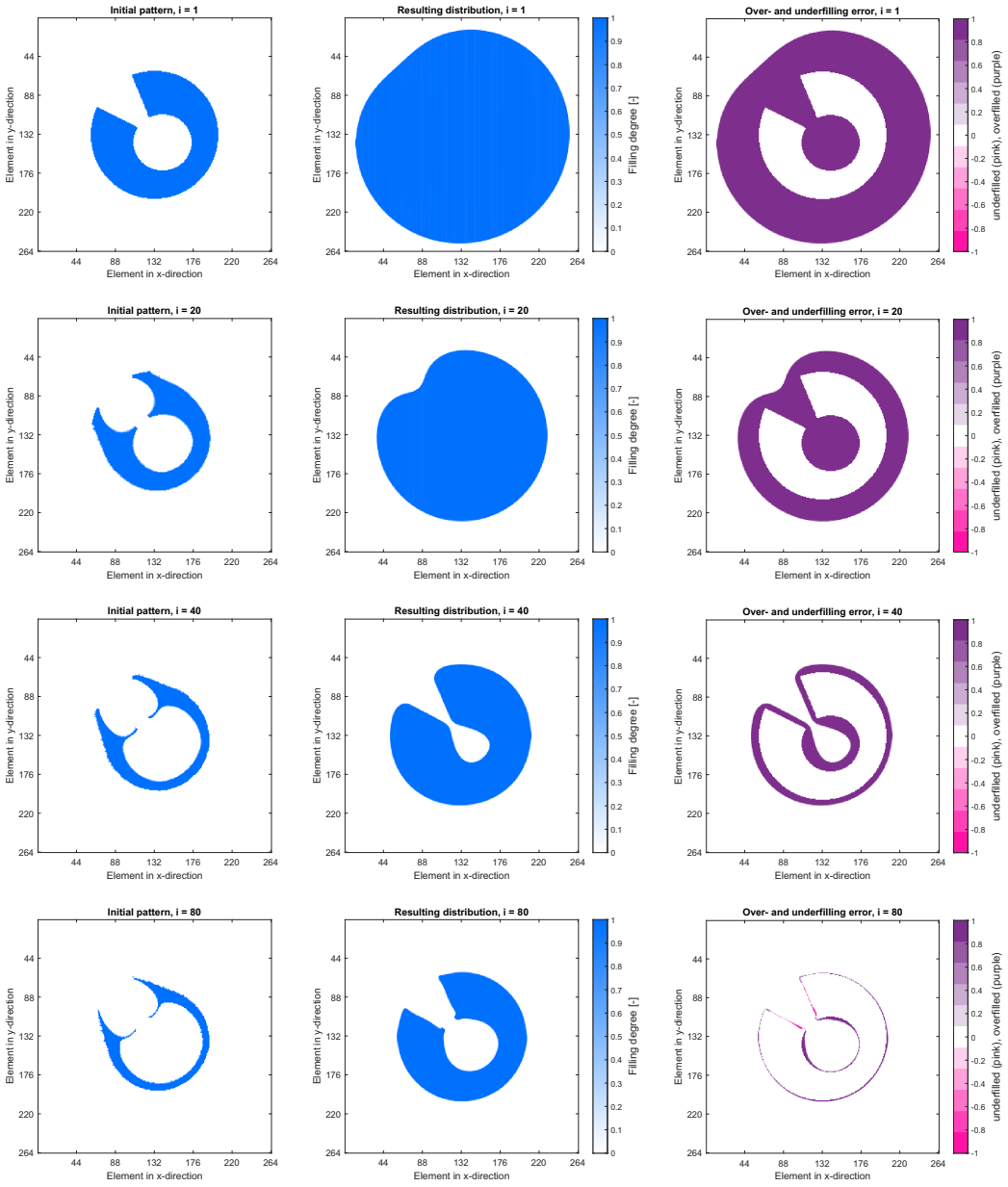

Figure A.3: Process to find an optimized initial pattern to be squeezed into an open circle: iterative development of initial pattern (left), resulting distribution (middle) and difference between resulting and target distribution (right).

A.4 Heart Shape

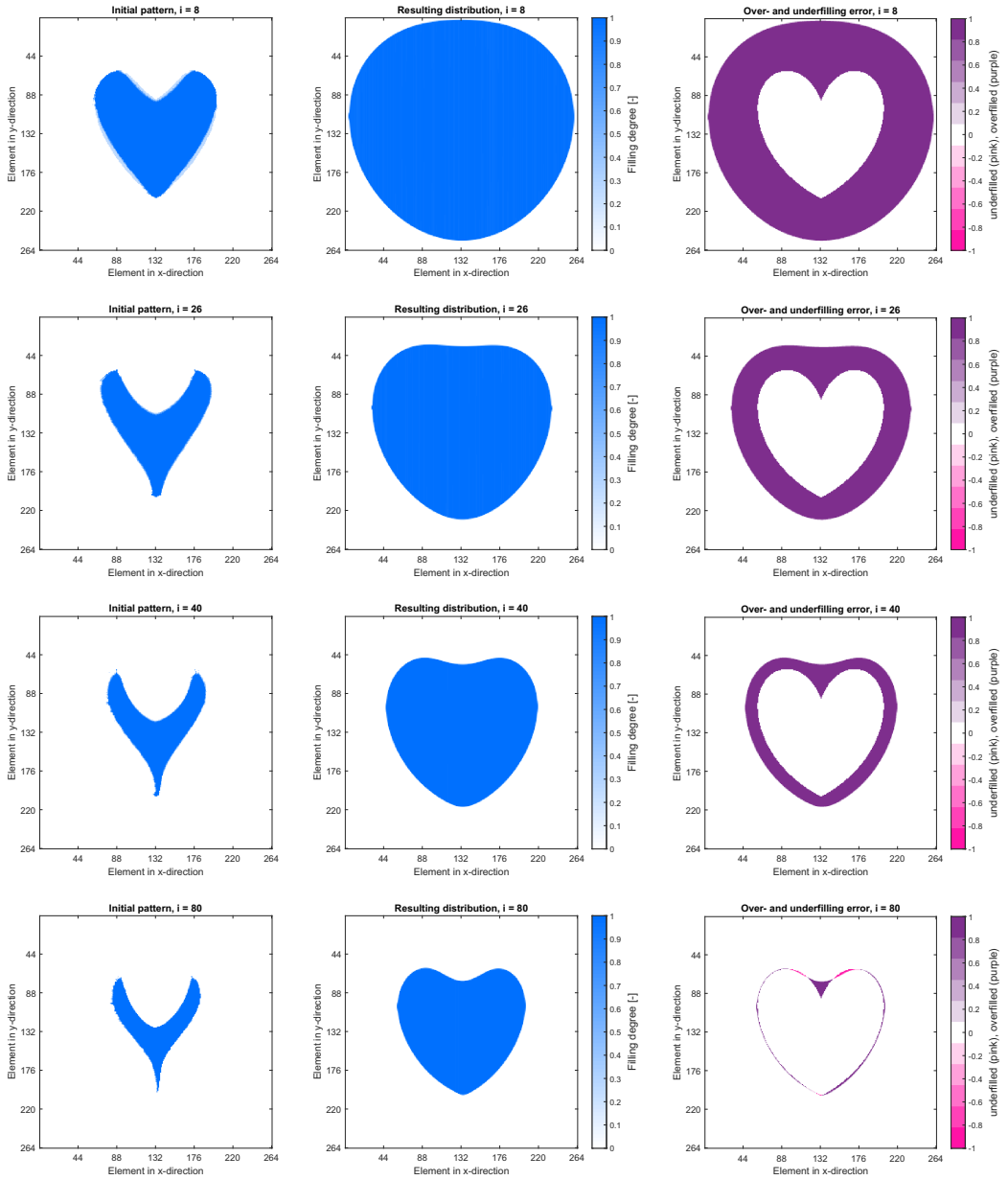

Figure A.4: Process to find an optimized initial pattern to be squeezed into a heart shape: iterative development of initial pattern (left), resulting distribution (middle) and difference between resulting and target distribution (right).

A.5 Arbitrary Form

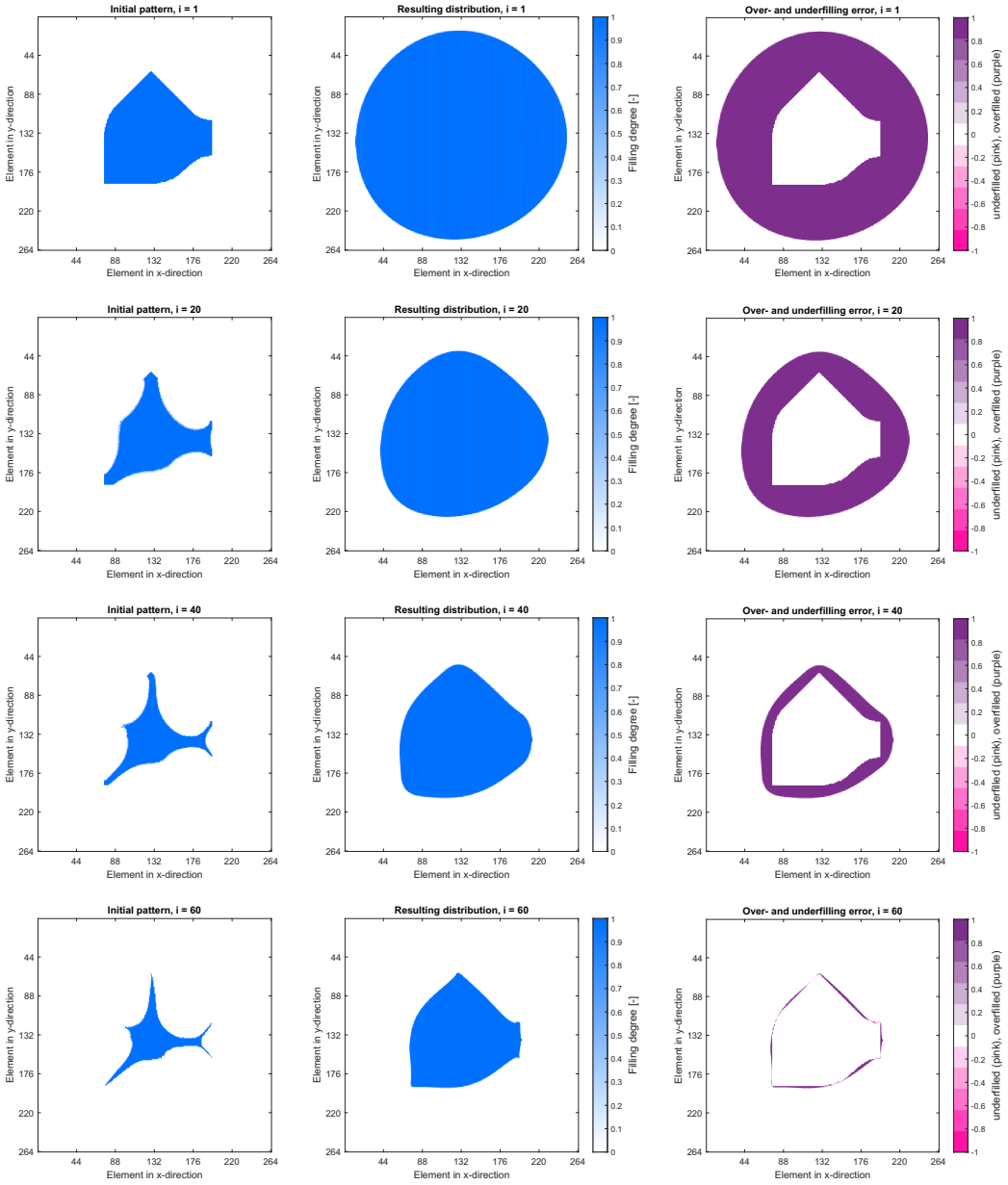

Figure A.5: Process to find an optimized initial pattern to be squeezed into an arbitrary shape: iterative development of initial pattern (left), resulting distribution (middle) and difference between resulting and target distribution (right).

A.6 Odd Shape

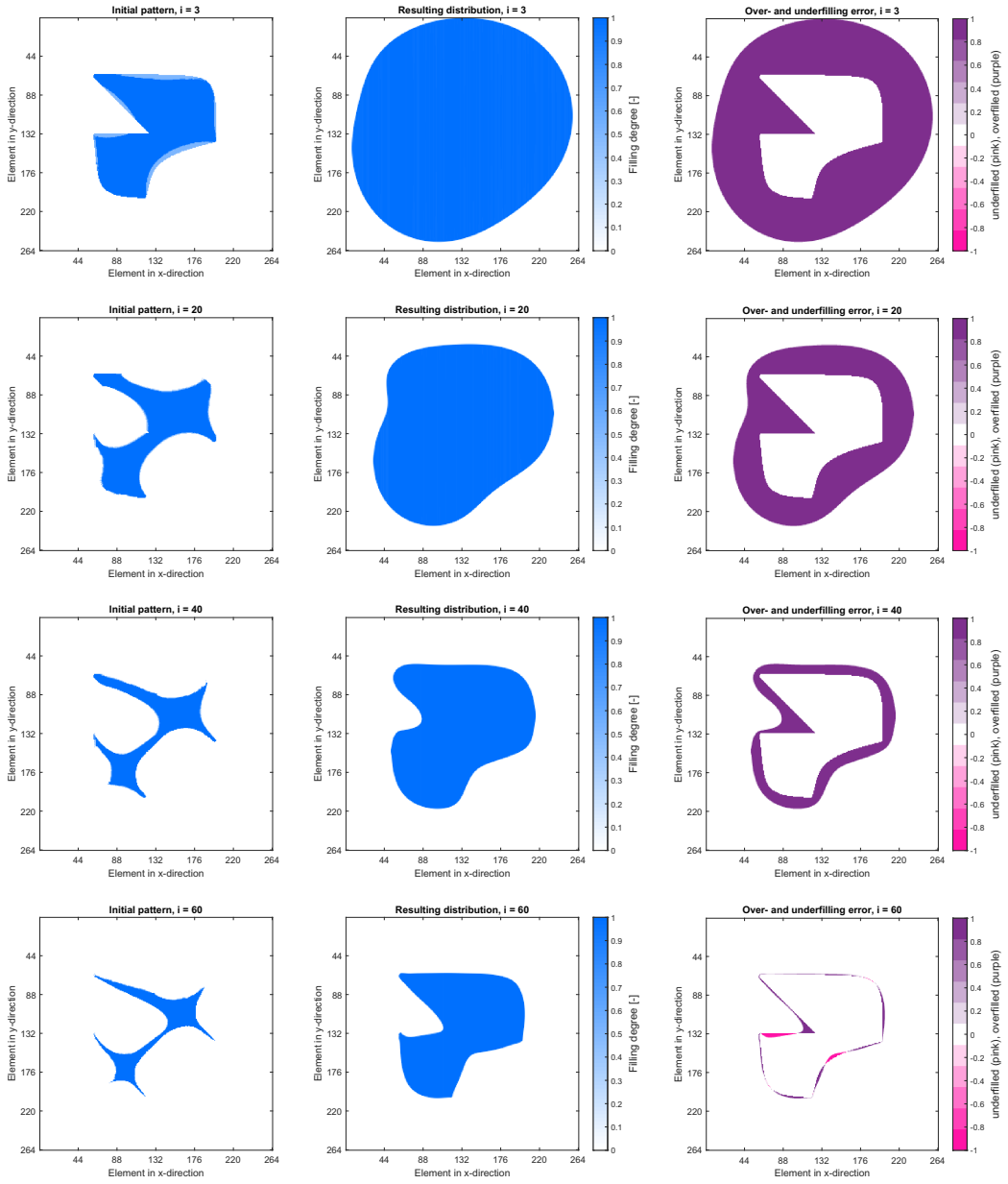

Figure A.6: Process to find an optimized initial pattern to be squeezed into an arbitrary shape: iterative development of initial pattern (left), resulting distribution (middle) and difference between resulting and target distribution (right).

B List of Publications

Publications

Peer Reviewed Journals

2024
- **Optimized adhesive application**
  Kaufmann, M., Flaig, F., Müller, M., Fricke, H., Vallée, T.
  International Journal of Adhesion and Adhesives
  https://doi.org/10.1016/j.ijadhadh.2024.103620

2023
- **How to find the perfect application pattern for adhesively bonded joints?**
  Flaig, F., Fräger, T., Kaufmann, M., Vallée, T., Fricke, H., Müller, M.
  Journal of Advanced Joining Processes
  https://doi.org/10.1016/j.jajp.2023.100147

2023
- **Are probabilistic methods a way to get rid of fudge factors? Part II: Application and examples**
  Vallée, T., Kaufmann, M., Adams, R.D., Albiez, M., Correia, J.R., Tannert, T.
  International Journal of Adhesion and Adhesives
  https://doi.org/10.1016/j.ijadhadh.2023.103364

2023
- **Do surface pretreatments for adhesives influence the squeeze flow?**
  Kaufmann, M., Flaig, F., Müller, M., Fricke, H., Vallée, T.
  International Journal of Adhesion and Adhesives
  https://doi.org/10.1016/j.ijadhadh.2023.103362

2023
- **How adhesives flow during joining**
  Kaufmann, M., Flaig, F., Müller, M., Fricke, H., Vallée, T.
  International Journal of Adhesion and Adhesives
  https://doi.org/10.1016/j.ijadhadh.2022.103315

2023
- **Construction adhesives: Qualification, specification, quality control, and risk mitigation**
  Vallée, T., Kaufmann, M., Voß, M.
  Advances in Structural Adhesive Bonding
  https://doi.org/10.1016/B978-0-323-91214-3.00013-2

2023
- **Experimental investigations on pre-tensioned hybrid joints for structural steel applications**
  Denkert, C., Gerke, T., Glienke, R., Dörre, M., Henkel, M.K., Fricke, H., Myslicki, S., Kaufmann, M., Voß, M., Vallée, T.
  The Journal of Adhesion
  https://doi.org/10.1080/00218464.2021.2003786

2022
- **Are probabilistic methods a way to get rid of fudge factors? Part I: Background and theory**
  Vallée, T., Kaufmann, M., Adams, R.D., Albiez, M., Correia, J.R., Tannert, T.
  International Journal of Adhesion and Adhesives
  https://doi.org/10.1016/j.ijadhadh.2022.103255

2022
- **Topology optimization of adhesively bonded double lap joints**
  Kaufmann, M., Vallée, T.
  International Journal of Adhesion and Adhesives
  https://doi.org/10.1016/j.ijadhadh.2022.103238

2022

- **Hybrid joining of jacket structures for offshore wind turbines – Determination of requirements and adhesive characterisation**

  Albiez, M., Damm, J., Ummenhofer, T., Kaufmann, M., Vallée, T., Myslicki, S.
  Engineering Structures
  https://doi.org/10.1016/j.engstruct.2022.114186

2022

- **Hybrid joining of jacket structures for offshore wind turbines – Validation under static and dynamic loading at medium and large scale**

  Albiez, M., Damm, J., Ummenhofer, T., Ehard, H., Schuler, C., Kaufmann, M., Vallée, T., Myslicki, S.
  Engineering Structures
  https://doi.org/10.1016/j.engstruct.2021.113595

2022

- **Experimental validation of a compression flow model of Non-Newtonian adhesives**

  Kaufmann, M., Flaig, F., Müller, M., Stahl, L., Finke, J., Vallée, T., Fricke, H.
  The Journal of Adhesion
  https://doi.org/10.1080/00218464.2021.1971081

2022

- **Curie–supported accelerated curing by means of inductive heating–Part II Validation and numerical studies**

  Voß, M., Kaufmann, M., Vallée, T.
  The Journal of Adhesion
  https://doi.org/10.1080/00218464.2021.1951712

2022

- **Curie-supported accelerated curing by means of inductive heating–Part I: Model building**

  Voß, M., Kaufmann, M., Vallée, T.
  The Journal of Adhesion
  https://doi.org/10.1080/00218464.2021.1902810

2022

- **Modelling and strength prediction of pre-tensioned hybrid bonded joints for structural steel applications**

  Vallée, T., Fricke, H., Myslicki, S., Kaufmann, M., Voß, M., Denkert, C., Glienke, R., Dörre, M., Henkel, M.-K., Gerke, T.
  The Journal of Adhesion
  https://doi.org/10.1080/00218464.2021.1928498

2022

- **Accelerated curing of glued-in threaded rods by means of inductive heating — part IV: curing under low temperatures**

  Ratsch, N., Burnett-Barking, M., Böhm, S., Voß, M., Adam, M., Kaufmann, M., Vallée, T.
  The Journal of Adhesion
  https://doi.org/10.1080/00218464.2020.1818562

2021

- **Accelerated curing of adhesively bonded G-FRP tube connections—Part III: Modelling of strength**

  Voß, M., Vallée, T., Kaufmann, M.
  Composite Structures
  https://doi.org/10.1016/j.compstruct.2021.113900

2021

- **Influence of manufacturing methods and imperfections on the load capacity of glued-in rods**

  Kohl, D., Ratsch, N., Böhm, S., Voß, M., Kaufmann, M., Vallée, T.
  The Journal of Adhesion
  https://doi.org/10.1080/00218464.2018.1508351

2020

- **Under water glued stud bonding fasteners for offshore structures**
  Myslicki, S., Kordy, H., Kaufmann, M., Créac'hcadec, R., Vallée, T.
  International Journal of Adhesion and Adhesives
  https://doi.org/10.1016/j.ijadhadh.2019.102533

2019

- **Influence of imperfections on the load capacity and stiffness of glued-in rod connections**
  Ratsch, N., Böhm, S., Voß, M., Kaufmann, M., Vallée, T.
  Construction and Building Materials
  https://doi.org/10.1016/j.conbuildmat.2019.07.278

2018

- **Numerical investigations and capacity prediction of G-FRP rods glued into timber**
  Grunwald, C., Kaufmann, M., Alter, B., Vallée, T., Tannert, T.
  Composite Structures
  https://doi.org/10.1016/j.compstruct.2017.10.010

2018

- **Hardwood rods glued into softwood using environmentally sustainable adhesives**
  Kaufmann, M., Kolbe, J., Vallée, T.
  The Journal of Adhesion
  https://doi.org/10.1080/00218464.2017.1385459

Non-Peer Reviewed Journals

2021

- **Influence of constructional details on bonds of pultruded GRP lamellae**
  Kruse, A., Grunwald, C., Kaufmann, M., Voß, M., Vallée, T.
  Adhäsion Kleben & Dichten
  https://doi.org/10.1007/s35145-021-0490-x

2021

- **Quick curing of bonded FRP pipes by induction (Part 2)**
  Haupt, J., Voß, M., Kaufmann, M., Grunwald, C., Vallée, T., Bode, M.
  Adhäsion Kleben & Dichten
  https://doi.org/10.1007/s35145-021-0480-z

2017

- **The eco-bar in wood construction**
  Kaufmann, M., Fecht, S., Kolbe, J., Vallée, T., Lochte-Holtgreven, S.
  Adhäsion Kleben & Dichten
  https://doi.org/10.1007/s35145-017-0041-7

Conferences

2023

EURADH 2023 – 14th European Adhesion Conference

- *FEICA Prize Award Lecture:* How adhesives flow during joining
  M. Kaufmann, F. Flaig, M. Müller, H. Fricke, T. Vallée

2023

AB2023 – 7th International Conference on Structural Adhesive Bonding

- *Lecture:* Simulation of adhesive flow and hardening
  T. Vallée, H. Fricke, F. Flaig, M. Müller, M. Kaufmann, J. Wirries, M. Rütters

- *Presentation:* How adhesives flow during joining
  M. Kaufmann, F. Flaig, M. Mueller, H. Fricke, T. Vallée

- *Presentation:* Consideration of air pockets and nonnewtonian fluids for adhesive squeeze flows
  M. Müller, F. Flaig, M. Kaufmann, T. Vallée, H. Fricke

- *Presentation:* Optimized adhesive application
  M. Kaufmann, F. Flaig, M. Mueller, H. Fricke, T. Vallée

- *Presentation:* Optimization strategies to determine ideal application patterns
  F. Flaig, M. Müller, M. Kaufmann, T. Vallée, H. Fricke

- *Presentation:* Are probabilistic methods a way to get rid of fudge factors?
  T. Vallée, M. Kaufmann, R.D. Adams, M. Albiez, J.R. Correia, T. Tannert

2022 **ECCM 2022 – 20th European Conference on Composite Materials**

- *Presentation:* Experimental investigations on accelerated curing of adhesively bonded G-FRP tube connections
  Voß, M., Kaufmann, M., Vallée, T.

- *Presentation:* Modelling of accelerated curing of adhesively bonded G-FRP tube connections
  Till, V., Morten, V., Kaufmann, M.

2021 **EURADH 2021 – 13th European Adhesion Conference**

- *Presentation:* Accelerated curing of adhesively bonded G-FRP tube connections
  T. Vallée, M. Voss, M. Kaufmann, M. Albiez

- *Poster:* Modelling the strength of adhesively bonded G-FRP tube connections
  T. Vallée, M. Voss, M. Kaufmann, M. Albiez

2021 **AB2021 – 6th International Conference on Structural Adhesive Bonding**

- *Presentation:* Numerical modelling of curie-supported accelerated curing by means of inductive heating
  M. Kaufmann, M. Voß, T. Vallée

- *Presentation:* Validation and numerical studies of Curie supported accelerated curing by means of inductive heating
  M. Voß, M. Kaufmann, T. Vallée

- *Presentation:* Load capacity prediction of bonded G-FRP tube connections
  T. Vallée, M. Voß, M. Kaufmann, H. Fricke, M. Albiez

- *Presentation:* Influences of Curie-susceptors induced accelerated curing on thermo-mechanical performance of 2K structural adhesives
  M. Voß, M. Kaufmann, T. Vallée

- *Presentation:* Capacity prediction of pre-tensioned hybrid joints for structural steel applications
  T. Gerke, C. Denkert, R. Glienke, M. Dörre, M.-K. Henkel, S. Myslicki, H. Fricke, M. Voß, M. Kaufman, T. Vallée

- *Presentation:* Experimental investigations on pretensioned hybrid joints for structural steel applications
  T. Gerke, C. Denkert, R. Glienke, M. Dörre, M.-K. Henkel, S. Myslicki, H. Fricke, M. Voß, M. Kaufman, T. Vallée

- *Poster:* Experimental investigations on accelerated curing of adhesively bonded G-FRP tube connections
  M. Voß, M. Kaufmann, H. Fricke, T. Vallée

2018 **WCTE 2018 – World Conference on Timber Engineering**

- *Presentation:* Experimental and numerical investigations on glued-in hardwood rods using bio adhesives
  Kaufmann, M., Kolbe, J., Vallée, T.

- *Presentation:* Capacity prediction for glued-in FRP joints
  Vallee, T., Kaufmann, M., Alter, B., Tannert, T.

2017 **AB2017 – 4th International Conference on Structural Adhesive Bonding**

- *Presentation:* Hardwood rods glued into softwood using environmentally sustainable adhesives
  M. Kaufmann, J. Kolbe, S. Lochte-Holtgreven, T. Vallée